Università degli Studi di Trieste

Sede Amministrativa del Dottorato di Ricerca

Scuola di Dottorato di Ricerca in Fisica
(XXII ciclo del Dottorato di Ricerca)

The role of the electron recoiling mechanism in coherent light high-order harmonics generation: from the source to the applications

Settore scientico-disciplinare FIS/03Fisica della Materia

Dottorando:
Alberto Simoncig

Coordinatore del Collegio dei Docenti:
Ch.mo Prof. Gaetano Senatore
(Università degli Studi di Trieste)

Supervisore:
Ch.mo Prof. Fulvio Parmigiani
(Università degli Studi di Trieste)

Anno Accademico 2008 – 2009

Transire suum pectus mundoque potiri
(Rise above oneself and grasp the world
Trascendere le limitazioni umane e padroneggiare l'universo)
ARCHIMEDES OF SYRACUSE

Avere non significa nulla, osare è ciò che conta.
REINHOLD MESSNER

Contents

1 The scope of the thesis **1**

2 HHG processes: theoretical background **5**

2.1 Introduction 5

2.2 Theory of high-order harmonic generation processes in inert gases 8

2.2.1 The rise and fall of the classical description 8

2.2.2 The quantum approach 17

2.3 The coherent building-up of EUV/SXR fields into a non-linear medium 23

3 HHG source: the design and the results **27**

3.1 Introduction 27

3.2 The laser source 29

3.2.1 The Mira Coherent® oscillator 29

3.2.2 The amplifier system 32

3.3 Design of an HHG source 32

3.3.1 The optical set-up 32

3.3.2 The HHG source and the detection system 35

3.4 Experimental results 37

3.4.1 Odd HHG orders 37

3.4.2 Even HHG orders 43

3.5 Discussion . . . 50
3.6 Conclusion . . . 57

4 The electron quantum paths **59**
4.1 Introduction . . . 59
4.2 Experimental results . . . 61
4.2.1 Spectral behavior of odd high-order harmonics . . . 61
4.2.2 Spectral behavior of even high-order harmonics . . . 65
4.3 Discussion . . . 68
4.3.1 The geometrical dispersion . . . 68
4.3.2 The dipole phase . . . 69
4.3.3 The induced temporal chirp . . . 73
4.4 Conclusion . . . 75

5 Damping of the non-perturbative process **77**
5.1 Introduction . . . 77
5.2 Control and manipulation of the dynamical regime . . . 78
5.2.1 The experimental set-up . . . 78
5.2.2 Experimental results . . . 79
5.2.3 Simulation of the damping of the tunneling mechanism 82
5.3 Conclusions . . . 85

6 Time-resolved EUV/MCD experiments **87**
6.1 Introduction . . . 87
6.2 Ultra-fast demagnetization processes . . . 88
6.3 Experimental set-up . . . 89
6.3.1 Development and test of the multi-layer quarter wave-plate device designed for EUV radiation . . . 91
6.3.2 The high-order harmonics generation vacuum chamber 95
6.3.3 The reflectometer experimental chamber . . . 97
6.4 Experimental results . . . 100
6.4.1 Static data on $M_{2,3}$ Fe-edge . . . 100
6.4.2 Static data on $M_{2,3}$ Ni-edge . . . 102
6.5 Conclusions . . . 103

7 Conclusions **105**

List of acronyms **117**

List of symbols **119**

Bibliografy **121**

Acknowledgment **127**

1

The scope of the thesis

The increasing development of light sources generating ultra-fast coherent pulses has given prominence to the possibility to map and control the dynamics of matter on the femtosecond (or sub-femtosecond) time scale. Nowadays, the high-order harmonic generation (HHG) process has to be consider as one of the most promising optical techniques for generating coherent radiation with a temporal duration approaching, under certain experimental conditions, the attosecond timescale and photon energies in the Extreme Ultra-Violet (EUV) and the Soft X-Rays (SXR) spectral regions.

From a phenomenological point of view, HHG can be described as a three steps process starting when the field of a very intense laser pulse interacts with an atomic (or molecular) system ionizing a bound electron. The ionized electron is subsequently accelerated into the continuum by the same field. When the laser field reverses, the electron has a finite probability of re-colliding with its parent ion eventually releasing the accumulated kinetic energy as high-energy photons, i.e. high-order harmonics (HH), which inherit the coherence properties of the radiation field.

However, this model is limited in descripting quantitatively the HHG process. Because of the quantum nature of the HHG process, the involved electron has to be described by a proper time dependent wavefunction that during the interaction endures a diffusion process. The importance of the wavefunction diffusion mechanism has been elucidated in a milestone paper, published in 1994 by M. Lewenstein and coauthors (*Theory of high-harmonic*

generation by low-frequency fields Phys. Rev. A **49**, 2117 − 2132), where it has been derived by means of a non-perturbative quantum model. Although the diffusion mechanism plays a key-role for the efficiency of the HHG processes, since it affects, negatively, the recoiling probability. It has been usually overlooked in the current experimental literature. On the other hand, being dependent on the spectral and temporal structures of the optical field it can be controlled manipulating the laser pulses.

The experimental and theoretical study of the wavefunction diffusion mechanism in the HHG processes represents the main scope of the present Ph.D. thesis in order to control the spectral and the coherence properties of the generated HH.

A detailed overview, concerning the theoretical description of the HHG processes in inert gases, will be presented in the second chapter, both in the classical and in a quantum frameworks, i.e. the Lewenstein's model. The tunability and the spectral properties have been investigated generating HH by means of different optical fields (third chapter), as a near-IR ($\lambda_0 \approx 800$ nm) one or its SH ($\lambda_{SH} \approx 400$ nm), in order to study their dependence on the diffusion mechanisms (Lewenstein's conjecture).

HH generated by near-IR laser pulses are modeled in a non-perturbative framework, although when the wavelength of the optical field is halved the process fits into an hybrid dynamical regime, i.e. it exhibit both non-perturbative and perturbative features. High-order harmonics have been generated by visible (the SH of a near-IR laser field) pulses in order to properly study such hybrid regime.

Finally, the spectral coherence properties have been studied in order to understand their dependence on the optical fields (fourth and fifth chapter). Such results contain useful informations on the dynamics of the involved electron.

As a possible interesting application it has been also considered the possibility for manipulating the state of polarization of the high-order harmonics, at the present limited by the fact that the ellipticity of the interacting field reduces the re-collision probability, i.e. the efficiency of the HHG process. In order to avoid such limitation a novel multi-layer quarter wave plate, designed for EUV radiation, has been developed in collaboration with the

Center for X-Rays Optics (CXRO) of the Lawrence Berkeley National Laboratory (LBNL) and successfully tested at the Advanced Light Source (ALS), both located in Berkeley (USA). By means of these optical devices, an unique experimental layout has been developed at the Elettra Synchrotron Light Source for probing the ultra-fast de-magnetization of ferromagnetic systems on a femtosecond timescale, by means of circularly polarized high-order harmonics. The sixth chapter reports the optical properties of such multi-layer devices, the test performed at ALS and, finally, the first results that proof the possibility to map the magnetic circularly dichroic contrast at the $M_{2,3}$ absorption edge of Fe or Ni, by means of circularly polarized high-order harmonics.

2

HHG PROCESSES: THEORETICAL BACKGROUND

2.1 Introduction

The last two decades have been characterized by a fast development of laser sources able to generate coherent pulses on the femtosecond (fs) timescale. Since the electron dynamics in atomic, molecular or more complex systems occurs between hundreds of femtoseconds to tens of attoseconds (as), such light pulses are the ideal tool to map and possibly control ultra-fast processes in matter [1, 2].

Figure 2.1 an useful sketch summarizing the timescales of the processes in matter, zooming (red line) in the femto/attosecond domains where several ultra-fast processes occur like the motion of individual valence and conduction band electrons (condensed systems), in the inner and outer shells (atomic or molecular systems), with the collective dynamics of free electrons [1, 3].

In 1999 Prof. Ahmed Zewail was awarded with the Nobel Prize in Chemistry for the development of the first time-resolved (TR) experiment employing laser pulses to map the dynamics of chemical reactions on a femtosecond timescale [4]. The key idea of TR optical technique is simple. An ultra-short laser pulse interacts with a system in order to promote a non equilibrium state. A second pulse, delayed in time, probes the system while is evolving through a relaxation process. A complete knowledge about such relaxation

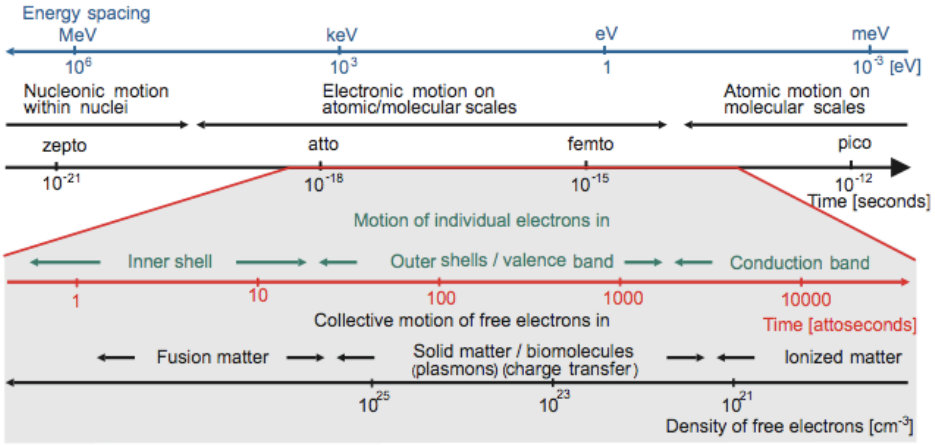

Figure 2.1: The temporal scale of matter. The red line focuses on the femto/attosecond timescale. Reported in [3].

dynamics can be achieved varying the temporal delay between these two pulses. Zewail's pioneering results have nudged a fast development of TR techniques in condensed matter research together with an increasing demand for new ultra-short coherent light sources [5, 6].

In this framework, the high-order harmonic generation (HHG) process can be consider as one of the most promising optical technique in order to develop TR experiments for condensed matter research [7]. This is due to the possibility of generating coherent radiation in a broad spectrum as the Extreme Ultra-Violet (EUV) and the Soft X-Rays (SXR) spectral regions, with a temporal duration from tens of femtosecond to the sub-femtosecond timescale (attosecond domain) [1, 2].

Taking advantage on the non-perturbative dynamics, which involves laser pulses and atomic (or molecular) systems, high-order harmonics (HH) can be generated with photon energies corresponding to the odd multiples of the angular frequency, ω_0, of the interacting field [1].

From a phenomenological point of view, HHG can be described starting from a three steps process [8, 9]. A laser field (with intensity $I_0 \geq 10^{13}$ Wcm^{-2}) interacts with an atomic (or molecular) system ionizing (1^{st} step) a bound electron. The de-localized (into the continuum) electron wavefunction wiggles (2^{nd} step) in the presence of the same optical electric field, $\mathbf{E}_L(t)$,

gaining kinetic energy. When $\mathbf{E}_L(t)$ reverses, the ionized electron has a finite probability of re-colliding (3^{rd} step) with its parent ion releasing the acquired kinetic energy as high-energy photons (HH), which inherit the coherence properties of the driving pulse [10, 11].

The available number of coherent EUV/SXR photons, strictly, depends on several factors like the spectral and temporal properties of the incoming optical field $\mathbf{E}_L(t)$, its polarization state (ellipticity) and the involved bound system [1].

The aim of this chapter is to present a detailed analysis concerning the theoretical description of the HHG processes in inert gases both in a classical and quantum frameworks. At the end, a brief overview on the existing TR applications of HH in condensed matter research will be reported.

2.2 Theory of high-order harmonic generation processes in inert gases

2.2.1 The rise and fall of the classical description

In this paragraph is reported a preliminary overview concerning the theory of the HHG processes in inert gases focusing the attention on the single steps. The first step (ionization) is modeled quantum mechanically, while a qualitative description of the second (wiggling) and the third (re-collision) steps has been achieved by means of the classical equations of motion.

The resulting HHG spectrum exhibits some features as the ones reported in the figure 2.2, where odd HH have been generated focusing in argon ≈ 2.0 mJ, ≈ 50 fs near-IR ($\lambda_0 \approx 800$ nm) laser pulses, reaching an intensity equal to $I_0 \approx 10^{15}$ Wcm^{-2} in the focal point.

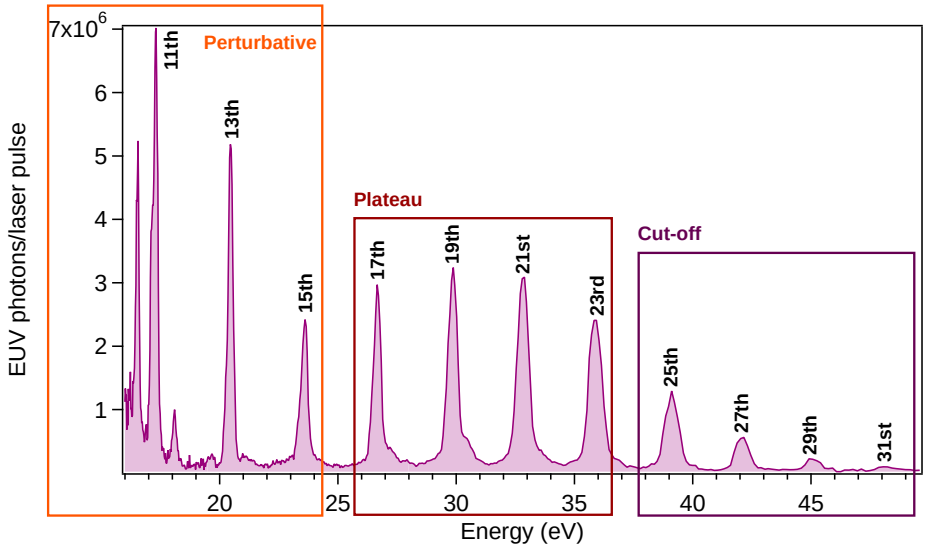

Figure 2.2: HHG spectrum generated in argon using ≈ 2.0 mJ, ≈ 50 fs, near-IR ($\lambda_0 \approx 800$ nm) laser pulses at a gas pressure of 5×10^{-3} mbar. The three colored boxes enclose the perturbative region (orange box), the plateau (red box) and the cut-off (violet box).

Three regions can be easily recognized:

- a perturbative region (orange box) where the low orders HH scale linearly, as expected by the standard perturbative law;

- a plateau region (red box) where the intensity of the HH (from to the 15^{th} order to the 23^{rd} one) remains approximately constant. The breaking of the perturbative scaling law reflects the non-perturbative nature of the HHG processes;
- a cut-off region (violet box) where the intensity abruptly falls down.

This discrete spectrum can be qualitative described, since the three steps mechanism repeats every half optical cycle $T/2$ and the corresponding Fourier transform is discrete. This means that the spectral components are separated by $2\pi(T/2)^{-1} = 2\omega_0$ [1]. As a consequence of this fact the measured spectrum exhibits only odd harmonics of the fundamental angular frequency, ω_0, i.e. $\omega_0 + 2\omega_2$, $\omega_0 + 4\omega_0$, ..., $\omega_0 + 2n\omega_0$ (being n an integer number).

The 1^{st} step: the ionization of a bound electron

The interaction between an intense electric field and a bound electron has been first investigated by Keldysh in the $60s$ in his pioneering work [12]. Till today it represents the basic approach to model the non-linear optical processes involving strong ($I_0 \geq 10^{13}$ Wcm^{-2}), ultrashort ($\tau_L \leq 100$ fs), light pulses and bound systems [14].

It is quite difficult to model this kind of interaction via the perturbation theory [13, 14], since the peak value of the optical field is comparable or higher than the coulomb potential of the atom.

The ionization process involves a transition between an initial bound state $|i\rangle$ and a continuum $|f\rangle$ one. Once the bound and free energies are known it is possible to evaluate a formal expression for the corresponding ionization rate Γ as done, originally, by Keldysh. The rate can be written as,

$$\Gamma \propto \exp\Big[-2Im\Big(S(\mathbf{p}, I_P)\Big)\Big], \tag{2.1}$$

being $S(\mathbf{p}, I_P)$ the well-known semi-classical action [13], which can be expressed as,

$$S(\mathbf{p}, I_P) = \int_{t_0}^{t} d\tau \Big[E_f(\tau) - E_i(\tau)\Big] = \int_{t_0}^{t} d\tau \left[\frac{1}{2}\Big(\mathbf{p} + \mathbf{A}(\tau)\Big)^2 - I_P\right]. \tag{2.2}$$

This means that the semi-classical action can be written as the difference between the final and the initial electron energies [13]. $\mathbf{p}$ is the canonical electronic momentum and I_P the first ionization potential of the non-linear medium, i.e. the energy (times minus 1) of the initially bound electron located into the ground state.

The ionization rate can be evaluated in the framework of the asymptotic analysis (saddle-points method), i.e. replacing the phase term with a sum over its saddle points where the integral piles up. This exponential behavior of the rate equation means that the (strong) electric field, $\mathbf{E}_0$, could modify the structure of the (Coulomb-like) binding potential allowing a tunneling process of the electronic wavefunction through the classical forbidden region.

The original work, evaluated for an hydrogen atom set in the presence of a strong electrostatic field, has been modified to arbitrary hydrogenoid systems interacting with a time-dependent field ,$\mathbf{E}_L(t)$, by Ammosov, Delone and Krainov [15] in 1986, and today it is referred as ADK model. The following equation (atomic units are used) refers to the ionization rate $\Gamma_{ADK}(t)$, with exponential accuracy [1, 15],

$$\Gamma_{ADK}(t) = N_{ADK}(t) \exp\left[-\frac{2(2I_P)}{3E_L(t)} \right], \tag{2.3}$$

where $N_{ADK}(t)$ is a pre-exponential factor dependent on the atomic quantum numbers and on I_P. It can be expressed as,

$$N_{ADK}(t) = A(l,m)B(n^*,l^*)I_P \sqrt{\frac{3E(t)}{\pi(2I_P)^{\frac{3}{2}}}} \left[\frac{2(2I_P)^{\frac{3}{2}}}{3E(t)} \right]^{2n^*-m-1}, \tag{2.4}$$

being n^* and l^*, respectively, the effective principal and angular quantum numbers[1], while l and m are the usual angular and magnetic momentum ones [1, 16]. The electric field is $\mathbf{E}_L(t) = \mathbf{E}_0 \cos(\omega_0 t + \theta_L)$, being θ_L an arbitrary extra phase term.

The probability $w_{ion}(t)$, for a shell closed atom, to be ionized by time t can be written as,

$$w_{ion}(t) = 1 - \exp\left[\int_{-\infty}^{t} d\tau \Big(-\Gamma_{ADK}(\tau) \Big) \right]. \tag{2.5}$$

[1] $n^* = Z(2I_P)^{-1/2}$ and $l^* = n^* - 1$

The Keldysh's parameter

The ionization rate $\Gamma_{ADK}(t)$ refers to the interaction between an atomic system and a static field (quasi-static approximation) if such optical field is strong and its angular frequency is low ($\omega_0 \to 0$) when compared to the atomic potential and the proper frequency of the bound electron [13]. In the quasi-static approximation the interaction between the bound electron (supposed to be localized into the ground state) and the static electric field can be compared to the study of a tunneling process through a triangular barrier created by the presence of $\mathbf{E}_0$. Since the electronic velocity changes as $v_e(t) = (2I_P - E_0 t)^{1/2}$, looking for $v_e(\tau) = 0$ it is easy to extrapolate a relation for the tunneling time τ_T [14],

$$\tau_T = \frac{\sqrt{2I_P}}{E_0}, \tag{2.6}$$

The main result of the Keldysh's work is the introduction of a phenomenological parameter [12] known as Keldysh's parameter (γ_K). It depends on the spectral and temporal structures of the optical field and on I_P and is defined as $\gamma_K = \omega_0 \tau_T$. This means that it is a dimensionless parameter depending on the product between the tunneling time and the optical angular frequency, i.e. the tunneling time modulated by the field frequency [14].

As a consequence of this fact, the quasi-static approximation is rightful in the limit $\gamma_K \ll 1$ where the binding barrier can be approximated to a static one, while the electron is tunneling through it (see figure 2.3). Nonetheless, in the opposite condition ($\gamma_K \gg 1$) the binding barrier starts to oscillate due to the increasing frequency of $\mathbf{E}_L(t)$. The ionization mechanism is usually modeled via a multi-photons absorption process able to promote the initially bound electron into the continuum.

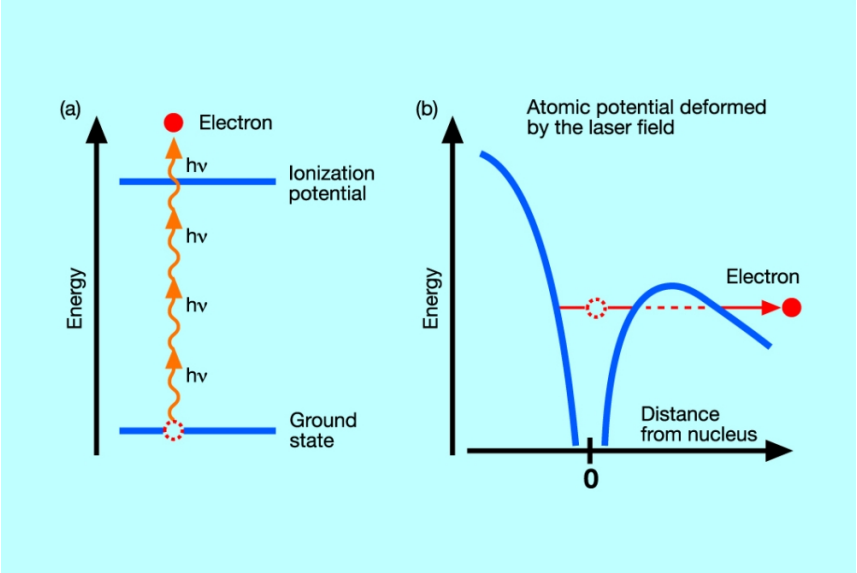

Figure 2.3: Ionization of an atomic electron via a) a multi-photon absorption ($\gamma_K \gg 1$) and b) a tunneling mechanism ($\gamma_K \ll 1$). Picture downloaded from [17]

The 2^{nd} step: wiggling in the optical field

Once ionized, the electron wiggles in the presence of $\mathbf{E}_L(t)$. Neglecting the effect of the deformed binding potential V_b during this 2^{nd} step (this is the basic assumption of the strong-field approximation or SFA) the electron dynamics can be modeled by means of the classical equations of motion. In the presence of a s-polarized electric field $E_L(t) = E_0 \cos(\omega_0 t + \theta_L)$ the electron velocity $\dot{x}(t)$ follows as [1, 3],

$$\begin{aligned} \dot{x}(t) = \int_0^t \mathrm{d}\tau \left[-\frac{e}{m} E(\tau) \right] &= -\frac{eE_0}{m\omega_0} \Big[\sin(\omega_0 t + \theta_L) - \sin(\theta_L) \Big] \\ &= -\frac{eE_0}{m\omega_0} \sin(\omega_0 t + \theta_L) + \dot{x}_0. \end{aligned} \tag{2.7}$$

Starting from the previous equation it is possible to evaluate the electron kinetic energy, as a function of θ_L. The kinetic energy averaged on an optical period (T) is usually defined as the quiver[2] (or ponderomotive) potential U_P.

[2] $U_P[\mathrm{eV}] = 0.96 \times 10^{-13} \mathrm{I}[\mathrm{Wcm}^{-2}] \lambda_0{}^2[\mu\mathrm{m}^2]$

Integrating one more time the law of motion follows as,

$$x(t) = \underbrace{\frac{eE_0}{m{\omega_0}^2}\Big(\cos(\omega_0 t + \theta_L) - \cos(\theta_L)\Big)}_{oscillation} + \underbrace{t\,\frac{eE_0}{m\omega_0}\sin\theta_L}_{drift}\,. \tag{2.8}$$

This equation means that the electron wiggles into the optical field with a motion composed by a linear drift plus an oscillation around this position.

The previous equation refers to the fact that the position $x(t)$ depends on the phase θ_L at which the electron has been ionized. The values of θ_L, corresponding to the non trivial solutions of $x(t)$, identify the closed trajectories which represent the radiative channel that lead to the emission of coherent EUV/SXR photons. This means that several processes compete with each other depending on the phase θ_L the electron has been ionized, as shown in the following figure 2.4 [8, 18] .

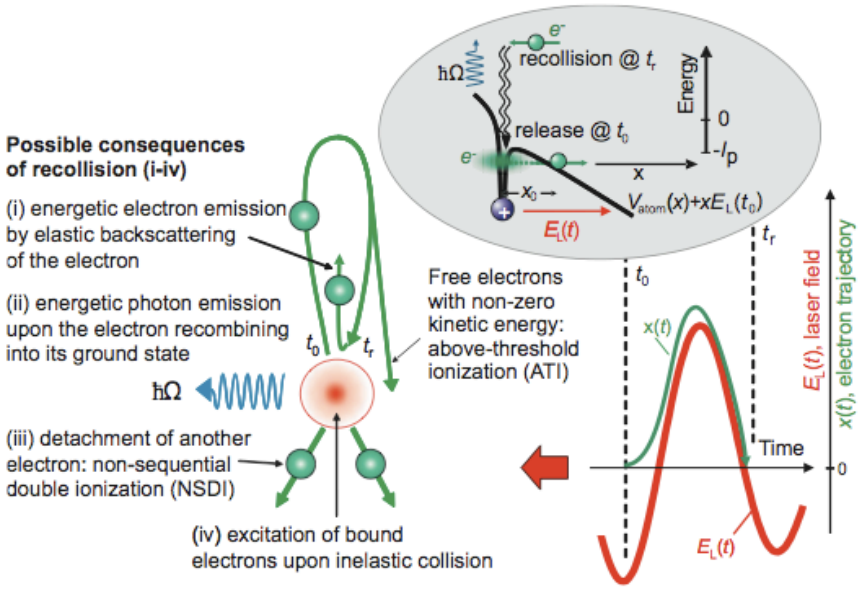

Figure 2.4: Pictorial representation of the three steps process that lead to the emission of HH. The picture reports the processes competing with HHG (i, ii and iv). Reported in [3].

The 3^{rd} step: the re-collision process

When the optical field reverses, the electron has a finite probability of re-coiling back with its parent ion releasing the accumulated kinetic energy as HH. Nonetheless, several processes compete with the emission of the coherent EUV/SXR pulses. Each of them is characterized by a swarm of different classical trajectories [3]:

- the accumulated kinetic energy can be emitted as EUV/SXR photons (HHG process). High-order harmonics are generated only when the electron is ionized at peculiar values of θ_L;
- this process has to compete with two other ones, since the re-collinding electron can scatters off with its parent ion, elastically or inelastically, leading to the ionization of a second electron (atomic fragmentation);
- the excited electron can not re-collide, since it leave the atom at θ_L values that forbid the re-collision.

Some classical trajectories evaluated at different θ_L are reported in the figure 2.5. In this peculiar case, the violet line leads to multiple re-collisions, but only the first two give re-collisions rise to a significant EUV/SXR photons emission [1]. This fact is due to the diffusion mechanism felt by the electron wavefunction during the wiggling process (2^{nd} step), since the overlap between the electron and the ion becomes smaller when the diffusion increases with time [19]. Unfortunately, this classical description is not able to take into account for the diffusion mechanism felt by the electron wavefunction and a more specific description is invoked and will be presented in the next paragraph.

The corresponding kinetic energies at the time of re-collision can be computed starting from the numerical solutions of $x(t)$, i.e. for different values of θ_L. The numerical solution of the previous equation for different values of $\theta_L(t)$ allows to obtain the corresponding kinetic energies. The maximum value is equal to $\approx 3.17U_P$ (corresponding to a phase of ≈ 18 degrees or $\approx \pi/10$ radians). The figure 2.6 refers to the kinetic energy as a

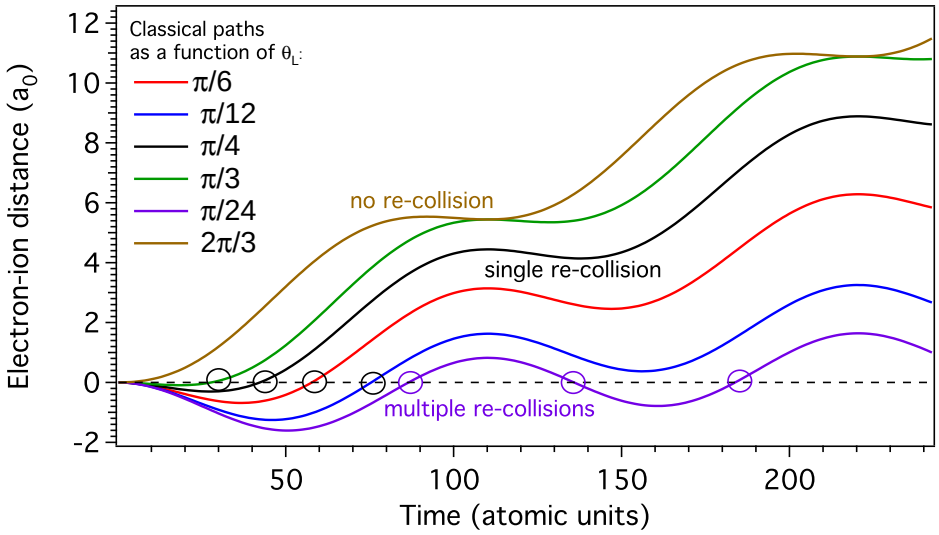

Figure 2.5: Classical electronic trajectories (electron-ion distance) in atomic units (1 a.u. is $\approx$ 24 attoseconds), as a function of different values of θ_L. A path (violet line) leads to multiples re-collisions, others to a single one. The brown line refers to a possible classical trajectory that do not involve a re-collision process. The circles emphasize the re-collision time. An optical period for a near-IR field ($\lambda_0 \approx 800$ nm) is ≈ 111 a.u.

function of $\theta_L(t)$. The accumulated kinetic energy is degenerate on θ_L, i.e. on the phase at which the electron has been ionized [1]. This means that two different trajectories lead to the same kinetic energy at the moment of re-collision. These trajectories are referred to short and long paths. From the same equation, it is also possible to derive the maximum photon energy releasable, which is equal to $\hbar\omega_{co} \approx 3.17U_P + I_P$ and this relation is known as cut-off law. In conclusion, an analysis of the electron trajectories by means of the classical equations of motion, allows to predict:

- the dependence of the re-collision process as a function of θ_L;
- the cut-off law;
- the degeneracy of the HH energy depending on the traveling time, i.e. the existence of short and long paths.

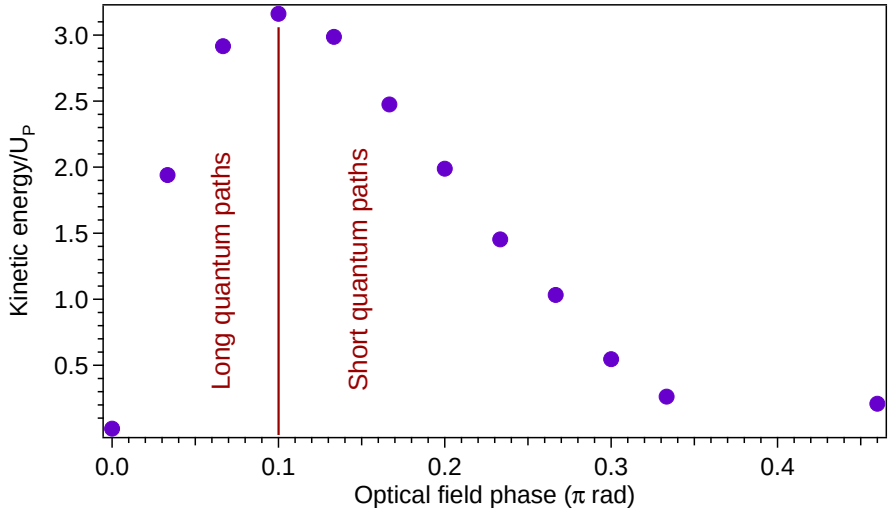

Figure 2.6: Gained kinetic energies (as a function of U_P) from the classical equation of motion. The ionized electron between 0 degree and $\approx$ 18 degrees will travel on a longer trajectory (long path). Otherwise, if ionized between $\approx$ 18 degrees and 90 degrees it will travel on the so called short path.

On the other hand, this classical description of the HHG processes is not able to include the diffusion mechanism that affects the dynamics of the electron wavefunction.

2.2.2 The quantum approach

The three steps model can be also deduced from a semi-classical approach, i.e. modeling the atomic electron as a non-relativistic bound particle and the optical (laser) field, $\mathbf{E}_L(t)$, as a classical field. When this field interacts with the atom (molecule) a fast-oscillating dipole moment in induced, leading to the emission of EUV/SXR coherent radiation. As previously underlined, is not possible to model such processes by means of the perturbation theory (due to the strong peak value of the optical field). Nonetheless, the response of a single atom to the presence of $\mathbf{E}_L(t)$ can be evaluated in two different ways.

The expectation value of the induced dipole moment, $\langle \mathbf{d}(t) \rangle$, can be quantitatively computed solving (numerically) the following time-dependent Schroedinger equation (TDSE), where $|\psi, t\rangle$ is the electronic state evaluated at time t (atomic units are used here),

$$i\partial_t |\psi, t\rangle = \Big(\hat{H}_{kin} + \hat{V}_b + \hat{H}_{int}(t)\Big)|\psi, t\rangle, \tag{2.9}$$

being $\hat{H}_{kin}$ the kinetic hamiltonian term, $\hat{V}_b$ the (Coulomb-like) binding potential and $\hat{H}_{int}(t)$ the interaction term.

Being the numerical integration of the TDSE quite time consuming [18], a saddle-point approach is invoked to calculate the non-perturbative atomic response to the presence of a strong field, as done by Lewenstein and coauthors in 1994 [19]. This approach has turned out to be the correct one to qualitatively reproduce the measured HHG spectra.

In order to complete the theoretical description of the HHG processes including their intrinsic quantum features, a short introduction, concerning the Lewenstein's model, is presented in the following.

Supposing that only one electron is involved in the process (single electron approximation or SEA) the ansatz for its state $|\psi, t\rangle$ at time t is,

$$|\psi, t\rangle = \underbrace{b(t)|\psi_b, t\rangle}_{bound} + \underbrace{\int \mathrm{d}\mathbf{v} c(\mathbf{v}, t)|\mathbf{v}, t\rangle}_{continuum}, \tag{2.10}$$

i.e. an overlap between the bound state $|\psi_b, t\rangle$ and a continuum (ionized) state $|\mathbf{v}, t\rangle$. The coefficients refer to the probability to localize the electron

into the bound or the continuum states, respectively. The integral spreads all the possible electronic velocity values, i.e. $\mathbf{v}$, acquired into the laser field continuum.

The transition amplitude

If at the initial time, t_0, the electron is localized into the atomic ground state $|0\rangle$ (the excited bound states do not contribute) and the optical field is supposed to be switched off, the bound-free transition (neglecting all the possible bound-bound and free-free contributions) amplitude $c_{bf}(\mathbf{v}, t, t_0)$ at time t can be written, as,

$$c_{bf}(\mathbf{v}, t, t_0) = \langle \mathbf{v}, t|0, t\rangle = \langle \mathbf{v}, t|\hat{U}(t, t_0)|0\rangle, \tag{2.11}$$

where the state $|0\rangle$ has been propagated from t_0 to t, by means of the time-evolution unitary operator $\hat{U}(t, t_0)$[20].

Neglecting the term $\hat{U}_0(t, t_0)$ inside $\hat{U}(t, t_0)$, dependent only on the kinetic hamiltonian $\hat{H}_{kin}$, the transition amplitude becomes,

$$c_{bf}(\mathbf{v}, t, t_0) \approx -i \int_{t_0}^{t} \mathrm{d}\tau \langle \mathbf{v}, \tau|\hat{H}_{int}(\tau)|\psi_b, \tau\rangle. \tag{2.12}$$

In order to evaluate $c_{bf}(\mathbf{v}, t, t_0)$ it is necessary to introduce a formal expression for the initial state, the final states and the interaction hamiltonian, as reported in the following:

- the initial state $|\psi_b, t\rangle$ can be evaluated propagating the ground state $|0\rangle$ at τ, i.e. $e^{iI_P\tau}|0\rangle$;
- the final state, in the framework of the SFA, can be approximated as a Volkov state [21]. This state can be obtained, starting from a free electron interacting with an optical field, by the time-dependent Schroedinger equation,

$$i\partial_t|\psi, t\rangle = \frac{1}{2}\Big(\mathbf{p} - \mathbf{A}_L(t)\Big)^2|\psi, t\rangle. \tag{2.13}$$

  being $\mathbf{A}_L(t)$ the vector potential of the optical field and $\mathbf{p}$ the electronic canonical momentum. A possible solution of the TDSE is,

$$|\psi, t\rangle = \exp\left(-\frac{i}{2}\Phi(\mathbf{p}, t, t_0)\right)|\psi, t_0\rangle, \tag{2.14}$$

where the phase term (known as Volkov phase) depends on the semi-classical action and is equal to,

$$\Phi(\mathbf{p}, t, t_0) = \frac{1}{2}\int_{t_0}^{t} \mathrm{d}\tau \Big(\mathbf{p} - \mathbf{A}_L(\tau)\Big)^2. \tag{2.15}$$

The Volkov phase contains the set of informations concerning the electron propagation in the presence of the optical field. By means of the introduction of two completeness relations, $\int \mathrm{d}\mathbf{x}|\mathbf{x}\rangle\langle\mathbf{x}|$ and $\int \mathrm{d}\mathbf{p}|\mathbf{p}\rangle\langle\mathbf{p}|$, in the equation 2.14, it is possible to define, via a Fourier transform, the corresponding electron wavefunction,

$$\psi(\mathbf{x}, t) = (2\pi)^{-3/2}\int \mathrm{d}\mathbf{p} e^{i\mathbf{p}\cdot\mathbf{x}} e^{-i\Phi(\mathbf{p},t,t_0)}\tilde{\psi}(\mathbf{p}, t_0). \tag{2.16}$$

- The interaction hamiltonian can be written by means of the dipole approximation as $\hat{H}_{int}(t) = \mathbf{x}\cdot\mathbf{E}_L(t)$.

The dipole moment and the saddle-points approach

Introducing a completeness relation, $\int d\mathbf{x}|\mathbf{x}\rangle\langle\mathbf{x}|$, the bound-free transition amplitude $c_{bf}(\mathbf{v}, t, t_0)$ can be written as,

$$\begin{aligned} c_{bf}(\mathbf{v}, t, t_0) \approx -i(2\pi)^{-3/2}\int_{t_0}^{t}\mathrm{d}\tau\int \mathrm{d}\mathbf{x} e^{-i\mathbf{v}\cdot\mathbf{x}} \\ \times e^{iS(\mathbf{p},\tau)}\mathbf{x}\cdot\mathbf{E_0}\cos(\omega_\mathbf{0}\tau)\psi_\mathbf{b}(\mathbf{x},\tau), \end{aligned} \tag{2.17}$$

$$= -i(2\pi)^{-3/2}\int_{t_0}^{t}\mathrm{d}\tau\mathbf{E}_0\cos(\omega_0\tau)\langle\mathbf{v}|x|0\rangle e^{iS(\mathbf{p},t,\tau)}. \tag{2.18}$$

Setting $\langle\mathbf{v}|x|0\rangle$ as $d(\mathbf{v})$ (the dipole amplitude) and $S(\mathbf{p}, t, \tau) = \Phi(\mathbf{p}, t, \tau) + I_P$ (the Volkov phase plus a term depending on the atomic system) it is possible to define the expectation value of induced dipole moment as,

$$\langle\mathbf{d}(t)\rangle = \langle\psi, t|\hat{\mathbf{x}}|\psi, t\rangle = \int \mathrm{d}\mathbf{v} d^*(\mathbf{v})c(\mathbf{v}, t) + c.c. \tag{2.19}$$

Replacing the transition amplitude $c_{bf}(\mathbf{v}, t, t_0)$ into the 2.19 equation and setting $\mathbf{v} = \mathbf{p} - \mathbf{A}_L(t)$, it ca be re-written as,

$$\begin{aligned}\langle \mathbf{d}(t) \rangle = -i \int_0^t \mathrm{d}\tau \int d\mathbf{p} \underbrace{E_0 \cos(\omega_0 \tau) d\Big(\mathbf{p} - \mathbf{A}_L(\tau)\Big)}_{1^{st}step} \\ \times \underbrace{e^{-iS(\mathbf{p},t,\tau)}}_{2^{nd}step} \\ \times \underbrace{d^*\Big(\mathbf{p} - \mathbf{A}_L(\tau)\Big)}_{3^{rd}step} + c.c.\end{aligned} \tag{2.20}$$

Here t_0 has been set equal to 0.

The previous equation represents a sum of amplitudes corresponding to the three steps [19]:

- the probability amplitude to promote a bound electron (1^{st} step) in the continuum, at time τ and canonical momentum $\mathbf{p}$, is modeled by the term $E_0 \cos(\omega_0 \tau) d\Big(\mathbf{p} - \mathbf{A}_L(\tau)\Big)$;
- the electron wavefunction is propagated (2^{nd} step) until the time t acquiring a phase equal to $\exp\left(-iS(\mathbf{p}, t, \tau)\right)$;
- at time t the re-covering (3^{th} step) takes place with probability amplitude equal to $d^*\Big(\mathbf{p} - \mathbf{A}_L(\tau)\Big)$.

As a consequence of the presence of such a fast-oscillating phase the calculation of the last integral is quite difficult. Nevertheless, it can be performed by means of saddle-points method, i.e. looking for the stationary points of the semi-classical action. The saddle points equations arise from the following derivates of the semi-classical action $S(\mathbf{p}, t, \tau)$,

$$\partial_{\mathbf{p}} S(\mathbf{p}, t, \tau) = \tau \mathbf{p} - \int_{t-\tau}^{t} \mathrm{d}\tilde{\mathrm{t}} \mathbf{A}(\tilde{t}) = \mathbf{0}, \tag{2.21}$$

$$\partial_{\tau} S(\mathbf{p}, t, \tau) = \frac{1}{2}\Big(\mathbf{p} - \mathbf{A}_L(t-\tau)\Big)^2 + I_P = 0, \tag{2.22}$$

$$\begin{aligned}\partial_t S(\mathbf{p}, t, \tau) = \frac{1}{2}\Big(\mathbf{p} - \mathbf{A}_L(t)\Big)^2 - \frac{1}{2}\Big(\mathbf{p} - \mathbf{A}_L(t-\tau)\Big)^2 \\ = (2n+1)\omega_0,\end{aligned} \tag{2.23}$$

being n a positive integer number.

The three saddle-points equations evaluated on the canonical momentum $\mathbf{p}$ refer to the fact that only the electron trajectories leading to a recoiling process contribute to the generation of coherent EUV/SXR photons. Being I_P a real and positive value the electron leaving the atom at time $t-\tau$ has to travel thought the binding barrier with negative kinetic energy. This boundary condition means that τ has to be a complex variable, i.e. it implies a tunneling description of the ionization process [19]. The third equation emphasizes the energy conservation law, i.e. a formal explanation for the generation of only odd HH of the interacting field [19].

In addition, also the stationary value of the canonical electronic momentum can be easily evaluated by means of the first saddle-point equation. It appears as,

$$\mathbf{p}_{st}(t,\tau) = \frac{\mathbf{E}_0}{\tau}\Big[\cos\Big(\omega_0 t + \theta_L\Big) - \cos\Big(\omega_0(t-\tau) - \theta_L\Big)\Big], \tag{2.24}$$

being,

$$S_{sp}(t,\tau) = I_P\tau + \frac{1}{2}\int_{t-\tau}^{t} \mathrm{d}\tilde{\mathrm{t}}\Big(\mathbf{p}_{st} - \mathbf{A}(\tilde{t})\Big)^2, \tag{2.25}$$

the corresponding semi-classical action, Following the Lewenstein's model the semi-classical action can be re-written as [19],

$$\begin{aligned} S_{sp}(t,\tau) = (I_P + U_P)\tau - 2U_P\frac{1-\cos\Big(\omega_0\tau\Big)}{\omega_0\tau} + \\ -U_P C(\tau)\cos\Big(\omega_0(2t-\tau)\Big), \end{aligned} \tag{2.26}$$

i.e. dependent on the function $C(\tau)$,

$$C(\tau) = \sin\Big(\omega_0\tau\Big) - 4\frac{\sin\Big(\omega_0\tau/2\Big)^2}{\tau\omega_0}. \tag{2.27}$$

The function $2|C(\tau)|$, which depends on the return time τ, gives the variation of the semi-classical action as a function of t, i.e. $\partial_t S_{sp}(t,\tau)$. The physical meaning of the action is well known, being $S_{sp}(t,\tau)$ the integral of the accumulated kinetic energy during the propagation in the optical field, which maxima corresponds to the maxima of $2|C(\tau)|$. Figure 2.7 reports the behavior of $2|C(\tau)|$ as a function of τ, i.e. the maxima of the acquired kinetic energy as a funtion of the return time. It easy to see that the first, and

higher, of such maxima corresponds to the value ≈ 3.17, predicted by means of the classical equations. This means that the saddle-points analysis proposed by M. Lewenstein and coauthors is correct in order to reproduce the results of the classical description of HHG processes, shown in the previous paragraph.

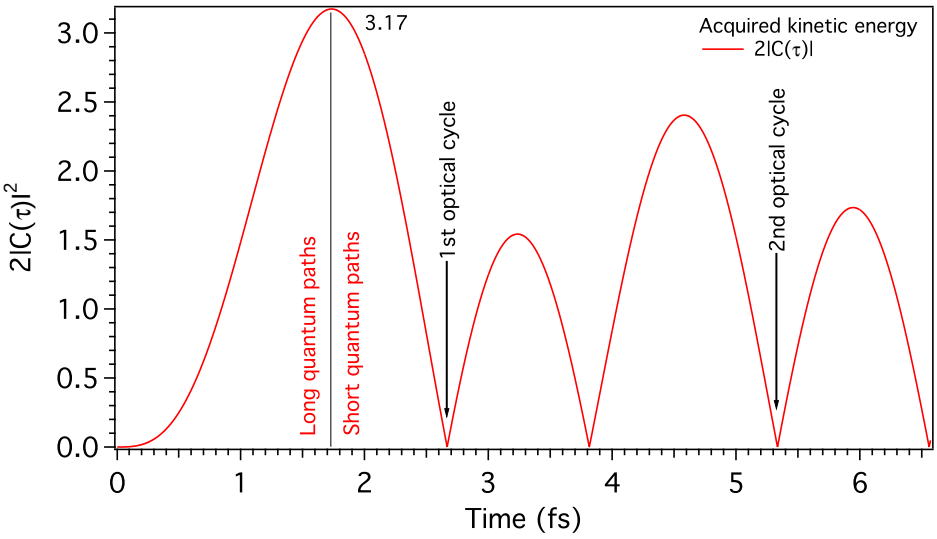

Figure 2.7: The behavior of $2|C(\tau)|$ as a function the time (fs). The values have been calculated for a near-IR optical field with wavelength $\lambda_0 \approx 800$ nm. The corresponding angular frequency is $\omega_0 \approx 0.057$ (expressed in atomic units). The optical period is ≈ 2.7 fs.

In order to complete the saddle-points analysis it is required to include the effect of the second order partial derivative to ensure that $\langle \mathbf{d}(t) \rangle$ can be integrated [19]. $\partial_{\mathbf{p},\mathbf{p}} S(\mathbf{p}, t, \tau)$ introduces a factor equal to $[\pi/\epsilon + i\tau/2]^{3/2}$, i.e. it model the behavior of the expectation value of the dipole moment as a function of the return time. It easy to recognize that at higher values of τ, $\langle \mathbf{d}(t) \rangle$ decreases. This means that the efficiency of the HHG process decreases, since the electron wavefunction encounters a diffusion process, reducing the overlap of between the electron and the parent ion.

2.3 The coherent building-up of EUV/SXR fields into a non-linear medium

A detailed analysis concerning the response of a single atomic system on the presence of an interacting field has been presented in the two previous paragraphs. Nonetheless, the experimental HH signal results from the contribution of the fields generated by each atomic system present in the non-linear medium. In order to maximize the intensity of the HH signal, i.e. the number of available EUV/SXR photons, it is necessary to require that the HH fields add coherently [1, 23].

This condition is satisfied when the wavevector mismatch Δk is equal to 0, i.e. $\Delta k = k_{q\omega_0} - k_{\omega_0} = 0$ ($k_{q\omega_0}$ is the wavevector for the q harmonic order). This means that the phases of the HH field ($k_{q\omega_0}$) and the fundamental (k_{ω_0}) one, have to add coherently (phase-matching condition or PM) while propagating inside the non-linear medium. An useful sketch showing the ideal coherent building-up of the generated HH fields is reported in figure 2.8 [1].

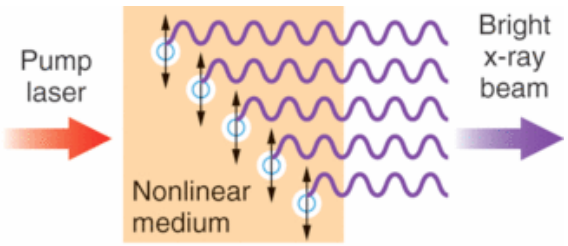

Figure 2.8: Coherent building-up of the generated HH fields into the non-linear medium.

From an experimental point of view, the PM relation is $\Delta k \neq 0$, since the propagation of the EUV/SXR radiation in the non-linear medium (inert gas) depends on several factors. Any medium exhibits a dispersion and this means that its refractive index $n(\omega)$ depends on the HH frequency $\omega = q\omega_0$. The corresponding contribution to the PM (the q-order harmonic) is $\Delta k_{disp} = qk_{disp}(\omega_0) - k_{disp}(\omega)$. Since the refractive index is larger than 1 both for near-IR and visible fields and smaller than 1 for EUV/SXR ones [24], the corresponding dispersion is $\Delta k_{disp} > 1$.

As previously underlined, the HH are generated only if the electrons are ionized at peculiar values of θ_L. The swarm of paths that do not lead to re-collison of the ionized electron with its parent ion generates a plasma, with a proper plasma frequency ω_P and a refractive index $n_P(\omega)$ varying as $\left[1-(\omega_P/\omega)^2\right]^{1/2}$ [1]. In HHG process the plasma density is lower than the critical value N_c, so the refractive index can be approximated as $n_P(\omega) \approx 1-(\omega_P/4\omega)^2$, corresponding to,

$$\Delta k_P = \frac{{\omega_P}^2(1-q^2)}{2qc\omega_0}, \tag{2.28}$$

being $\Delta k_P < 0$.

In order to generate HH the driving optical field (with wavelength λ_0) has to be focused onto the non-linear medium by means of a lens (or a spherical mirror) with focal length f_0 to reach a proper I_0 value. The initial radius of the spot[3] (w) is decreased to $w_0 = f_0\lambda_0/\pi w$. The propagating beam $E(z) \propto e^{-ikz}$ acquires a phase value $\Phi_{Gouy}(z)$ known as Gouy phase, equal to $\Phi_{Gouy}(z) = \arctan(\lambda_0 z/\pi {w_0}^2)$. This phase is related to the wave vector by the relation $k_{geo}(z) = \partial_z(\Phi_{Gouy}(z))$ and around the focus position z_0 can be approximated as $2/b$, being b the well known confocal parameter.

This parameter is the same for each HH, so the total contribution to the PM is $\Delta k_{geo} = 2(q-1)/b$, i.e. $\Delta k_{geo} > 0$.

This approach is correct if the optical field is focused onto the non-liner medium for example a gas set in a free jet or a close volume. If the HH are generated focusing $\mathbf{E}_L(t)$ into a capillary, i.e. a guided geometry, the contribution to PM changes, being lower than 1. In this thesis, HH have been always generated in a cell filled with inert gas (see next chapters).

In conclusion, under the PM conditions Δk depends on spatial properties of the focused optical beam, the generated plasma and the neutral dispersion of the non-linear medium. The dependences of i) Δk_{geo} on z and ii) Δk_P on the plasma density, imply that it is possible to optimize the PM condition moving the relative position (Δz) between the focus and the gas, and varying the gas pressure.

The optimization of Δk by means of gas pressure, is clearly limited by the re-absorption of the EUV/SXR radiation in the non-linear medium itself.

[3] $w(z) = w_0\sqrt{1+(z/z_R)^2}$ being z_R the Rayleigh length.

This fact is due to the large photoionization cross section σ_e that many media exhibit in the spectral range from the ultra-violet (UV) to the SXR [24]. Once the amplitude (single atom response) for the q-order harmonic A_q is known, it is possible to define the yield for this harmonic order, depending on the propagation distance z inside the non-linear medium (with length L), as follows,

$$I_q \approx \left| \int_0^L \rho_0 A_q e^{i\Phi_q(z)} \left(- \frac{L-z}{2L_{abs}} \right) \right|^2, \tag{2.29}$$

being ρ_0 the density of atoms (supposed constant), and L_{abs} the absorption length. If A_q does not be independent on z, the previous integral results

$$\begin{aligned} \frac{I_q}{\rho_0 A_q} \approx & \frac{4{L_{abd}}^2}{1+4\pi^2(L_{abs}/L_c)^2} \\ & \times \left[1 + \exp\left(- \frac{L}{L_{abs}} \right) - 2\cos\left(\frac{\pi L}{L_c} \right) \exp\left(- \frac{L}{2L_{abs}} \right) \right], \end{aligned} \tag{2.30}$$

where $\Phi_q(z)$ is equal to $-z\Delta k$.

3

HHG SOURCE: THE DESIGN AND THE RESULTS

3.1 Introduction

The simplest way for generating coherent EUV/SXR photons via HHG processes is to focus an ultra-short ($\tau_L \leq 100$ fs) and strong ($I_0 \geq 10^{13}$ Wcm^{-2}) laser pulse onto a non-linear medium, for example an inert gas set into a free jet or constrained into a cell [1, 3]. As underlined in the previous chapter, a laser field, $\mathbf{E}_L(t)$, induces a fast-oscillating dipole moment generating coherent radiation with photon energies corresponding to the odd multiplies of the laser angular frequency, ω_0, and extending from the EUV up to the SXR spectral regions. These HH pulses exhibit a temporal structure comparable to that of the original driving pulse, i.e. in the femtosecond time domain, or, under certain experimental conditions, in the attosecond time domain [2].

In a less phenomenological framework the quantum nature of the HHG processes can not be overlooked, since the freed electrons have to be modeled by a proper time dependent wavefunction enduring a diffusion mechanism during the propagation in the interacting field (2^{nd} step). As shown in [19], this mechanism plays a key-role for the HHG efficiency, since it affects negatively the re-coiling amplitude reducing the overlap between the electron and its parent ion. Nonetheless, M. Lewenstein and coauthors have predicted a scaling law for such diffusion mechanism [19] by means of a

non-perturbative quantum approach (see previous chapter). It is expected to scale as T^3, i.e. with the cube of the optical period. As a consequence, shortening the wavelength (λ_0) of the interacting field, the HHG efficiency is expected to increase (Lewenstein's conjecture), for example comparing the results obtained generating HH by means of a laser field and/or its second harmonic (SH) [27, 28]. The existing literature accounts for several experiments where EUV/SXR pulses have been generated by means of the HHG process using a driving field characterized by a single photon frequency or by mixed frequencies (two-color generation). Nonetheless, an experiment to prove the Lewenstein's conjecture has never been reported.

A careful control of the experimental set-up, along with an unambiguous detection scheme to avoid any spurious effects, is required to report a detailed quantitative analysis on the spectral properties of the generated HH (in terms of the EUV/SXR photons) in order to emphasize the contribution of the diffusion mechanism. The experimental set-up has been developed at the T-ReX Laboratory, located at the Elettra Synchrotron Light Source in Trieste (Italy) [29].

This chapter reports the study of the spectral properties of HH generated from the interaction between an inert gases and a ≈ 2.5 mJ, ≈ 50 fs, near-IR ($\lambda_0 \approx 800$ nm) laser pulses or the SH of such pulses, both operating at a repetition rate of 1 kHz.

To the author's knowledge these results represent the first detailed study on the dependence of spectral properties of the generated HH of the driving field, i.e. on the wavefunction diffusion mechanism, which is usually overlooked in the existing experimental literature.

3.2 The laser source

In order to study the spectral properties of HH, a commercial laser source has been used to generate the optical pulses. In figure 3.1 the set-up of the laser source is reported. This is based of an oscillator generating coherent pulses of $\approx$ 50 fs, at $\lambda_0 \approx 800$ nm and a repetition rate (r.r.) of 76 MHz. The oscillator is pumped by visible ($\lambda_{pump} = 532$ nm) coherent light. The coherent pulses generated by the oscillator are amplified up to $\approx$ 2.5 mJ, while the temporal structure is $\approx$ 35 fs. The amplifier operates at a r.r. of 1 kHz.

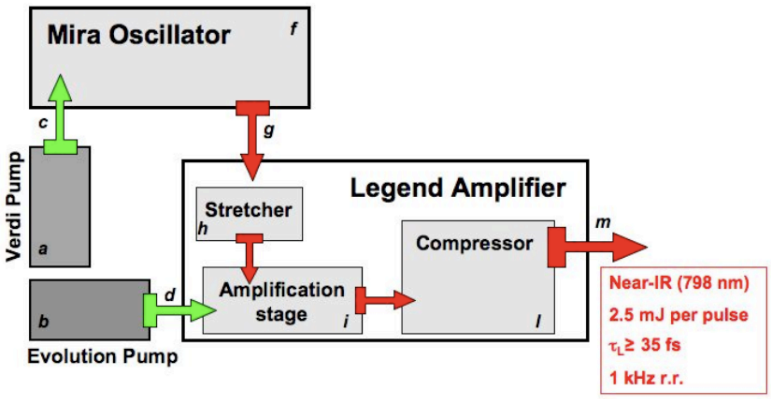

Figure 3.1: Sketch of the laser source. It consists of two visible pump lasers (a,b), an oscillator (f), an amplifier with its stretcher (h), the amplification stage (i) and the final compressor (l). The green arrows (c,d) and the red ones (g,m) refers to the path followed by the light.

3.2.1 The Mira Coherent® oscillator

The near-IR pulses train is generated via a Kerr-lens mode locked [5, 6] Ti:Sapphire (Ti:Al_2O_3) commercial oscillator (f) from Coherent®, pumped by a continuos (a) laser (Verdi-5 from Coherent®) generating radiation centered at 532 nm (c), with an average power of 5 W. The mode-locking process is able to generate near-IR pulses with a band-width set between 45 and 50 nm, centered at a wavelength of $\approx$ 796 nm, corresponding to a photon en-

ergy of ≈ 1.55 eV [30]. The temporal duration of these pulses is $\tau_L \approx 50$ femtoseconds, at a r.r. of 76 MHz with an average power of 350 mW (≈ 4.6 nJ energy per pulse). In the figure 3.2 is reported a sketch of the optical set-up of the Mira oscillator. Once generated the ultra-short pulses are sent into the commercial regenerative amplifier.

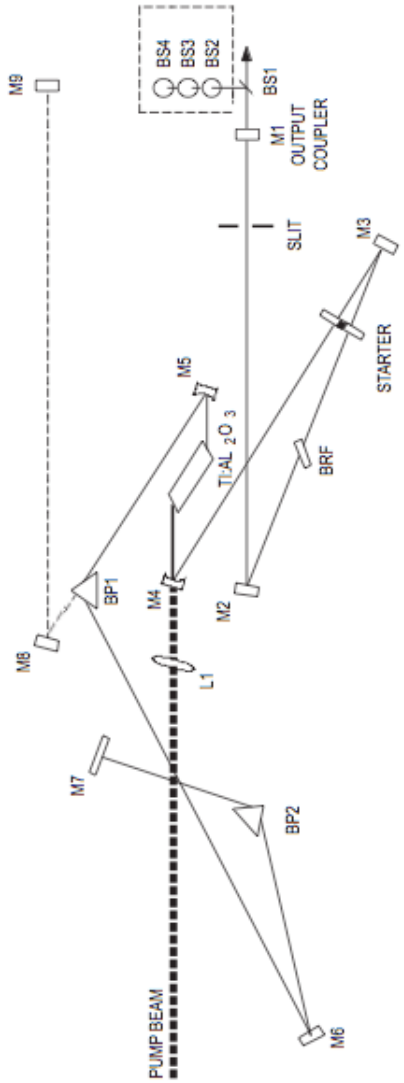

Figure 3.2: Optical set-up of the Mira Coherent® oscillator.

3.2.2 The amplifier system

The amplifier consists of three different stages (see figure 3.1) as i) a stretcher (h), ii) an amplification module (i) and a iii) compressor (l). A second (pulsed) pump (b,d) laser lowers the r.r., from 76 MHz to 1 kHz and increases the energy per pulse until $\approx$ 2.5 mJ, lowering the temporal duration of $\tau_L \geq 35$ fs (m).

The pulses generated by the Mira oscillator, once sent to the Legend-Elite amplifier, pass through three stages:

- a stretcher stage increases the temporal duration of the pulses up to tens of picosecond (ps), in order to avoid any damage onto the active medium set inside the amplifier;
- the stretched pulses are sent inside the amplification cavity, where they interacts with the lasing medium (Ti:Sapphire) pumped by a pulsed visible laser, operating at 1 kHz r.r.. The active medium is cooled at a temperature of 0 Celsius degrees. The permanence of such pulses inside the cavity is governed by two Pockels cells;
- the amplified pulses are finally compressed up to $\tau_L \geq 35$ fs, reaching a peak energy value of $\approx$ 2.5 mJ.

3.3 Design of an HHG source

3.3.1 The optical set-up

Once amplified the laser pulses are sent into the optical set-up, shown in figure 3.3, purposely designed to spectrally characterize the HHG source [29].

The laser beam goes though the following path. First of all it is focused by a galilean telescope to reduce the incoming spot size (w).

This optical device consists of a convex lens with a focal length of 300 mm ($1a$) and a double concave one with focal length of -100 mm ($1b$), both designed for near-IR radiation at $\approx$ 800 nm. The telescope reduces the beam spot (radius) from $w = 10$ nm down to $w = 5$ mm.

After the telescope a continuously variable attenuator (CVA) consisting of a $\lambda/2$ retardation plate ($2a$) and a two mirrors ($2b$) set at the Brewster angle [33], is used to split the beam into two, s and p-polarized. The intensity of these beams can be varied continuously, while preserving the temporal structure. The s-polarized beam is sent into the vacuum generation chamber (GC) using two metallic mirrors (3), whereas; the p-polarized beam is frequency doubled by a 1.5 mm Lithium Barium Borate (LBO) non-linear crystal (4). The resulting s-polarized second harmonic (SH) beam is separated from the residual fundamental near-IR beam via two dichroic high reflectivity band-pass mirrors (5), both designed for radiation with $\lambda_{SH} = 400$ nm.

The near-IR beam is focused onto a static (cylindrical shaped) cell filled with inert gas (A) by means of a convex lens with focal length of 250 mm ($6a$), while the SH beam can be focused onto the gas cell by a convex lens with focal length of 170 mm ($6b$) by means of the insertion of a third (removable) band-pass mirror ($6c$). The near-IR and the visible beams are both s-polarized (the non-linear crystal rotates the plane of polarization of the incoming near-IR p-polarized beam for an ammount of 90 degrees)

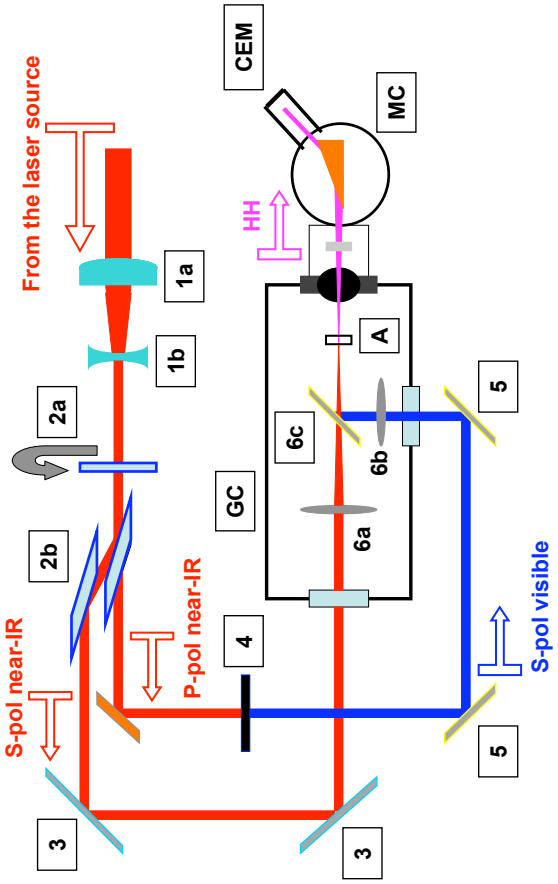

Figure 3.3: Layout of the optical set-up designed for generating HH pulses. The numbers refer to: 1a/b) telescope, 2a/b) CVA, 3) near-IR mirrors, 4) LBO non-linear crystal, 5) visible mirrors, 6a/b) lenses and 6c) removable mirror. The letters refer to A) cell, GC) generation chamber, MC) monochromator and CEM) detector.

3.3.2 The HHG source and the detection system

The HHG source has been designed in collaboration with the Laboratory for Ultra-violet and X-rays Optical Research (LUXOR) located in Padova (Italy) [32]. It consists of two vacuum chambers designed for the generation and the spectral characterization of EUV/SXR radiation. The HHG source consists of a vacuum generation chamber (GC) where the convex lenses and the static gas cell (A) are placed. The cell is mounted onto a three dimensional movable stage, in order to optimized the alignment between the gas target and the incoming optical beam and to control the phase-machting properties of the generated HH.

The generation chamber is connected with a vacuum monochromator chamber (MC) via a bellows, where a 200 nm Al filter (on a mash) is used for absorbing the residual driving beam in order to avoid any radiation damages of the monochromator and to preserve the operating pressure in the monochromator chamber at a value lower than 10^{-5} mbar.

The vacuum monochromator is equipped whit an Au-coated spherical grating and an exit slit. The main specifications of the grating are 576 grooves/mm, 1000 mm radius and blazed-profile. The distances from the grating to the source and from the grating to the slit are 450 mm and 350 mm, respectively. The subtended angle between the incoming HHG beam and the HHG zero order diffracted beam is 135 degree. These parameters have been designed to obtain the HH spectral plane focused on the slit plane. This choice prevent moving the exit slit while scanning the grating.

The grating is mounted onto a piezo-motor, able to change its angular position, in order to monochromatize the incoming HHG beam. A channeltron electron multiplier (CEM) is used as detector [34]. The absorbed EUV/SXR photons generate a signal proportional to the incoming number of photons. It operates at a base pressure of $\approx 10^{-7}$ mbar, to avoid any discharge process, and its operating voltage is set between -1000 and -1900 V.

The characterization of the HH spectral components is obtained by scanning the monochromator. The signal is detected by the channel electron multiplier (CEM). The responses of the Al-filter, monochromator and the gain of the CEM, have been previously calibrated showing a linear transfer

function. All together these parameters allow to determine the number of EUV/SXR photons emitted in the single HH spectral lines, and are reported in figure 3.4.

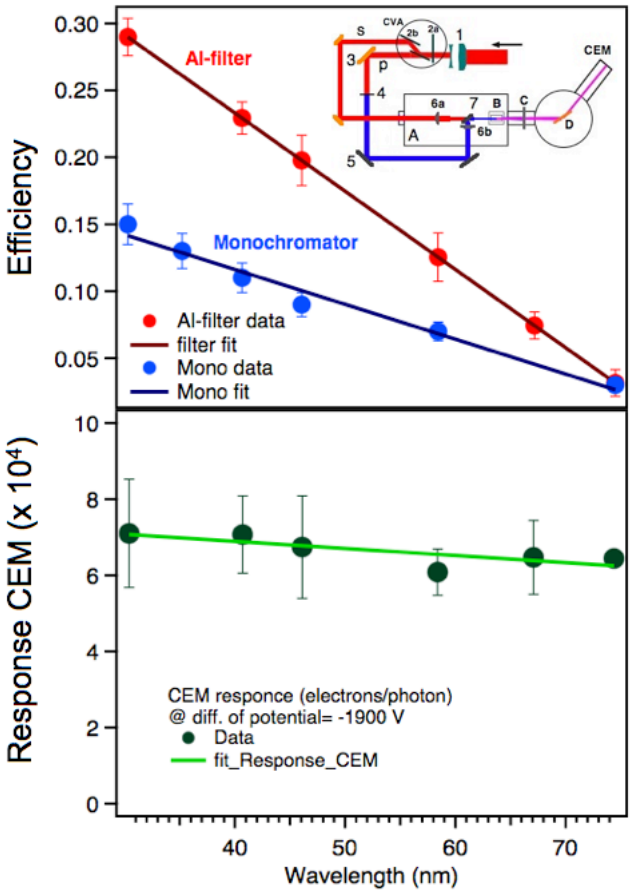

Figure 3.4: Efficiencies of the Al-filter (red dots correspond to the transmission) and the monochromator (blue dots correspond to the reflection) as a function of the wavelength of the incoming EUV radiation. The green dots refer to the response of the CEM in terms of generated electrons per incoming photons at a fixed operating voltage (-1900 V).

3.4 Experimental results

3.4.1 Odd HHG orders

The HHG source has been spectrally characterized using both the fundamental near-IR ($\lambda_0 \approx 800$ nm) beam and its SH.

This paragraph reports the results acquired using the near-IR field. The incoming ≈ 2.5 mJ, ≈ 50 fs pulses have been focused on the inert gas target. The HHG spectra have been generated by neon, argon and xenon, therefore in gas with different ionization potentials I_P, i.e. at 21.54 eV, 15.76 eV and 12.13 eV, respectively [35]. The HHG spectra have been acquired with a spectral accuracy of ≈ 1.0 nm centering the gas cell at the focus position (z_0), previously determined by means of the Foucault's blaze. The data have been acquired as a function of the inert gas, i.e. of I_P. As a consequence of the well known cut-off law (the number of available HH grows linearly with I_P), therefore the number of the available HH depends on I_P.

The operating gas pressure (P) has been varied for estimating the most efficient operating conditions, where the gas starts to re-absorb the EUV/SXR radiation, while the relative distance (Δz) between the focus position (z_0) and the gas cell has been adjusted to obtain the optimal phase-matching conditions.

Therefore Δz is of fundamental importance in order to control the spectral behavior of the generated HH. It contains the knowledge in order to modify and optimize the spectral coherence of the generated HH [22, 41]. These data will be presented in the next chapter.

The following figures 3.5, 3.6 and 3.7 report the HHG spectra generated by the fundamental near-IR beam (800 nm) in neon, argon and xenon with the gas cell centered in z_0. Each spectrum exhibits, as expected, odd HH with photon energies defined by the recursive rule $(2n+1)\hbar\omega_0$ (being n a positive integer number). Tables 3.1, 3.2 and 3.3 refer to the experimental results, in terms of the generated EUV photons, at different gas pressures.

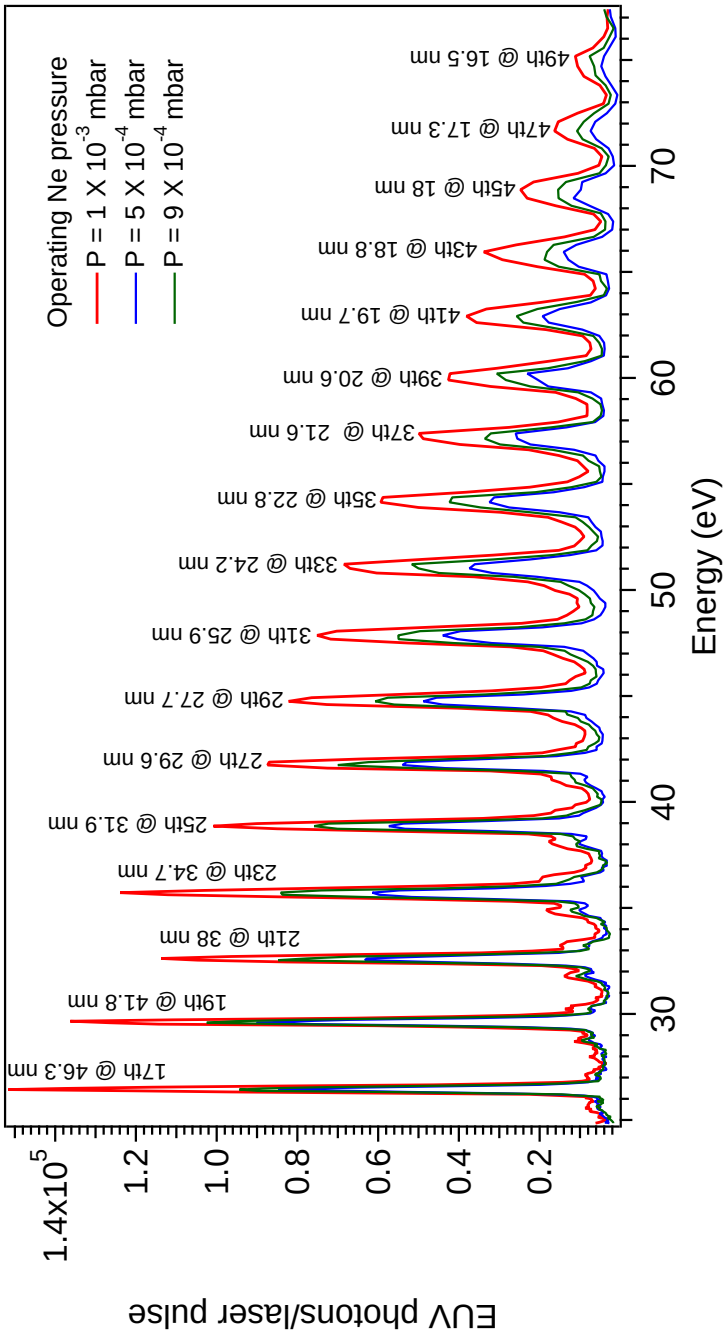

Figure 3.5: Odd HH generated in Ne by near-IR laser pulses ($\lambda_0 \approx 800$ nm) as a function of the gas pressure.

Gas (I_P [eV])	P [mbar]	Order	Photons	λ_0 (nm)	FWHM (nm)
Ne (21.54)	5×10^{-4}	17^{th}	7.7×10^4	46.9	0.427
		19^{th}	8.4×10^4	41.9	0.386
		21^{th}	5.9×10^4	38.0	0.363
		23^{rd}	5.8×10^4	34.7	0.382
		33^{rd}	3.4×10^4	24.9	0.331
		35^{th}	3.0×10^4	22.9	0.294
		37^{th}	2.4×10^4	21.7	0.287
		41^{th}	1.7×10^4	19.7	0.264
		43^{rd}	1.3×10^4	18.9	0.293
		45^{th}	1.1×10^4	18.0	0.342
Ne (21.54)	9×10^{-4}	17^{th}	9.3×10^4	46.9	0.448
		19^{th}	9.6×10^4	41.8	0.406
		21^{th}	7.8×10^4	38.0	0.351
		23^{rd}	8.0×10^4	34.7	0.375
		33^{rd}	4.6×10^4	24.3	0.305
		35^{th}	3.8×10^4	22.9	0.327
		37^{th}	3.1×10^4	21.7	0.297
		41^{th}	2.3×10^4	19.7	0.287
		43^{rd}	1.7×10^4	18.8	0.309
		45^{th}	1.4×10^4	18.0	0.305
Ne (21.54)	2×10^{-3}	17^{th}	1.4×10^5	46.9	0.46
		19^{th}	1.3×10^5	41.9	0.41
		21^{th}	1.0×10^5	38.0	0.379
		23^{rd}	1.1×10^5	34.7	0.397
		33^{rd}	5.9×10^4	24.8	0.362
		35^{th}	5.2×10^4	22.9	0.332
		37^{th}	4.3×10^4	21.7	0.298
		41^{th}	3.4×10^4	19.7	0.288
		43^{rd}	2.9×10^4	18.9	0.291
		45^{th}	2.3×10^4	18.0	0.307

Table 3.1: Odd HH generated (photons refer to photons per pulse) in Ne by near-IR laser pulses ($\lambda_0 \approx 800$ nm) as a function of the gas pressure.

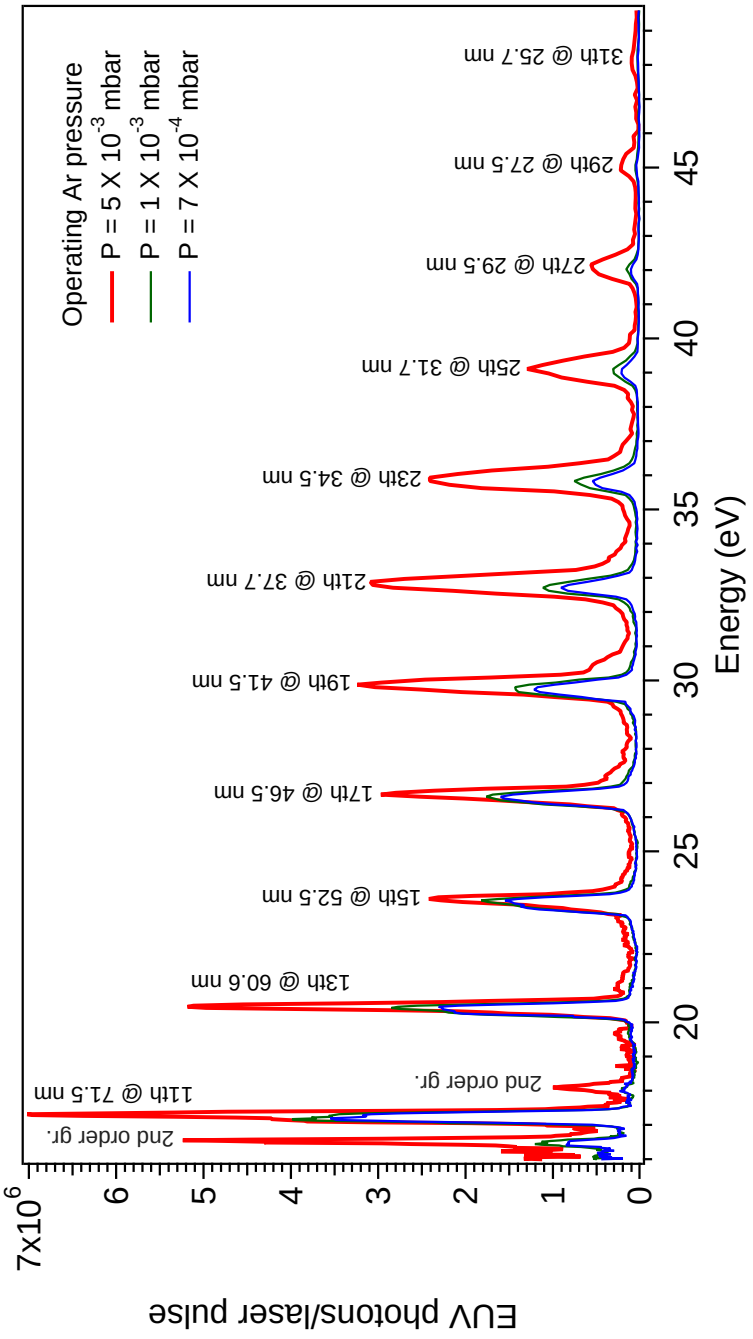

Figure 3.6: Odd HH generated in Ar by near-IR laser pulses ($\lambda_0 \approx 800$ nm) as a function of the gas pressure.

Gas (I_P [eV])	P [mbar]	Order	Photons	λ_0 (nm)	FWHM (nm)
Ar (15.76)	7×10^{-4}	11^{th}	3.7×10^6	72.0	1.075
		17^{th}	1.5×10^6	46.7	0.587
		19^{th}	1.2×10^6	41.7	0.527
		21^{rd}	8.4×10^5	37.9	0.414
		25^{rd}	1.9×10^5	31.7	0.373
		27^{th}	9.0×10^4	29.5	0.301
		29^{th}	2.9×10^4	27.5	0.308
Ar (15.76)	1×10^{-3}	11^{th}	4.1×10^6	72.0	1.107
		17^{th}	1.7×10^6	46.6	0.611
		19^{th}	1.4×10^6	41.7	0.527
		21^{rd}	1.0×10^6	37.9	0.414
		25^{rd}	2.8×10^5	31.7	0.373
		27^{th}	1.3×10^5	29.5	0.301
		29^{th}	3.7×10^4	27.5	0.308
Ar (15.76)	5×10^{-3}	11^{th}	6.0×10^6	71.8	1.039
		17^{th}	2.6×10^6	46.5	0.539
		19^{th}	2.9×10^6	41.5	0.544
		21^{rd}	2.9×10^6	37.8	0.534
		25^{rd}	1.1×10^6	31.7	0.458
		27^{rd}	5.2×10^5	29.4	0.39
		29^{th}	1.8×10^5	27.5	0.344

Table 3.2: Odd HH (photons refer to photons per pulse) generated in Ar by near-IR laser pulses ($\lambda_0 \approx 800$ nm) as a function of the gas pressure.

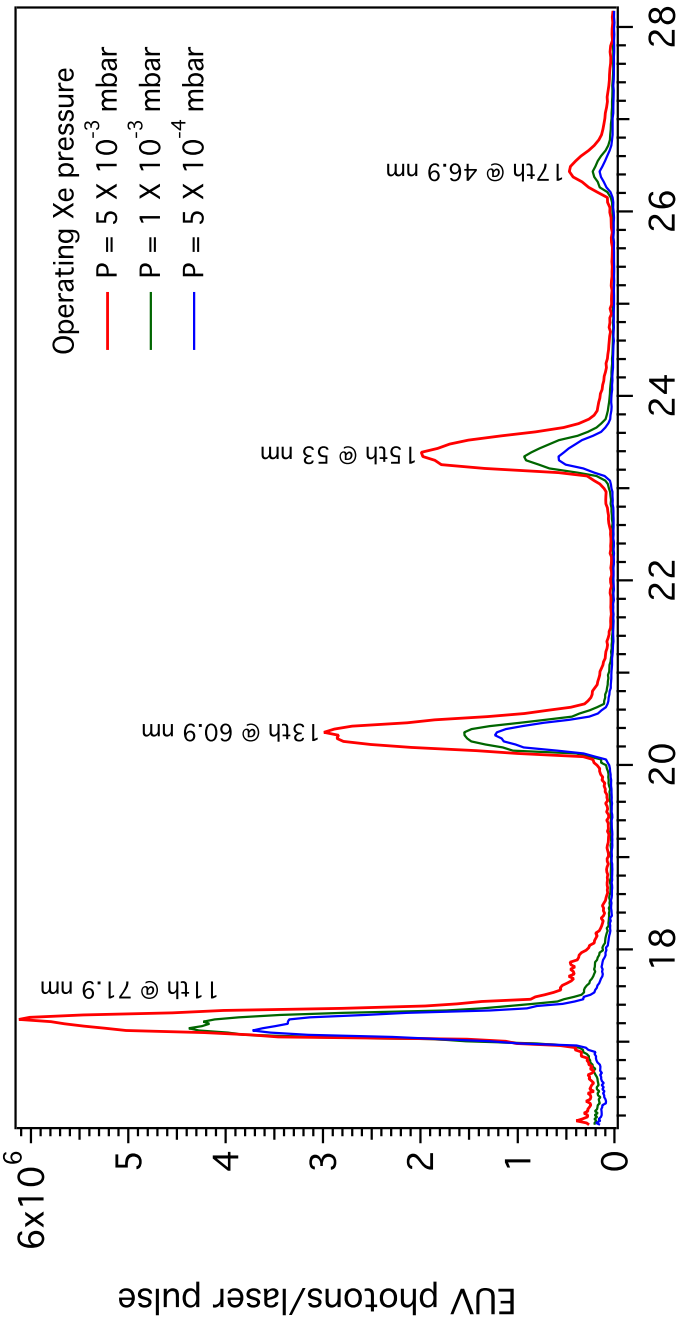

Figure 3.7: Odd HH generated in Xe by near-IR laser pulses ($\lambda_0 \approx 800$ nm) as a function of the gas pressure.

Gas (I_P [eV])	P [mbar]	Order	Photons	λ_0 (nm)	FWHM (nm)
Xe (12.13)	5×10^{-4}	11^{th}	3.7×10^6	72.2	0.968
		13^{th}	1.3×10^6	61.0	0.732
		15^{th}	5.5×10^5	53.0	0.614
		17^{rd}	1.3×10^5	46.9	0.479
Xe (12.13)	1×10^{-3}	11^{th}	4.5×10^6	72.1	0.979
		13^{th}	1.6×10^6	61	0.782
		15^{th}	8.9×10^5	53.1	0.653
		17^{rd}	1.9×10^6	46.9	0.539
Xe (12.13)	5×10^{-3}	11^{th}	5.9×10^6	72.0	0.996
		13^{th}	3.0×10^6	61.0	0.826
		15^{th}	2.0×10^6	53.0	0.694
		17^{rd}	3.0×10^5	46.8	0.589

Table 3.3: Odd HH (photons refer to photons per pulse) generated in Xe by near-IR laser pulses ($\lambda_0 \approx 800$ nm) as a function of the gas pressure.

3.4.2 Even HHG orders

In order to increase the number of available HH, i.e. the degree of tunability of the HHG source, the near-IR beam has been splitted by means of the CVA. The p-polarized near-IR beam, outgoing from the CVA, has been frequency doubled by a 1.5 mm Lithium Barium Borate (LBO) non-linear crystal (4). HH have been generated by means of the s-polarized SH field.

It is well known that only HH with photon energies corresponding to the odd multiplies of the driving frequency can be generated, i.e. those defined by the recursive rule $(2n+1)\hbar\omega_0$ [1, 3]. Therefore, the HH generated using the SH correspond to the even harmonics of the fundamental angular frequency, ω_0, with photon energies defined by the rule $2(2n+1)\hbar\omega_0$. The clear absence of even HH with photon energies equal to $2(2n)\hbar\omega_0$, emphasizes that coherent EUV/SXR photons can be generated (efficiently) via HHG process using the pure SH field. On the other hand, the number of available even HH is lower due both to the lower conversion efficiency of the LBO non-linear crystal (maximally 30%) and to the halving of the driving wavelength.

The three following HHG spectra refer to the non-linear medium response, in terms of the generated EUV photons (per laser pulse) as a function of P.

Depending on I_P, the three noble gases exhibit different spectra. Figure. 3.8 reports the Ne HHG spectrum where 5 HH, from the 18^{th} to the 34^{th}, i.e. in the range between $\approx$ 45 nm and $\approx$ 23 nm (between $\approx$ 27 eV and $\approx$ 54 eV) can be observed. Neon exhibits a kind of standard structure for HHG spectra as a plateau (22^{nd} and 26^{th} HH), an exponential cut-off (30^{th} and 34^{th} HH), while the 18^{th} HH represents the perturbative region to the spectrum. The number of generated EUV photons increases at higher values of pressure, up to 5×10^{-3} mbar, i.e. it is not easy to observe a clear re-absorption value.

Figure 3.9 shows the Ar HHG spectrum. It is possible to note that it does not exhibit the same behavior of neon. It possible to recognize 3 HH, from the 14^{th} to 22^{nd} one, without a clear non-perturbative structure (appearance of a plateau region), but rather a linear (perturbative) scaling law. This behavior is expected. In fact γ_K is ≥ 1, corresponding to a not well defined non perturbative condition. Further discussions concerning this fact will be presented in the next chapters. As in the previous case, the number of EUV photons increases, when P arises.

Figure 3.10 shows the HHG spectrum for Xe, i.e. using an inert gases with a lower I_P value. As a consequence the HHG spectrum has a reduced number of HH. Only two HH, i.e. the10^{th} and the 14^{th}, are clearly detected showing how a higher P value does not produced an evident re-absorption effect.

As done in the previous paragraph, the table 3.4 refers to the results shown in the spectra, in terms of EUV coherent pulses. These results emphasize how HH can be, efficiently, generated by means of the SH pulses ($\lambda_{SH} \approx$ 400 nm) with photon energies defined by the expected recursive rule $2(2n+1)\hbar\omega_0$. The number of generated photons are comparable (or higher) that those generated by the near-IR. In order to report a meaningful comparison between these two processes, the gas pressure and the geometrical parameters have been kept constant.

The clear absence of even HH with photon energies defined by the re-

cursive rule $2(2n)\hbar\omega_0$ emphasizes the fact that coherent EUV/SXR photons can be, efficiently, generated using a pure SH field (400 nm). Noteworthy here is to underline that the presented HH spectra generated by a pure SH field are significantly different from the data reported by several groups and generated by means of a two-color combination scheme [27, 28], i.e. a strong fundamental optical field plus its (weak) SH [**?**].

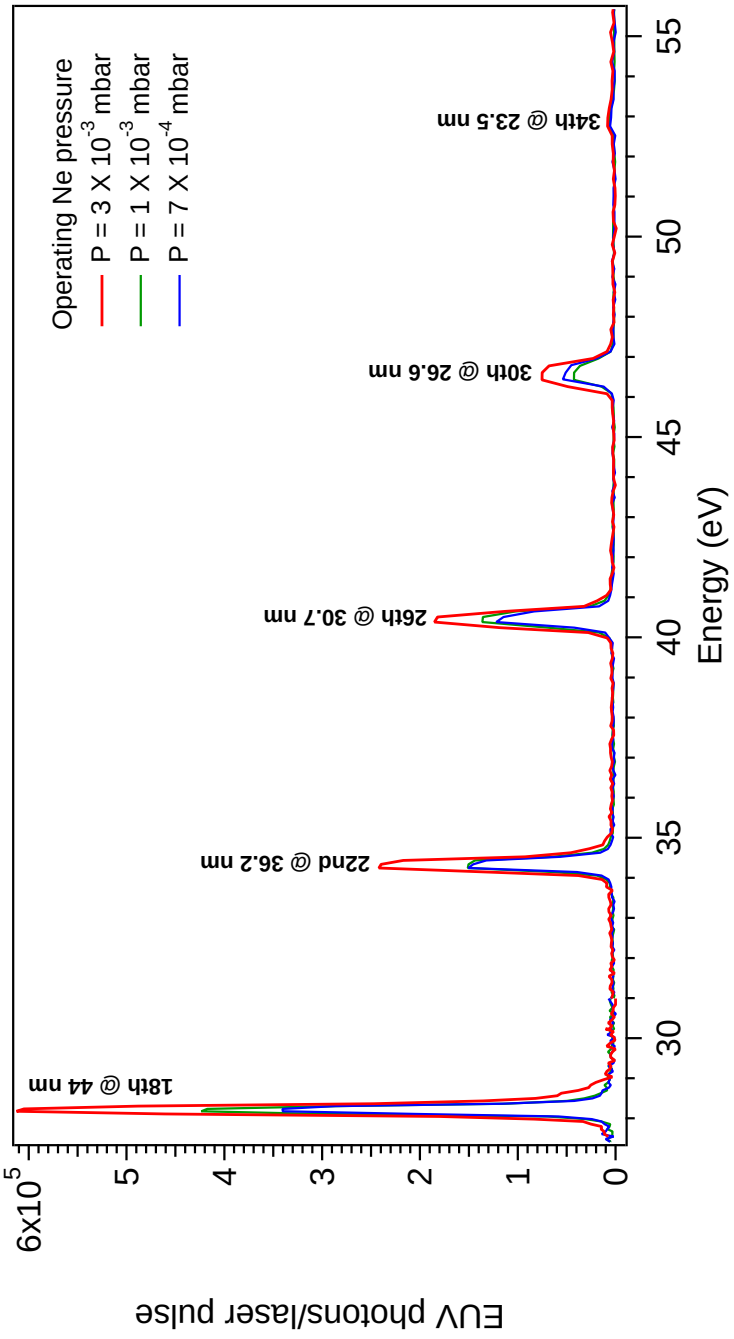

Figure 3.8: Even HH generated in Ne by visible pulses ($\lambda_{SH} \approx 400$ nm) as a function of the gas pressure.

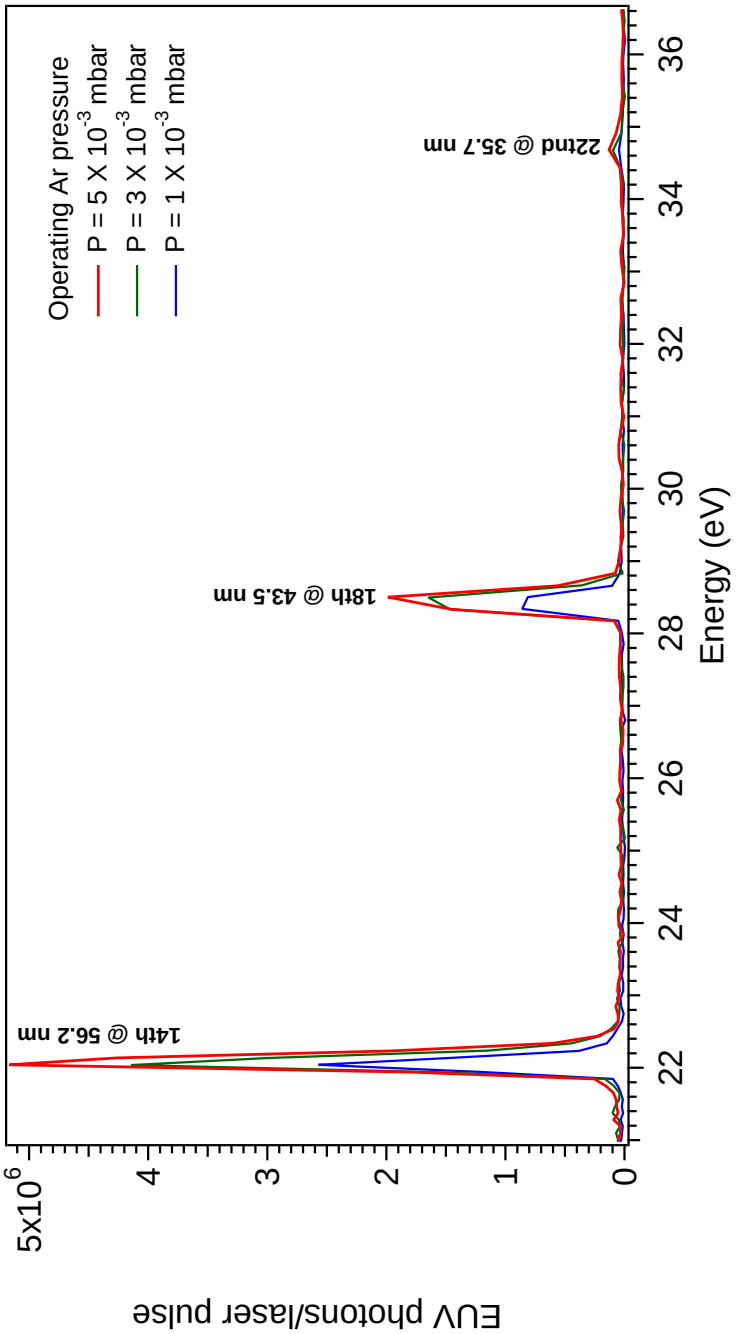

Figure 3.9: Even HH generated in Ar by visible pulses ($\lambda_{SH} \approx 400$ nm) as a function of the gas pressure.

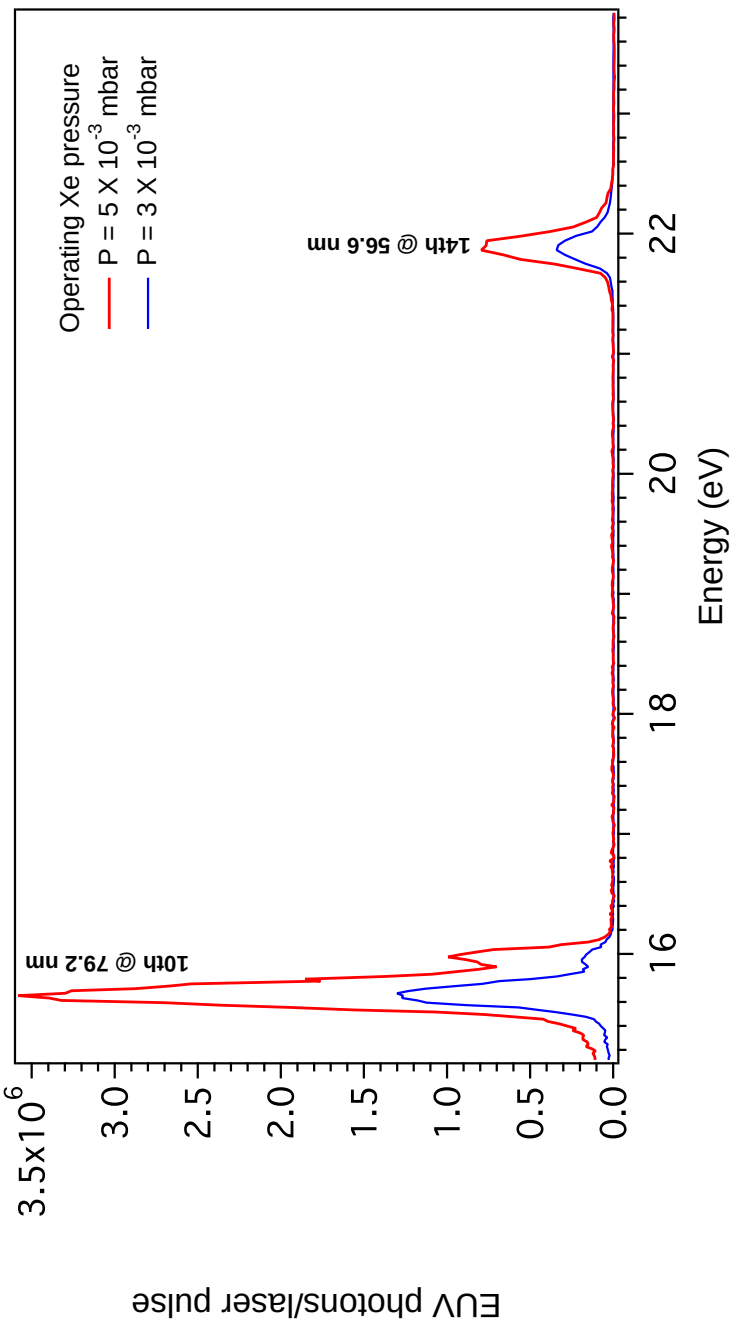

Figure 3.10: Even HH generated in Xe by visible pulses ($\lambda_{SH} \approx 400$ nm) as a function of the gas pressure.

Gas (I_P [eV])	P [mbar]	Order	Photons	λ_0 (nm)	FWHM (nm)
Ne (21.54)	7×10^{-4}	18^{th}	3.6×10^5	43.9	0.303
		22^{th}	1.6×10^5	36.1	0.262
		26^{th}	1.3×10^5	30.6	0.24
		30^{th}	5.7×10^4	26.6	0.259
Ne (21.54)	1×10^{-3}	18^{th}	4.4×10^5	43.9	0.294
		22^{th}	1.6×10^5	36.1	0.293
		26^{th}	1.4×10^5	30.6	0.264
		30^{th}	4.5×10^4	26.6	0.271
Ne (21.54)	5×10^{-3}	18^{th}	6.2×10^5	43.9	0.348
		22^{th}	2.5×10^5	36.1	0.308
		26^{th}	1.9×10^5	30.6	0.27
		30^{th}	8.2×10^4	26.6	0.294
Ar (15.79)	1×10^{-3}	14^{th}	2.5×10^6	56.2	0.431
		18^{th}	1.1×10^6	43.6	0.303
Ar (15.79)	3×10^{-3}	14^{th}	4.1×10^6	56.2	0.474
		18^{th}	1.9×10^6	43.6	0.359
Ar (15.79)	5×10^{-3}	14^{th}	5.2×10^6	56.1	0.508
		18^{th}	2.2×10^6	43.6	0.372
Xe (12.13)	3×10^{-3}	10^{th}	1.2×10^6	79.1	0.88
		14^{th}	3.3×10^6	56.6	0.554
Xe (12.13)	5×10^{-3}	10^{th}	3.1×10^6	79.1	0.993
		14^{th}	7.9×10^6	56.6	0.567

Table 3.4: Even HH (photons refer to photons per pulse) generated by visible pulses ($\lambda_{SH} \approx 400$ nm) in Ne, Ar and Xe as a function of the gas pressure.

3.5 Discussion

The existing literature accounts for several experiments where coherent EUV/SXR photons are generated using optical fields characterized by single photons frequency (ω_0), corresponding to the near-IR or the mid-IR spectral regions. In addition, several groups have been demonstrated the possibility for generating HH via a two-color scheme, i.e. by means of a mixed photon frequencies, for example using the fundamental laser beam plus its SH. These processes occur in a dynamical condition corresponding to a Keldysh parameter much lower than 1 ($\gamma_K \ll 1$), i.e. in a tunneling (non-perturbative) regime where the quasi-static approximation is still rightful. When the atomic system interacts with the SH pulses, generated by a conventional Ti:Sa laser, such multi order non-linear optical process takes place between the tunneling and the the MPI dynamical conditions, characterized by $\gamma_K \geq 1$. in a not well defined regime (called hybrid or intermediate) corresponding to $\gamma_K \geq 1$, being the SH pulse energy is lower ($\approx 30\%$) than the near-IR one due to the conversion efficiency of the non-linear crystal.

The experimental results presented in the previous paragraphs (see figures 3.11, 3.12 and 3.13 and tables 3.4 and 3.5) emphasize how the HH generated by a pure SH field are comparable or higher (in terms of the number of generated EUV photons) than those produced by the near-IR. This behavior can be qualitatively attributed to the diffusion mechanism, being the two optical periods different.

A proper definition of the efficiency for the HHG processes requires considering that the transition amplitude strongly depends on the spectral and temporal properties of the optical field. This is also evinced by the fact that the non-linearity order in HHG processes can not be deduced from the measure of the HH intensity (in terms of the generated photons) as in most of the non-linear optical processes, where the conversion efficiency do not depend on the intensity of the incoming radiation field (perturbative limit). For this reason the efficiency of the HHG process has to be evaluated by measuring the number of generated EUV/SXR photons at the same Keldysh's parameter, γ_K, i.e. in the same dynamical conditions.

It is clear that this condition can not be satisfied using the laser field and its SH. Within our experimental conditions, the efficiency for generating HH, using the near-IR laser field and its SH, can be performed only for different values of γ_K, i.e. ≈ 0.25 for near-IR pulses and ≈ 1 for SH ones. This means that these data proof the previsions of Lewenstein's model about the role played by diffusion, but in different dynamical regimes.

Figure 3.11 refers to the HH spectra, generated in the three different inert gases (Ne, Ar and Xe), using the fundamental laser beam (red lines) or its SH (blue lines) keeping constant the gas pressure and the geometrical parameters, in order to avoid spurious effects depending on different phase matching conditions (see next chapter). By comparing the HHG spectra at ω_0 and $2\omega_0$ it is clear that the HH generated at $2\omega_0$ are significantly more intense, in terms of generated photons.

In order to gain a more quantitative knowledge concerning the weight of the diffusion mechanism in HHG processes, a suitable phenomenological model is mandatory. The aim of such a model is to compare the efficiency of HHG process using optical fields with different wavelength as the near-IR ($\lambda_0 = 800$ nm) and its SH ($\lambda_{SH} = 400$ nm) in the same dynamical conditions, i.e. at the same γ_K.

A possible choice is to start from the semi-classical three steps model, focusing the attention onto the non-linear ionization process (1^{st} step), well described by the ADK model in the tunneling regime [1, 15]. To model the efficiency in an arbitrary dynamical regime it is necessary to extend the ADK ionization rate $\Gamma_{ADK}(t)$ to arbitrary γ_K.

For $\gamma_K \geq 1$, i.e. hybrid regime, Yudin and Ivanov have developed an *ad-hoc* model for describing ionization processes, which demonstrates the strict dependence of the optical process on the phase θ_L [36]. Unfortunately, the rate equations of the Y-I model are not of easy solution, so it is necessary to define a new ionization rate.

The transition between an initially bound state $|i\rangle$ and a final continuum one $|f\rangle$ has been derived in the framework of the Landau-Dykhne theory [13]. The corresponding transition rate is (see chapter 2),

$$\Gamma(t) \propto \exp\Big[-2Im\Big(S(\mathbf{p}, I_P)\Big)\Big], \tag{3.1}$$

being $S(\mathbf{p}, I_P)$ the usual semi-classical action, which can be written,

$$S(\mathbf{p}, I_P) = \int_{t_1}^{\tilde{t}} d\tau [E_f(\tau) - E_i(\tau)]. \tag{3.2}$$

The point $\tilde{t}$ has to satisfy the condition $E_i(\tilde{t}) = E_f(\tilde{t})$ and can it be evaluated by means of the saddle-point method, i.e. looking for a solution of the equation $\partial_{\tilde{t}} S(\mathbf{p}, I_P) = 0$. t_1 is any point on the temporal axis. The formal solution is,

$$\tilde{t} = \frac{1}{\omega_0} \arcsin \left[\gamma_K \left(\frac{p_{\parallel}}{\sqrt{2I_P}} + i\sqrt{1 + \frac{p_{\perp}^2}{2I_P}} \right) \right] \tag{3.3}$$

As done in [37] it is possible to set $\mathbf{p} = 0$, i.e. to suppose that the ionized electron is promoted into the continuum with null velocity. After some algebraic manipulation the equation for $\Gamma(t)$ at arbitrary values of γ_K results,

$$\Gamma(t) \propto exp\left[-\frac{2I_P}{\omega_0} f(\gamma_K) \right], \tag{3.4}$$

being the function $f(\gamma_K)$ dependent of γ_K as,

$$f(\gamma_K) = arccosh\left[\sqrt{1+\gamma_K^2} \left(1 + \frac{1}{2\gamma_K} \right) - 2\sqrt{1 + \frac{1}{\gamma_K}} \right]. \tag{3.5}$$

Therefore, it is possible to compute the corresponding $w_{ion}(t)$, i.e. the probability amplitude to ionize an initially bound electron at time t_{ion}. As underlined in chapter 2 the electron can travel along a long path, if ionized between 0 and $T/20$ (≈ 18 degrees), or a short path if ionized between $T/20$ and $T/4$. The q-order harmonic (with photon energy equal to $q\hbar\omega_0$) results from the interference of $w_{ion}(t_s)$ and $w_{ion}(t_l)$.

Therefore, it is possible to compute the behaviour of the function, η_{eff}, as suggested by A. Gordon and F. Kaertner, and related to the HHG efficiency [38]:

$$\eta_{eff} = {\omega_0}^3 |w(t_s) w(t_l)|^2, \tag{3.6}$$

being $w(t_s)$ and $w(t_l)$ the free electron densities for short and long quantum paths. η_{eff} is defined as the interference term between these contributions, while ${\omega_0}^3$ accounts for the electronic wavefunction diffusion process (it scales as T^3).

The acquired data are reported in table 3.5 along with the estimated power of odd and even HH and the corresponding γ_K. Even harmonics exhibit always a higher intensity and a corresponding efficiency, although γ_K is larger than for the odd harmonics. This fact emphasizes how HHG is not strictly dependent on the pulse energy, but rather both on the dynamical regime, where it takes place, and on the diffusion process, which is lower for shorter wavelengths. This behavior proves the expected contribution of the diffusion mechanism at lower driving wavelengths, as predicted in the Lewenstein's model [19].

In order to give a meaningful comparison, the previous phenomenological model has been used to evaluate the generalized efficiency for odd and even HH in a well defined tunneling regime. These values have been computed at the same Keldysh parameters increasing the SH pulse energy up to match the values of γ_K, but preserving the temporal structure (both simulated fields have a temporal duration of 50 fs). Table 2 reports the Keldysh parameters (γ_K) evaluated in order to compute the phenomenological efficiency (fourth column) for each HH. These results indicate that at 400 nm the HH are generated with a significantly higher efficiency.

Gas (I_P [eV])	Order	P (W)	Efficiency	γ_K
Xe (12.13)	10	8.99×10^{-9}	1.71×10^{-7}	0.8
	11	4.35×10^{-9}	1.98×10^{-9}	0.21
	13	2.51×10^{-9}	1.14×10^{-9}	0.21
	14	2.76×10^{-9}	5.52×10^{-9}	0.8
	15	2.08×10^{-10}	9.45×10^{-10}	0.21
Ar (15.76)	13	3.59×10^{-9}	1.63×10^{-9}	0.24
	14	1.83×10^{-8}	3.66×10^{-8}	1
	17	2.15×10^{-9}	9.77×10^{-10}	0.24
	18	9.1×10^{-9}	1.82×10^{-8}	1
	19	2.51×10^{-10}	1.14×10^{-10}	0.24
Ne (21.54)	17	6.33×10^{-10}	2.88×10^{-10}	0.28
	18	1.89×10^{-9}	3.78×10^{-9}	1.17
	19	6.63×10^{-10}	3.01×10^{-10}	0.28
	21	5.73×10^{-10}	2.6×10^{-10}	0.28
	22	8.22×10^{-10}	1.64×10^{-9}	1.17

Table 3.5: The five columns refer, respectively, to i) the inert gas, ii) the harmonic order , iii) the measured HH power, iv) the corresponding efficiency and v) the estimated Keldysh parameters.

Gas (I_P [eV])	Order	γ_K	Gen. efficiency
Xe (12.13)	10	0.166	1.45×10^{-3}
	11	0.168	1.06×10^{-4}
	13	0.168	9.53×10^{-5}
	14	0.166	1.45×10^{-3}
Ar (15.76)	13	0.191	1.41×10^{-4}
	14	0.201	1.11×10^{-3}
	17	0.191	1.2×10^{-4}
	18	0.201	9.86×10^{-4}
Ne (21.54)	17	0.224	1.74×10^{-4}
	18	0.227	1.26×10^{-3}
	21	0.224	1.71×10^{-4}
	22	0.227	1.21×10^{-3}

Table 3.6: The four columns refer, respectively, to i) the inert gas, ii) the harmonic order, iii) the Keldysh parameters used in the simulation (γ_K) in order to compute the theoretical efficiency (expressed in arbitrary units).

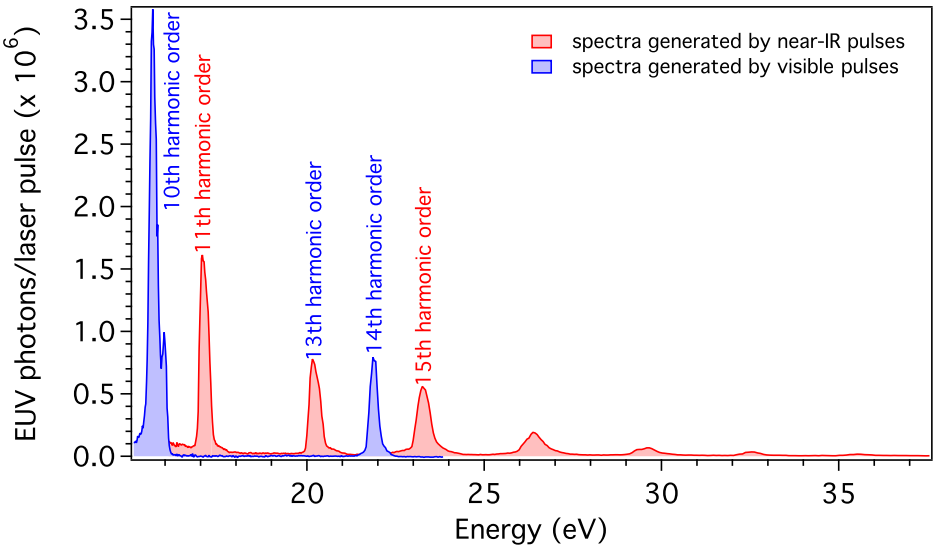

Figure 3.11: HH generated by near-IR field (red spectra) and SH (blue spectra) in Xe at pressure of 3×10^{-3} mbar. Data refer to coherent photons generated in the gas cell.

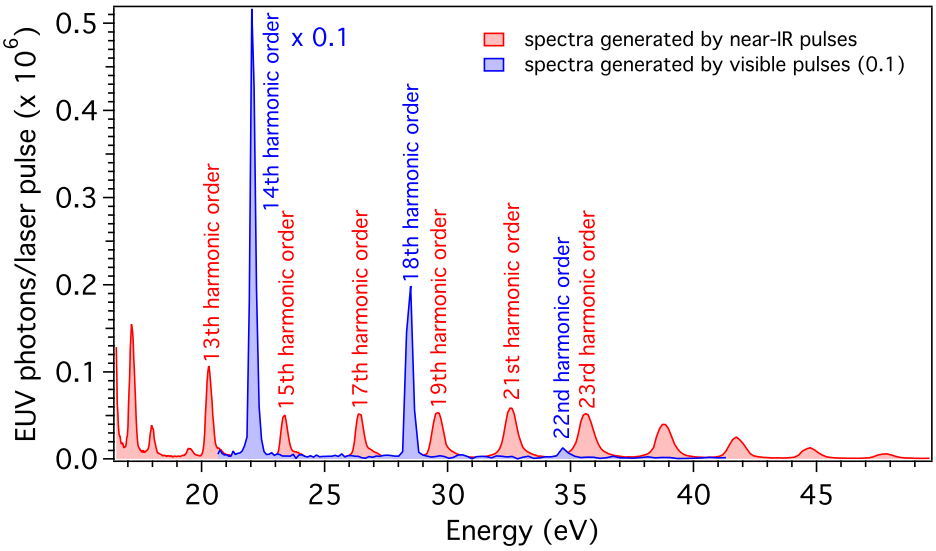

Figure 3.12: HH generated by near-IR field (red spectra) and SH (blue spectra) in Ar at pressure of 5×10^{-3} mbar. Data refer to coherent photons generated in the gas cell.

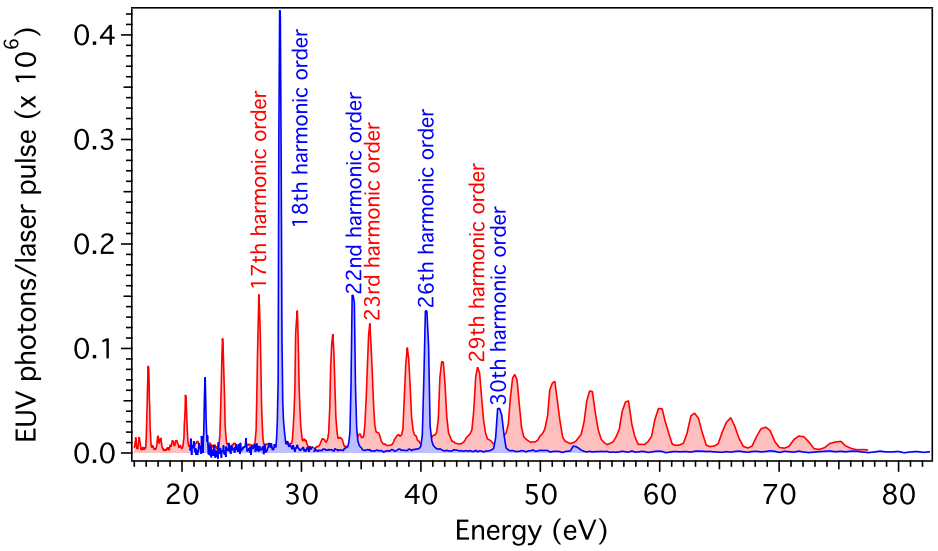

Figure 3.13: HH generated by near-IR field (red spectra) and SH (blue spectra) in Ne at an operating pressure of 1×10^{-3} mbar. Data refer to coherent photons generated in the gas cell.

3.6 Conclusion

The experimental results, presented in this chapter, substantiate the Lewenstein's conjecture that the efficiency (in terms of generated EUV photons) depends on the electron wavefunction diffusion mechanism, that scales with the optical period of the interacting field. This fact emphasize how HHG processes do not depend on the available pulse energy, but rather on the diffusion mechanism of the electron wavefunction, which results more localized when the atomic electrons interact with photons corresponding to shorter wavelengths pulses. Such experimental results represent the first detailed analysis concerning the role of these diffusion process involved in the generation of HH pulses [39]. A detailed overview on the experimental set-up, as the laser source, the optical layout and the experimental vacuum chamber, has been also presented.

4

The electron quantum paths

4.1 Introduction

Both the classical and the quantum descriptions of the HHG processes are suitable for modeling the dynamics of the excited electron (2^{nd} step) in terms of classical trajectories or quantum paths, respectively [1, 3]. The recoiling electron can travel along two subset of such trajectories known as the short and the long quantum paths, which are characterized by a proper return time ($\tau_{s,l}$) equal to $\tau_s \approx T/2$ (short path) and $\tau_l \approx T$ (long path), being T the period of the optical field.

In the framework of the SFA, M. Lewenstein and coauthors [19] have emphasized how the quantum paths with return times longer than one optical cycle, i.e. $\tau > T$, do not significantly contribute to the emission of HH. The overlap between the wavefunction of the involved electron and the parent ion suffers of a dramatic decrement when the return time increases, because of the diffusion process. Accordingly to the Lewenstein's model, the coherent EUV/SXR photons with energies corresponding to the plateau region, are created by means of the quantum interference between the short and long paths, being the accumulated kinetic energy degenerated [1, 19].

On the other hand, any physical process can be modeled in the framework of the Feynman's path integral formulation of quantum mechanics [40], i.e. as the coherent overlap of different quantum paths connecting the initial $|i\rangle$ and final $|f\rangle$ states of the involved system. Each of these paths is unique,

being characterized by a proper phase term dependent on the semi-classical action $S[\mathbf{x}(t)]$ and equal to $\exp\left(\frac{-iS[\mathbf{x}(t)]}{\hbar}\right)$ [40]. An exponential term, dependent on $S(\mathbf{p}, t, \tau)$, has to be taken into account for characterizing the short and the long quantum paths. This phase, known as dipole one, contains the set of informations knowledge concerning the electron propagation in the presence of the optical field and it has to be evaluated by means of the saddle-points method [19].

In the perturbative harmonic generation (HG) processes (as example in the non-linear crystals), the coherence properties of the optical field are transmitted to the generated fields.

In order to generate HH in inert gases the optical field has to be focused onto the non-linear medium. Its intensity depends on the axial coordinate z as $I(z) = I_0\left[1 + (z/z_R)^2\right]^{-1}$, and the corresponding quiver potential U_P scales on z by means of the same law, because of its linearly dependence on $I(z)$. Since the semi-classical action, evaluated onto the stationary points of the electronic momentum $\mathbf{p}_{st}(t, \tau)$, depends on U_P, the dipole phases can be manipulated varying z, i.e. modifying the relative position (Δz) between the laser focus and the non-linear medium [41, 42].

This means these dipole phases corresponding to different quantum paths, i.e. the coherence properties of the generated HH can be controlled by means of a macroscopical variation of Δz.

The aim of this chapter is to report the acquired experimental data concerning the behavior of the spectral profiles of odd and even HH varying Δz in order to understand how the coherence properties changes when HH are generated by means of a near-IR ($\lambda_0 \approx 800$ nm) laser field or its SH ($\lambda_{SH} \approx 400$ nm).

4.2 Experimental results

4.2.1 Spectral behavior of odd high-order harmonics

The simplest way to control and to optimize the coherence properties of the generated HH is to change the axial geometry of the interaction volume between the optical field and the non-linear medium, i.e. varying macroscopically the relative distance (Δz) between the gas cell and the focal position [11]. As shown in chapter 3, the gas cell is mounted onto a 3D stage for optimizing the alignment with the interacting laser beam. In addition, it is able to control Δz moving the gas cell along the axial direction (z) keeping fixed the focal position z_0 inside the generation chamber (GC).

In order to gain a preliminary qualitative analysis on the dependence of the HH spectral profiles on Δz, the following spectra (figures 4.1 and 4.2) have been acquired centering the gas cell at z_0 (black spectra) and at ± 3 mm from z_0 (blue and red spectra) keeping fixed the operating gas pressure. These data have been acquired in neon (from the 17^{th} to the 49^{th} harmonic orders) and in argon (from the 13^{th} to the 29^{th} harmonic orders), with a spectral accuracy of 1 nm, at a pressure of 2×10^{-3} mbar and of 9×10^{-3} mbar, respectively.

When the gas cell is placed at $\Delta z = +3$ mm (blue spectra) the generated HH exhibit both a broader profile and a consequent blue-shift behavior, i.e. a shift to higher energies, more marked in the cut-off region of the neon spectrum. On the other side, the HH spectrum acquired in argon when the gas cell is set at $\Delta z = -3$ mm (red spectra) exhibits narrower profiles. At this position such spectrum is omitted in neon, being irrelevant in terms of the low number of the generated photons.

Table 4.1 reports the data for five harmonics, i.e. from the 37^{th} to the 45^{th} harmonic orders, generated in Ne with the gas cell centered in z_0 and $\Delta z = 3$ mm, respectively. In addition Table 4.2 reports the data for three harmonics, i.e. from to the 13^{th} to the 29^{th} harmonic orders, generated in Ar with the gas cell centered in $\Delta z = 3$ mm (blue spectrum), z_0 (black spectrum) and $\Delta z = -3$ mm (red spectrum), respectively.

The data reported in the Table 4.1 refer both to the increase of the FWHM and to the consequent blue-shift behavior, observed in the cut-off

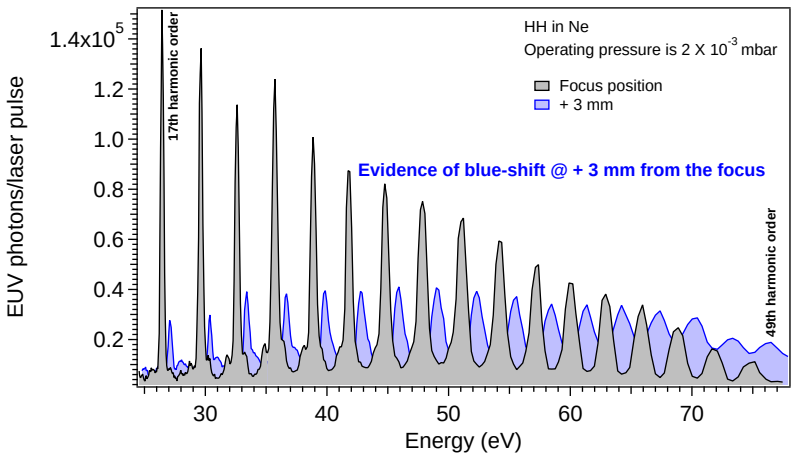

Figure 4.1: HH generated in Ne at a pressure of 2×10^{-3} mbar. The black spectrum refers to the HH generated in gas cell centered in z_0, while the blue one refers to a relative distance $\Delta z = 3$ mm.

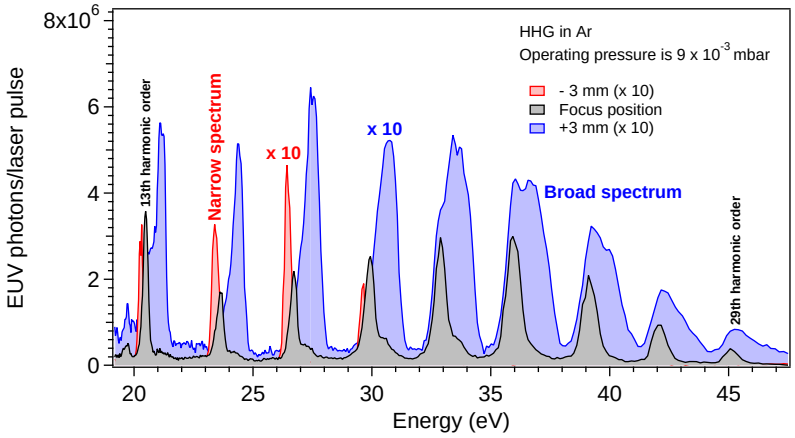

Figure 4.2: HH generated in Ar at a pressure of 9×10^{-3} mbar. The black spectrum refers to the HH generated in gas cell centered in z_0, while the blue and red ones refers to $\Delta z = 3$ mm and $\Delta z = -3$ mm, respectively.

Δz (mm)	P [mbar]	Order	Photons	λ_0 (nm)	FWHM (nm)
0	2×10^{-3}	37^{th}	4.32×10^4	21.68	0.3
		39^{th}	3.74×10^4	20.65	0.3
		41^{st}	3.43×10^4	19.7	0.29
		43^{rd}	2.91×10^4	18.82	0.29
		45^{th}	2.26×10^4	18.02	0.31
+3	2×10^{-3}	37^{th}	1.88×10^4	21.22	0.34
		39^{th}	1.76×10^4	20.21	0.32
		41^{st}	1.58×10^4	19.29	0.34
		43^{rd}	1.36×10^4	18.44	0.34
		45^{th}	1.27×10^4	17.67	0.35

Table 4.1: Spectral properties of some HH generated in Ne at a pressure of 2×10^{-3} mbar with the gas cell centered in the focus or placed at +3 mm, respectively.

region of the neon spectra. As an example, the 39^{th} harmonic exhibits an increase of the FWHM equal to ≈ 0.05 nm and a blue-shift of ≈ 0.44 nm, i.e. ≈ 1.3 eV, with a still appreciable number of generated EUV photons (higher than 1×10^4).

Taking advantage on such behavior it is possible to increase the degree of tunability in the cut-off region, leading to a quasi continuum source of coherent EUV photons between $\approx$ 50 eV and $\approx$ 75 eV, by means of a macroscopical change of Δz.

Table 4.1 shows also the increase of the FWHM and the consequent blue-shift, observed in the plateau region of the argon spectra. At $\Delta z = +3$ mm, for example, the 17^{th} harmonic suffers both of a broadening of its FWHM of ≈ 0.48 nm and a blue shift from ≈ 46.41 nm to ≈ 45.14 nm, with a total amount of ≈ 0.7 eV. The profile of the generated HH can be considered, in first approximation, as gaussian (black spectra). Nonetheless, the number of generated EUV photons (per pulse) degrades when gas cell is placed before z_0 with a consequence narrow spectral profile (red spectrum). In order to gain more information, the spectral behavior of a single harmonic order has been acquired (figure 4.3), step by step, with an accuracy of 0.5 mm when

Δz (mm)	P [mbar]	Order	Photons	λ_0 (nm)	FWHM (nm)
-3	9×10^{-3}	15^{th}	3.2×10^5	52.93	0.62
		17^{th}	4.39×10^5	46.84	0.47
		19^{th}	1.74×10^5	41.84	0.38
0	9×10^{-3}	15^{th}	1.41×10^6	52.58	0.62
		17^{th}	1.87×10^6	46.41	0.49
		19^{th}	2.15×10^6	41.43	0.54
$+3$	9×10^{-3}	15^{th}	4.44×10^5	50.9	0.89
		17^{th}	5.81×10^5	45.14	0.97
		19^{th}	4.94×10^5	40.51	1.1

Table 4.2: Spectral properties of some HH generated in Ar at a pressure of 9×10^{-3} mbar with the gas cell centered in the focus or placed at ± 3 mm, respectively.

moving the gas cell.

The black spectral profile (ticker black line) refers to the 23^{rd} harmonic generated in neon. It has been acquired keeping fixed the pressure at 1×10^{-3} mbar with the gas cell centered at the focus position ($\Delta z = 0$). Here the number of generated EUV photons (per pulse) is $\approx 5 \times 10^4$. The red line refers to the spectral profile acquired with the gas cell set before at $\Delta z = -1$ mm. As expected it exhibits a narrow profile and a lower number of generated photons ($\approx 5 \times 10^3$ photons). Moreover, the profile undergoes to a progressive blue-shift, i.e. the harmonic profile becomes centered at higher energies values when moving the gas cell from $\Delta z = 3$ mm (dark blue profile) to $\Delta z = 4$ mm (violet profile), while the number of generated photons remain higher than 1×10^3.

In order to gain more informations concerning the dependence of these spectral profile on the semi-classical action, $S_{st}(t, \tau)$, i.e. on the dipole phase, it is mandatory to observe if the even HH, generated using the SH pulses in a different dynamical regime ($\gamma_K \approx 1$), exhibit the same spectral behavior.

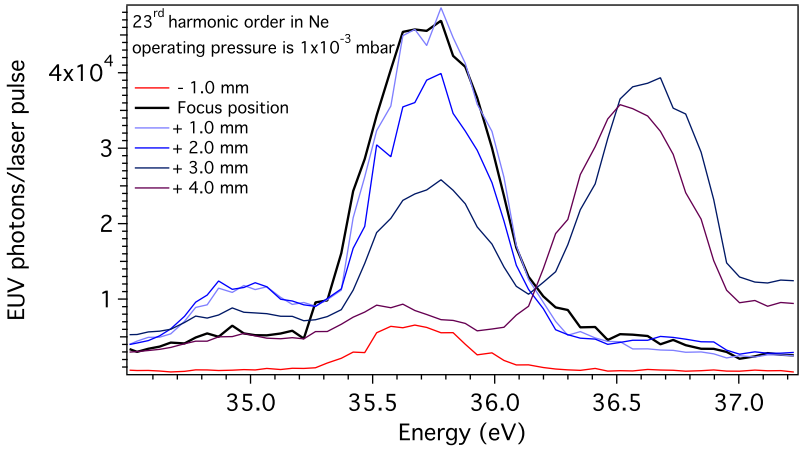

Figure 4.3: Spectral behavior of the 23^{rd} harmonic generated in Ne at a pressure of 1×10^{-3} mbar. The red line refer to the profile at $\Delta z = -1$ mm, while the dark blue one at $\Delta z = 3$ mm. The black profile has been acquired in the focus position.

4.2.2 Spectral behavior of even high-order harmonics

By means of the experimental set-up, described in chapter 3, it is possible to switch the driving field from the fundamental laser beam ($\lambda_0 \approx 800$ nm) to its SH ($\lambda_{SH} \approx 400$ nm), generating HH with photon energies corresponding to the even multiplies of ω_0. Keeping constant the gas pressure, the spectral profiles of a single HH, generated in neon and the other in argon, have been acquired with a spectral accuracy of 0.5 nm. The spectra are reported in the figure 4.4.

They refer to the 18^{th} harmonic order generated in neon (Figure 4.4) and argon (Figure 4.5) at the same pressure (1×10^{-3} mbar), respectively. The black profiles have been acquired with the gas cell centered in z_0, exhibiting a number of EUV photons (per pulse) equal to $\approx 5 \times 10^5$. These coherent EUV photons have been generated in a not well defined dynamical regime, being the corresponding Keldysh's parameters higher than 1, i.e. $\gamma_K \geq 1$. Nonetheless, the number of photons remains still appreciable, due to the limited diffusion processes (see chapter 3).

It results unambiguously clear that these spectra differ from those gen-

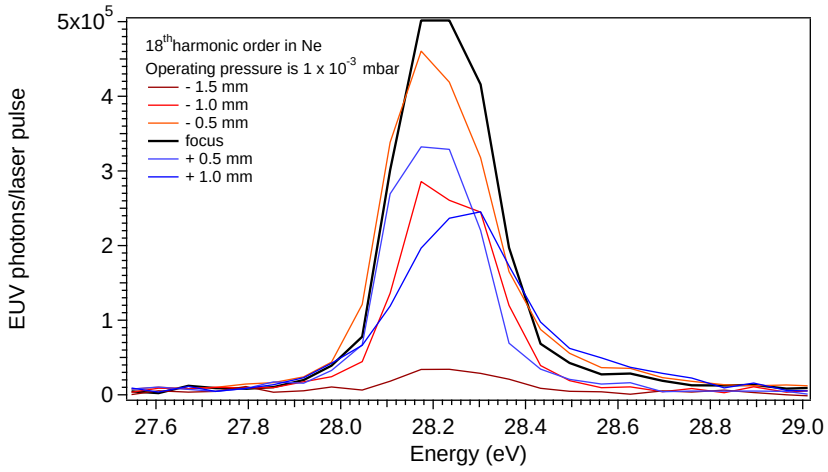

Figure 4.4: Spectral behavior of the 18^{th} harmonic generated in Ne at a pressure of 1×10^{-3} mbar.

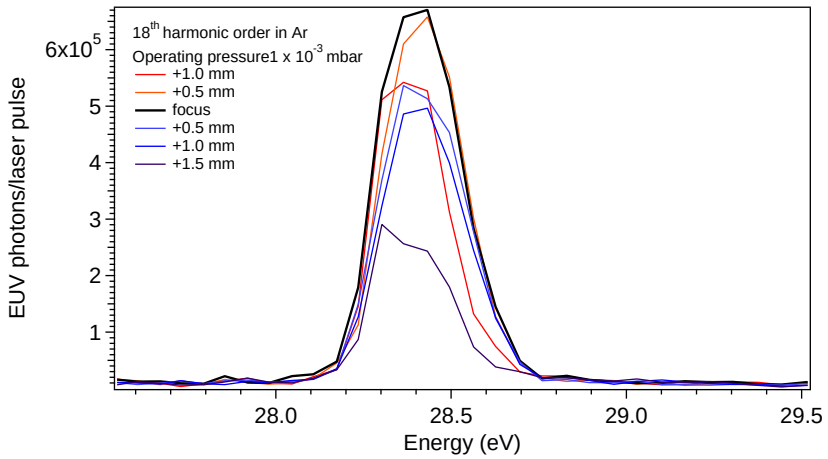

Figure 4.5: Spectral behavior of the 18^{th} harmonic generated in Ar at a pressure of 1×10^{-3} mbar.

erated by the near-IR beam in the tunneling regime ($\gamma_K \approx 0.25$).

The acquired profiles exhibit different spectral behaviors being, in first approximation, invariant to the sign of Δz. When the gas cell is placed at $\Delta z = \pm 1$ mm, the harmonics exhibit the same intensity and spectral behavior, both in neon and argon, i.e. at different values of the first ionization potential of the non-linear medium. At $\Delta z = \pm 1.5$ mm the intensity of the HH falls down. It is, approximately, halved in the 18^{th} harmonic generated in Ar, while in the neon spectrum it is abruptly reduced. These data proof, unambiguously, that when HH are generated into an hybrid dynamical condition ($\gamma_K \approx 1$), their spectral profiles do not exhibit any broadening at $z > z_0$ and any appreciable blue-shift. In addition the intensity quickly decreases when the gas cell is not centered in z_0.

4.3 Discussion

In order to understand the origin of these different spectral behavior a detailed analysis, concerning the phases of the generated EUV radiation and their dependence on the axial coordinate z, is necessary.

A gaussian beam, propagating into a free focused geometry, acquires a phase term traveling through the focal region (see chapter 2), which is known as Gouy phase $\Phi_{Gouy}(z)$ [1]. The total amount of this phase shift at the two far field extremities ($|z| \gg z_0$) is equal to π. Since the dipole phase depends on the axial coordinate z, the total axial phase $\Phi_{axl}(z) = \Phi_{Gouy}(z) + S_{st}(z)$ has to be analyzed [22].

4.3.1 The geometrical dispersion

As previously underlined, an optical beam, characterized by a gaussian intensity distribution, propagating into a free focused geometry suffers of a phase shift equal to $\Phi_{Gouy}(z)$. This phase term depends on the axial coordinate z as,

$$\Phi_{Gouy}(z) = \arctan\left(\frac{2z}{b}\right), \tag{4.1}$$

being $b = 2z_R$ the beam confocal parameter and z_R the corresponding Rayleigh length, i.e. equal to $\pi {w_0}^2/\lambda_0$. This means that the Gouy phase depends antisymmetrically on z.

The figure 4.6 reports the Gouy phases for the near-IR (red line) and visible (blue line) optical fields exhibiting, approximately, the same behavior. Being the Rayleigh length a function both of the beam waist, evaluated in the focus position z_0, and the driving wavelength λ_0 it is easy to estimate the corresponding value for a laser field ($\lambda_0 \approx 800$ nm), focused onto the non-linear medium by means of a lens with focal length of $f_{IR} = 250$ mm and a beam waist of $w_{IR} = 10$ mm and its SH ($\lambda_{SH} \approx 400$ nm), which is focused by a lens with focal length of $f_{SH} = 170$ mm and a waist equal to $w_{SH} = 5$ mm. The SH beam waist in the focus position is estimated to be $w_{SH} = 0.68 w_{IR}$, being w_{IR} the corresponding waist at z_0 for the near-IR beam. Since the SH wavelength is halved, its Rayleigh length is ≈ 1.36 times higher than the near-IR.

Nonetheless, the previous equation for the Gouy phase has to be modified in order to model the geometrical dispersion for the generated HH including the corresponding non-linear order q of the optical process, as,

$$\Phi_{Gouy}(z) = q \arctan\left(\frac{\lambda_0 z}{\pi {w_0}^2}\right). \tag{4.2}$$

The dark red line and the violet one refers to the Gouy phases for the 23^{rd} and 18^{th} harmonic order, respectively. From the previous equation it easy to note that these antisymmetric contribution to the global phase depends only on the non-linear order of the involved optical process.

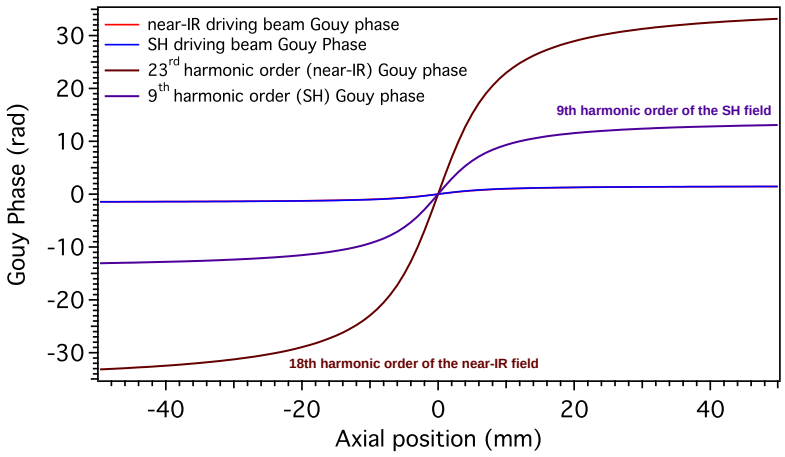

Figure 4.6: Contribution of the geometrical dispersion from the near-IR laser field (red line) and its SH (blue line). The dark red line refers to the Gouy phase of the 23^{rd} harmonic and the violet one refers to the 18^{th} harmonic, i.e. the 9^{th} harmonic order generated by the SH field.

4.3.2 The dipole phase

Since the intensity of the optical beam scales as $I(z) = I_0\Big[1 + (z/z_R)^2\Big]^{-1}$, the quiver potential $U_P(z)$ depends symmetrically on the axial coordinate z. The dipole phase $S(\mathbf{p}, t, \tau)$ can be evaluated by means of the saddle-points analysis (see chapter 2) as,

$$S_{sp}(t,\tau) = I_P\tau + \frac{1}{2}\int_{t-\tau}^{t} \mathrm{d}\tilde{\mathrm{t}}\Big(\mathbf{p}_{st} - \mathbf{A}(\tilde{t})\Big)^2, \tag{4.3}$$

which can be approximated by $S_{st}(t,\tau) \approx -U_P\tau$, i.e. as a product between the quiver potential and the return time [41, 42]. Introducing the previous dependence on z it becomes easy to evaluate its behavior.

Figures 4.7 and 4.8 refer to the dipole phases for 23^{rd} and 18^{th} harmonic orders, generated by the near-IR field ($\lambda_0 \approx 800$) and its SH ($\lambda_{SH} \approx 400$) nm, respectively. The red (figure 4.7) line and the blue (figure 4.8) refer to the dipole phases introduced by the short quantum paths, while the dark red and dark blue ones refer to the contributions of the long paths. This means that the coherent EUV/SXR radiation exhibits different peculiar characteristics if generated by the electrons recoiling with the parents ions along the short or the long paths, being different the values of their dipole phases.

On the other hand, the contribution of the long paths to dipole phases of the even HH (-2.39 rad) and the odd HH (-54.67 rad) differ substantially, being the first much lower. Once the dependence of $\Phi_{Gouy}(z)$ and

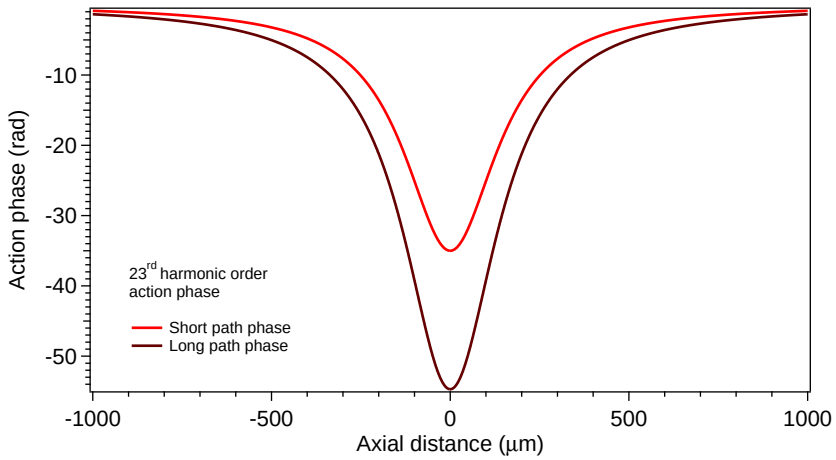

Figure 4.7: Dipole phase for HH generated by near-IR ($\lambda_0 \approx 800$ nm) laser pulses at $\gamma_K \approx 0.25$. The dark red line refers to the contribution of the long quantum path, while the red refers to the short one.

$S_{st}(z,t,\tau)$ on z are known, it is possible to compute the total axial phase $\Phi_{axl}(z)$, defined as the sum of these two terms. In order to optimize the coherence properties of the generated HH, the z values corresponding to a minimal variation of $\Phi_{axl}(z)$ over the non-linear medium have to be evalu-

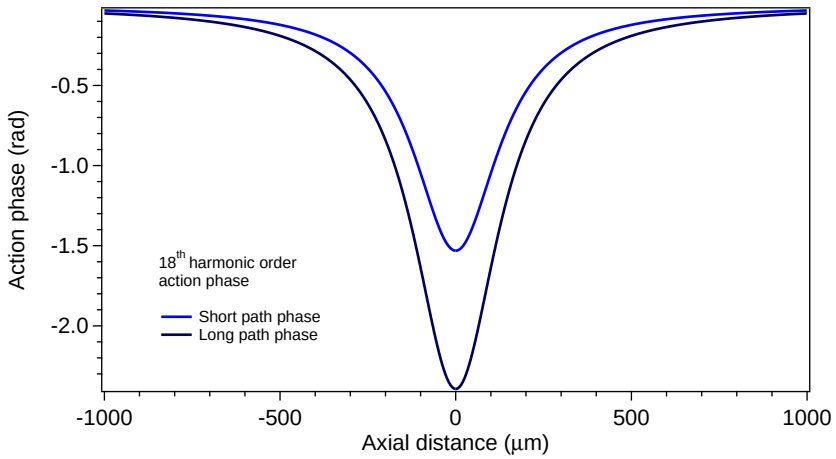

Figure 4.8: Dipole phase for HH generated by SH ($\lambda_{SH} \approx 400$ nm) laser pulses at $\gamma_K \approx 1$. The dark blue line refers to the contribution of the long quantum path, while the red refers to the short one.

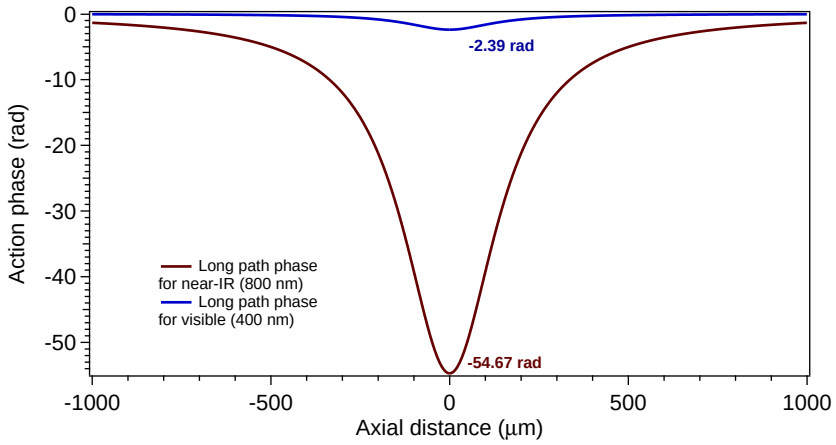

Figure 4.9: Comparison between the dipole phases for odd (red line) and even (blue line) HH. Each of them have been evaluated for the long path.

ated, i.e. looking for the not trivial solutions of $\partial_{z,z}\Phi_{axl}(z) = 0$ Figures 4.10 and 4.11 report the total axial phases $\Phi_{axl}(z)$ for the 23^{rd} and the 18^{th} (9^{th} harmonic order of the SH field), respectively. These two figures show both the contribution of the Gouy phase and the dipole one. In addition to the total axial phase $\Phi_{axl}(z)$ (black lines).

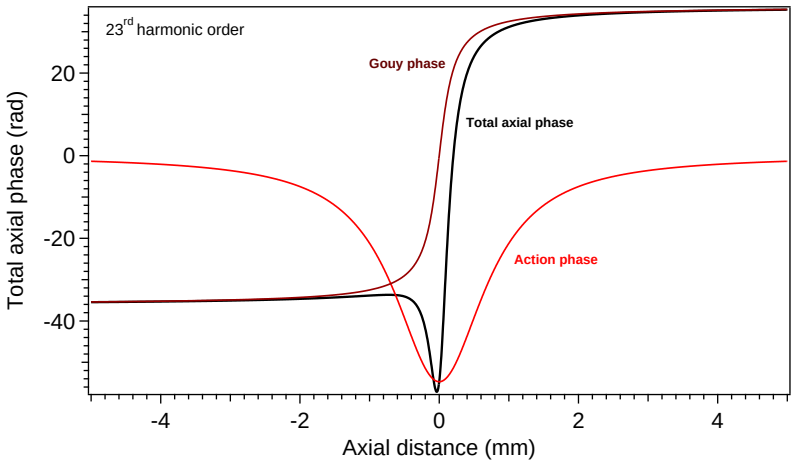

Figure 4.10: Total axial phase (black line) for the 23^{rd} HH. The red line refers to the dipole phase, while the dark red refers to the Gouy one.

Reminding the conclusions of chapter 2, the even HH have been generated into an hybrid dynamical regime being $\gamma_K \geq 1$, which has never been properly described. In a phenomenological framework it possible to model the atomic binding barrier as a static one (quasi-static approximation) at $\gamma_K \ll 1$, while it starts to oscillate quicker as the frequency of the optical field increases [1]. This condition is verified when the Keldysh's parameter is ≥ 1. In this hybrid regime the electron dynamics results over many optical cycles, rather than a single cycle process as modeled in the framework of the SFA.

When HH are generated in the hybrid regime (γ_K) in addition to a reduced diffusion process, the contribution of quantum paths with proper return times longer than one optical cycle, i.e. $\tau > T$, can not be excluded. It is rightful to call them very long quantum paths (τ_{vl}).

From these remarks, the contributions to the total axial phase $\Phi_{axl}(z)$ due to these very long quantum paths can be computed to find at which

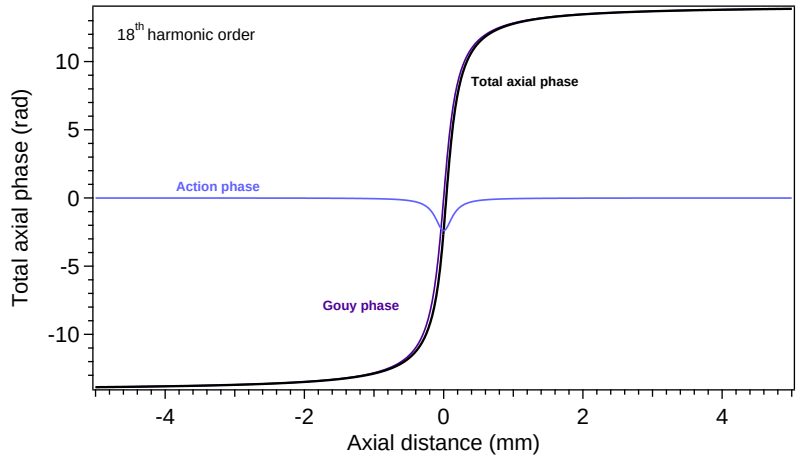

Figure 4.11: Total axial phase (black line) for the 18^{th} HH. The cyan line refers to the dipole phase, while the dark red refers to the Gouy one. It easy to note how the dipole phase represents only a small correction to $\Phi_{axl}(z)$.

value of τ_{vl} the dipole phase is not negligible (presence of a saddle-like). This is equivalent to set a superior limit for the quantum paths number, i.e. the number of possible re-coilings between the electron and the parent ion.

The total axial phases for the 18^{th} harmonic order, computed at different very long quantum paths, are reported in the figure 4.13. The ticker blue line refers to the values of $\Phi_{axl}(z)$ corresponding to the first non-trivial dipole phase, i.e. the term $S_{sp}(z,t,\tau)$ is not negligible (28 re-collisions). Figure 4.12 reports the total axial phase (times 0.5) for the 23^{th}, generated by the near-IR laser field in a tunneling dynamical regime. These axial phases can be compared to that calculated for $\gamma_K \ll 1$ (red curve), in order to compare the profile in both the non-perturbative ($\gamma_K \ll 1$) and the hybrid ($\gamma_K \geq 1$) dynamical regimes.

4.3.3 The induced temporal chirp

Being the optical field time dependent, i.e. $\mathbf{E}_L(t) = \mathbf{E}_0 \cos(\omega_0 t + \theta_L)$, the axial phase Φ_{axl} suffers of an instantaneous variation in time. This means that the temporal variation of $\Phi_{axl}(z,t)$ induces an instantaneous frequency variation, i.e. a temporal chirp equal to $\omega_{chirp}(z,t) = -\partial_t \Phi_{axl}(z,t)$.

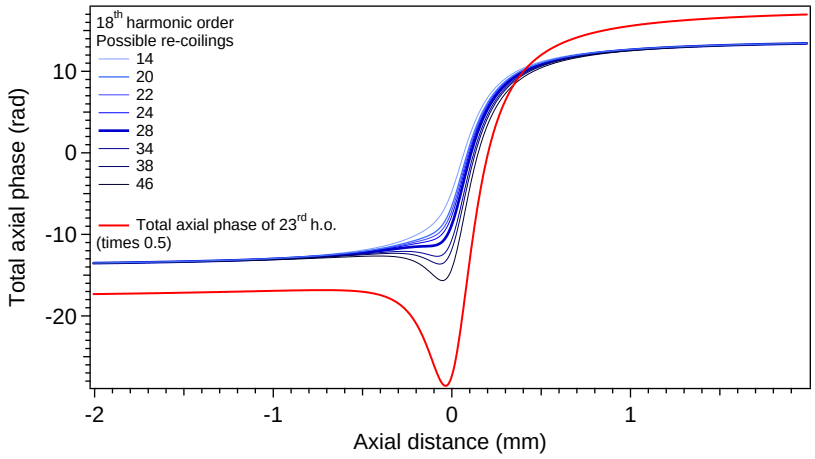

Figure 4.12: Different total axial phases for the 18^{th} harmonic order evaluated for different re-coiling times, i.e. for different very long quantum paths. The thicker blue line (28 re-coilings) refers to the first non trivial dipole contribution. The red line (times 0.5) refers to the total axial phase for 23^{rd} harmonic order.

Since the chirp depends both on the quiver potential U_P and on the return time τ, it generates broader spectral profile when the HH are generated by electrons re-coiling over long quantum paths. This means that the temporal chirp plays the role of a macroscopical marker for the detection of the involved quantum paths, i.e. if at $\Delta z > 0$ a broader spectrum is observed the dipole phase is dominated by the long paths contribution. On the other hand, a narrow profile at $\Delta z < 0$ means the the long paths are overwhelmed by the short ones.

This behavior is clear observed in the odd HH spectral profiles, while is lacking in the data referred to the even HH.

4.4 Conclusion

The experimental results concerning the coherence properties of the odd and even HH have been reported in this chapter. The spectral profile of the odd HH, generated by the near-IR laser field ($\lambda_0 \approx 800$ nm) in a well defined tunneling regime ($\gamma_K \approx 0.25$), are in agreement with the results presented in the current literature [22, 41]. The HH spectra exhibit a narrow profile when the non-linear medium is set before the focus position z_0 and a broader profile in the opposite position. These data can be model in terms both of the change of the axial phase matching condition and the induce temporal chirp.

Nonetheless, the even HH generated by means of the SH of the laser field, in an hybrid dynamical regime ($\gamma_K \geq 1$), do not appear as the previous ones (odd HH). The contribution of the dipole phases is lower, due to the lower quiver potential acquired by the involved electrons during the propagation step (2^{nd} step). Being the multi-photons conversion more efficient, as a consequence of the decreased diffusion mechanism, an additional remark is needed. Computing the contribution of the dipole phases in the framework of the SFA, i.e. taking into account only the first two quantum paths (short and long), the total axial phase remains, in first approximation, unchanged. This fact is able to explain the symmetrical fall down of the intensities (in terms of the generated EUV photons) of the even HH. In addition their spectral profile does not suffer a broadening process.

On the other hand, it is rightful to suppose that in a hybrid dynamical regime the electron dynamics has to be averaged over many optical cycles. Being the diffusion mechanism lower, the possibility that quantum paths, with proper return times longer than one optical cycle, contribute to the HH emission, has been taken into account, while a superior limit, in terms of the involved electron path, has been defined.

5

Damping of the non-perturbative process

5.1 Introduction

The calculation of the expectation value of the induced dipole moment $\langle \mathbf{d}(t) \rangle$ introduces a pre-exponential factor which depends on $\tau^{-3/2}$ (τ is the return time) [19]. This means that the amplitude of the induced dipole decreases abruptly at higher values of τ (see chapter 2). Such result emphasizes the quantum nature of the electron, since it model the increasing diffusion processes felt by the electron wavefunction, which reduces the overlap between the recoiling electron and its parent ion, i.e. it affects dramatically the recoiling amplitude (3^{rd} step).

As well the diffusion mechanism is expected, its contribution is usually overlooked in the current literature. Taking advantage on the halved optical period of the SH field ($\lambda_{SH} \approx 400$ nm), i.e. on a reduced diffusion, it is rightful to look for the minimal threshold needed to generate even HH, in order to compare these results with the generation of odd HH. This means that the efficiency (in terms of the generated EUV photons) has to be mapped as a function of γ_K, i.e. on the dynamical boundary conditions, in order to observe how the photons number and the coherence properties of the HH (spectral profile) scale depending on the Keldysh's parameter.

Reminding the results reported in the previous chapters, the generation of HH using the near-IR laser field ($\lambda_0 \approx 800$ nm) and its SH ($\lambda_{SH} \approx$

400 nm), takes place in different dynamical regimes as a tunneling (non-perturbative) and an hybrid one, respectively.

In the hybrid framework the non-linear ionization process do not take place into a tunneling through a static barrier (adiabatic approximation is valid only for $\gamma_K \ll 1$), since the binding potential starts to oscillate. At $\gamma_K \gg 1$ the ionization takes place via a multi-photons absorption (MPI). In this intermediate regime ($\gamma_K \geq 1$) the tunneling and the MPI mechanisms coexist, and this means that the electron wavefunction is delocalized into the continuum via a more complex process. In order to gain more informations on the possibility to generate HH beyond the usual tunneling (non-perturbative) regime, the Keldysh's parameters can be tuned exploring the prospective hybrid regime.

The aim of this chapter is to report the first investigation of such hybrid regime by varying the pulse energy of the SH field, while preserving its temporal structure, in order to tune the corresponding γ_K. The experimental data provide an unambiguous evidence of the hybrid regime [45]. The minimal threshold needed to generate HH by near-IR or pure visible pulses are reported, in addition with the qualitative results computed by means of the phenomenological model presented in the chapter 3.

5.2 Control and manipulation of the dynamical regime

5.2.1 The experimental set-up

The experimental set-up is similar to the one exhaustively presented into the chapter 3 in order to spectrally characterize the response on several inert gases. The ≈ 50 fs, 2.5 mJ near-IR ($\lambda_0 \approx 800$ nm) s-polarized beam passes through a telescope in order to reduce its waist, w, down to ≈ 5 mm.

The laser beam is split into two orthogonally polarized beams, by the CVA. The CVA varies the pulse energy of the outgoing beams, while preserving the pulse temporal structure, i.e. modifying γ_K continuously, therefore controlling the ionization dynamics.

The p-polarized beam is frequency doubled by a Beta Barium Borate,

type-I, (BBO) non-linear crystal (thickness 0.35 mm), with a conversion efficiency up to $\approx$ 35 %, while the s-polarized SH beam is then separated from the residual near-IR beam by three dichroic high reflectivity band-pass mirrors set at $\lambda_{SH} \approx 400$ nm.

The SH pulses are than focused, by a 170 mm plane-convex lens, into the gas cell filled up to 10^{-3} mbar with xenon. The s-polarized near-IR beam outgoing form the CVA is stopped, by means of a beam stopper.

Once generated, the HH train are spectrally dispersed by means of the monochromator, which consists of the Au-coated spherical grating and the fixed exit slit (see chapter 3), and subsequently analyzed by the channel electron multiplier. The following figure 5.1 reports a sketch about the optical set-up used for such experiments, being quite different from the one previously presented. In this experimental conditions even HH have been generated by a pure SH field focused onto a xenon target, varying the incoming pulse energy, i.e. the corresponding Keldysh's potential, keeping fixed the gas pressure.

5.2.2 Experimental results

Once the absolute responses of each single optical device (the Al-filter, the monochromator and the CEM) are known it is possible to estimate the number of the generated coherent EUV/SXR photons. The corresponding values of γ_K have been evaluated numerically setting the temporal length of the SH pulses equal to 60 fs and the spot size in the focus 40 μm. The wavelength and the repetition rate of the optical source are $\lambda_{SH} = 400$ nm and 1 kHz, respectively, while the first ionization potential of the non-linear medium (xenon) is 12.13 eV.

In order to generate HH in different dynamical conditions, the intensity of the p-polarized near-IR beam has been continuously varied preserving its temporal structure by means of the CVA. The BBO has been set in the phase-macthing condition to maximize the SH generation (conversion efficiency up to $\approx 35\%$). Even HH have been generated in Xe keeping fixed the operating gas pressure at 5×10^{-3} mbar. The figure 5.2 reports the number of the generated EUV photons of the 10^{th} (79.8 nm i.e. $\approx$ 15.5 eV)

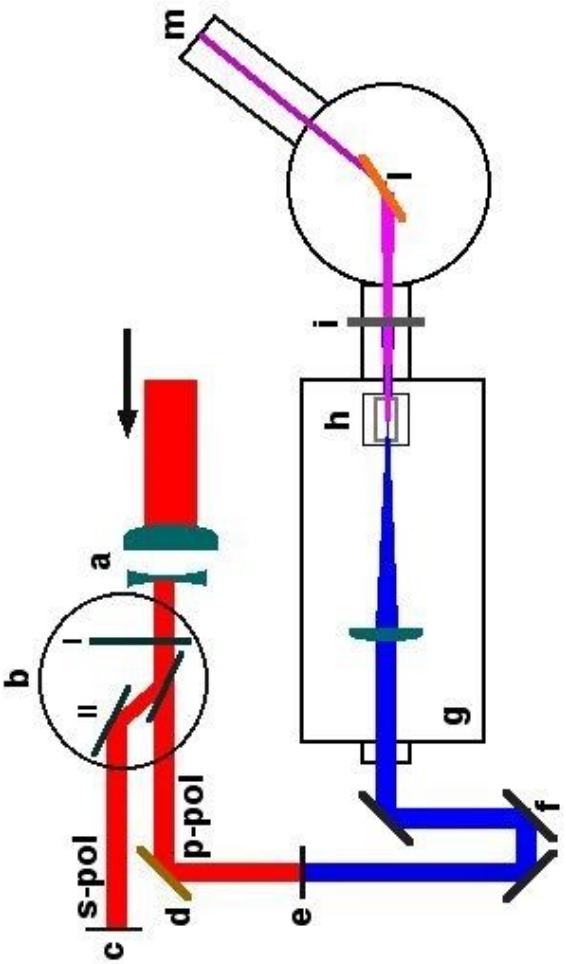

Figure 5.1: Layout of the optical set-up used to study the hybrid dynamical regime. The sketch reports a (a) telescope, (b) CVA: (I) $\lambda/2$ and (II) Brewster mirrors, (d) Au mirror, (e) BBO noon-linear crystal, (f) visible mirrors, (g) generation chamber, (h) cell, (i) Al filter, (l) grating and (m) detector and (c) beam stopper used to block the s-polarized beam.

harmonic order as a function of the corresponding values of γ_K. From these experimental data it easy to recognize three different dynamical regimes. A first one, corresponding to the non-perturbative regime at $\gamma_K < 1$ (red dots), can be well described in the framework of the ADK model. Here the electron wavefunction is delocalized into the continuum via a tunneling process through a quasi-static barrier. The second regime is characterized by an exponential decay in the range between $1 < \gamma_K < 3$ (violet dots). At γ_K the signal scales linearly when the Keldysh's parameter increases. Here the non-linear ionization process is well described in terms of a multi-photons absorption, i.e. multi-photons ionization or MPI.

A quite phenomenological picture of such non-linear processes can be gained by considering that the re-covering process (3^{rd} step) of the delocalized electron wavefunction with its parent ion one, depends strictly on the phase θ_L at which the electron has been released into the continuum (see chapter 2). Yudin and M. Ivanov have proposed an analytical model (Y-I model) in order to explain in details such non-linear ionization processes in the hybrid, or intermediate, regime [36].

The Y-I model predicts that in the MPI regime the role of θ_L into the ionization rate equation $\Gamma_{YI}(t)$ becomes negligible. This implies a drop of the efficiency (in term of the generated photons) of the HHG process for $\gamma_K \ll 1$. This effect is clearly observed into these experimental results. The experimental results have been fitted using an exponential function as,

$$n(\gamma_K) = n_0 + A\Big(-\frac{\gamma_K}{\tau}\Big), \tag{5.1}$$

where n_0 is the background, A is the amplitude (both expressed in terms of EUV photons/laser pulse) and τ is the decay constant. The fitting parameters are reported in the table 5.1.

In a phenomenological picture these data report the clear evidence of an exponential decay of the HH efficiency (in terms of the generated EUV photons), i.e. the exponential decrease of the contribution of the tunneling mechanism to the whole ionization mechanism.

n_0 (photons/laser pulse)	$2.11 \times 10^4 \pm 8.01 \times 10^2$
A (photons/laser pulse)	$2.89 \times 10^8 \pm 9.04 \times 10^4$
τ^{-1}	3.13 ± 0.02

Table 5.1: Fit parameters of the exponential damping.

5.2.3 Simulation of the damping of the tunneling mechanism

To gain a more quantitative description of the hybrid dynamical regime a phenomenological model becomes mandatory. A possible choice is to start from the semi-classical three steps model, focusing the attention onto the non-linear ionization process (1^{st} step), which is well described by the ADK model [1, 15]. To model the observed damping in the experimental data it is necessary to extend the rate equation, $\Gamma_{ADK}(t)$, to arbitrary γ_K, as presented in the chapter 3.

As underlined in the previous paragraph, for $\gamma_K \geq 1$, i.e. the intermediate or hybrid regime, Yudin and Ivanov have developed an *ad-hoc* model, that demonstrates the strict dependence of the ionization mechanism on the phase θ_L and underlines the possibility that a competing process between tunneling and MPI mechanism takes place.

Unfortunately, the rate equations of the Y-I model are not of easy solution, so defining $\Gamma(t)$ can be defined (with exponential accuracy) as,

$$\Gamma(t) \propto exp\left[-\frac{2I_P}{\omega_0} f(\gamma_K)\right], \tag{5.2}$$

being the function $f(\gamma_K)$ dependent of γ_K as,

$$f(\gamma_K) = arccosh\left[\sqrt{1+\gamma_K^2}\left(1+\frac{1}{2\gamma_K}\right) - 2\sqrt{1+\frac{1}{\gamma_K}}\right]. \tag{5.3}$$

Therefore, it is possible to compute the behaviour of the function, η_{eff}, defined as suggested by A. Gordon and F. Kaertner, and related to the HHG efficiency [38]:

$$\eta_{eff} = {\omega_0}^3 |w(t_s)w(t_l)|^2. \tag{5.4}$$

These $w(t_s)$ and $w(t_l)$ correspond to the free electron density, for short and long quantum paths, respectively. η_{eff} is defined as the interference term between these contributions, while ${\omega_0}^3$ accounts for the electronic wave-function diffusion process (it scales as T^3). $w(t_{s,l})$ are defined via the usual equation (see chapters 2 and 3), dependent on $\Gamma(t)$,

$$w_{ion}(t) \approx 1 - \exp\left[-\int_{t_i}^{t_f} \Gamma(\tau) d\tau\right]. \tag{5.5}$$

This function refers to a kind of dimensionless efficiency of the HHG processes, which proofs qualitatively the response of a single atomic system when interacting with an optical field at arbitrary values of γ_K. As a consequence of this phenomenological equation it is rightful to evaluate the dependence of η_{eff} for several optical fields, as a near-IR one ($\lambda_0 = 800$ nm), a visible field, i.e. its SH, ($\lambda_{SH} = 400$ nm) and the ultra-violet one with wavelength corresponding to the TH (third harmonic), i.e. $\lambda_{TH} = 266$ nm. These data have been acquired starting in a tunneling regime for each optical field, lowering progressively the corresponding Keldysh's parameters decreasing the pulse energy and preserving the temporal structure, as done by the CVA device.

The calculated η_{eff} values versus γ_K, for three different driving fields at $\lambda = 800$ (red line), $\lambda = 400$ (blue line) and $\lambda = 266$ (violet line) nm, are shown in fig. *next*.

For decreasing driving wavelengths λ_0, the hybrid regime moves toward higher γ_K. The red arrow refer to the measured threshold to generate HH by means of such near-IR pulses and corresponds to a pulse energy of ≈ 150 μJ, i.e. at $\gamma_K \approx 0.8$. By comparing the experimental data with our model a clear and general agreement concerning the behavior of the transition between the tunneling and the MPI regime is obtained. In particular, the exponential decay of the HHG intensity, observed in our experiment for $0.5 < \gamma_K < 3$, is properly described by our model. This result helps also to give a more direct physical interpretation of the parameter γ_K, which for the hybrid regime can be interpreted as the contribution of the tunneling mechanism to the whole HHG process, or as a parameter related to the damping of the tunnelling regime, while τ contains all the information concerning the

threshold condition for generation of high-order harmonics.

5.3 Conclusions

The possibility for generating HH using optical fields with different wavelengths has been presented both in an experimental framework and a phenomenological one. Taking advantage on the different diffusion processes it has been possible to generate coherent EUV photons by a pure SH ($\lambda_{SH} \approx$ 400 nm) tuning the energy of such pulses, while preserving their temporal structure. This means that it has been possible to control the dynamical process that delocalizes the electron wavefunction into the continuum, giving the possibility to study the generation of HH into an hybrid regime.

For the first time, to the author's knowledge, the progressive damping of the tunneling (non-perturbative) contribution to the whole non-linear process has been reported. In order to gain more quantitative informations a suitable phenomenological model has been developed in order to reproduce the experimental data.

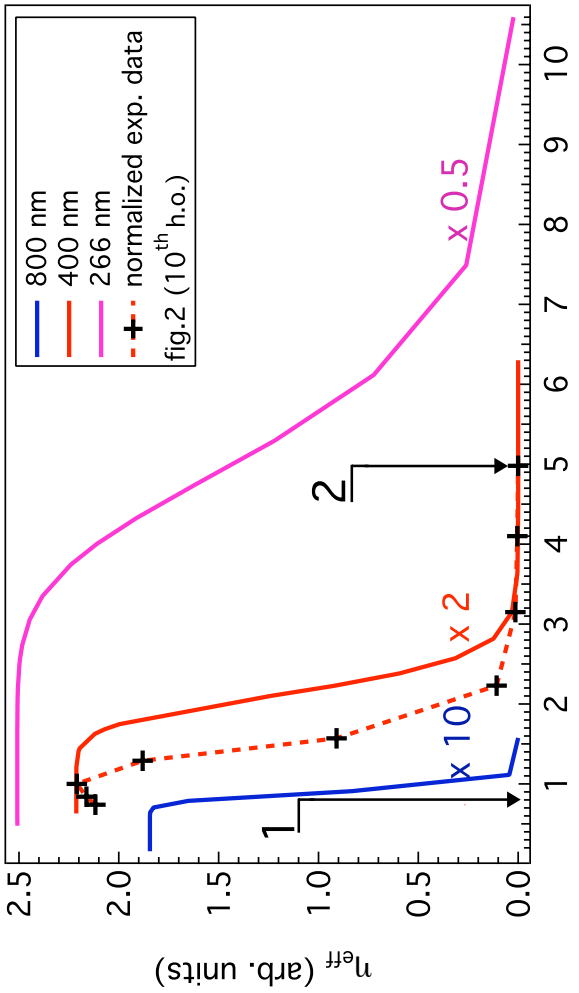

Figure 5.3: Calculated η_{eff} vs γ_K at $\lambda_0 = 800$ nm (blue), $\lambda_0 = 400$ nm (red) and $\lambda_0 = 266$ nm (purple). The black crosses represent the normalized experimental data. The red dashed line is a guide for the eye. Arrow 1 and 2 represent the experimental threshold for HHG processes at $\lambda_0 = 800$ nm and $\lambda_0 = 400$ nm.

6 Time-resolved EUV/MCD experiments

6.1 Introduction

The generation of coherent EUV/SXR photons via HHG processes has been investigated in the last years using near-IR, or mid-IR, laser pulses and leading to the emission, under certain experimental conditions, of pulses with a temporal structure in the attosecond time scale [2, 3]. Nonetheless, a diffuse application of HH pulses for performing TR experiments in condensed matter research manipulating the state of polarization of such EUV/SXR pulses is still lacking [25, 26].

This chapter reports the first application of HH pulses for studying the magnetization dynamics of ferromagnetic 3d metals on a femtosecond time scale by time resolved x-ray circular magnetic dichroism. An *ad-hoc* experimental set-up has been designed and built to probe the magnetization dynamics of an alloy composed of Fe and Ni (permalloy or $Fe_{20}Ni_{80}$) by means of circularly polarized HH pulses, i.e. looking for the different absorption of left or right circularly polarized EUV pulses. This physical phenomenon is known as magnetic circular dichroism (MCD). If such anisotropy in the absorption of left or circularly polarized light is probed by SXR pulses, i.e. the XMCD process [46, 47]. This challenging experiment has been developed as the result of an international collaboration between the T-ReX Laboratory and the Center for X-Ray Optics (CXRO) of the Lawrence Berkeley National Laboratory (LBNL), located in Berkeley (USA). The existing lit-

erature accounts for several experiments proofing the impossibility to generate efficiently elliptical (or circularly) polarized HH in inert gases [48]. The CXRO has developed a novel multi-layer optical device acting like a quarter wave-plate (ML-QWP), but designed for EUV radiation [49].

6.2 Ultra-fast demagnetization processes

The increasing development of laser sources generating ultra-fast coherent pulses has bring to light the possibility to investigate, exhaustively, the de-magnetization processes of ferromagnetic 3d metals (Fe, Co and Ni) on the sub-picosecond (sub-ps) time scale [50, 51]. This fact is quite surprising, since the dynamics of the de-magnetization of a ferromagnetic system has been expected to take a proper relaxation time of $\approx$ 100 ps, i.e. in the sub-ns time scale. The first experimental evidence of such processes has been reported in 1996 by E. Beaurepaire and coauthors [50]. The de-magnetization process of a Ni thin film (22 nm thickness) has been probed using p-polarized, $\approx$ 60 fs, visible ($\lambda_0 \approx 620$ nm) pulses in a time-resolved magneto-optical Kerr effect (TR-MOKE) configuration, i.e. looking for any variation in the state of polarization of the reflected radiation. The Ni thin film has been placed in the gap of a longitudinal electromagnet, in order to vary the intensity and the direction of the applied external magnetic field, $\mathbf{B}_{ext}$. A second p-polarized pulse, delayed in time, has been used to heat the sample, i.e. to de-magnetize it. The corresponding relaxation time has been estimated to be $\approx$ 200 fs by varying the relative delay between the pump and probe pulses. This pioneering work has given prominence to an increasing interest on such processes, both using ultra-short laser pulses and EUV/SXR radiation, generated via Free Electron Laser (FEL) or femto-slicing facilities, as recently done by the group directed by Prof. H. Durr [52]. They have investigated the ultra-fast de-magnetization process at the absorption L Ni-edge by means of a time resolved x-rays magnetic dichroism (TR-XMCD) experimental configuration. The near-IR laser pulses have been used to heat, i.e. to de-magnetize, the sample and the circularly polarized ultra-short SXR radiation, in the photon energy range between 845 eV and 885 eV, to probe the magnetization state of the sample. This exper-

iment has been performed at the femto-slicing source located at the Bessy II Light Source in Berlin (Germany).

Nonetheless, the intrinsic mechanism responsible for such ultra-fast processes remains still unknown, even if it can be qualitatively explained by means of a three steps phenomenological approach, involving the dynamics of the free electrons set in the conduction band, the lattice and the spins.

6.3 Experimental set-up

The challenging idea is to probe the magnetization state of permalloy by means of the coherent radiation generated, in the EUV spectral region, via HHG process, at the absorption $M_{2,3}$ Fe/Ni-edges. These Fe/Ni-edges pile up at energies of ≈ 54 eV and ≈ 66 eV, i.e. to the photon energies of the 35^{th} and 43^{rd} harmonic orders of a near-IR ($\lambda_0 \approx 800$ nm) optical field, respectively. The circularly polarized EUV light has been focused onto the sample, being set in the gap of a longitudinal electromagnet, in order to change both the direction and the intensity of $\mathbf{B}_{ext}$.

Because of the anisotropy for absorbing left or right circularly polarized radiation at the $M_{2,3}$ Fe/Ni-edges, the reflected beams suffer of a similar behavior, i.e. their intensities, $I_{\pm}$, differ for a relative amount of, maximally, 10%. The same measurement can be performed varying the direction of $\mathbf{B}_{ext}$ and keeping fixed the state of polarization of the incoming EUV pulses, i.e. looking for a time-resolved magnetic circular dichroism by means of EUV radiation (TR-EUV/MCD).

The HH train, generated in inert gas, goes through a ML-QWP, which is mounted on an holder set at the Brewster angle. It is optimized to transmit only the spectral components, of the generated HH, with photon energies higher than ≈ 50 eV or ≈ 60 eV. The transmitted radiation appears circularly polarized.

The radiation outgoing from the ML-QWP is band-pass filtered by a proper multi-layer spherical mirror, designed for the energies of the Fe-edge or the Ni-edge, respectively. The multi-layer spherical mirror focuses the EUV radiation on the sample.

Because of its higher divergence, part of the residual near-IR beam

can pass beyond the ML-QWP. An Au-coated spherical mirror (doughnut shaped) is used to focus the laser beam on the sample in order to demagnetize the sample by thermal process. The optical device, composed by the inner multi-layer mirror and the outer Au-coated one, constitute the pump and probe mirror (PPM). The outer Au-mirror is mounted onto a stage, which can be moved, varying the relative temporal delay between the near-IR (the pump) and the EUV (the probe) radiation.

These optical devices are operating in a high vacuum condition, i.e. $\approx 10^{-6}$ mbar, in order to propagate the EUV radiation. A sketch of the experimental set-up is reported in the figure 6.1.

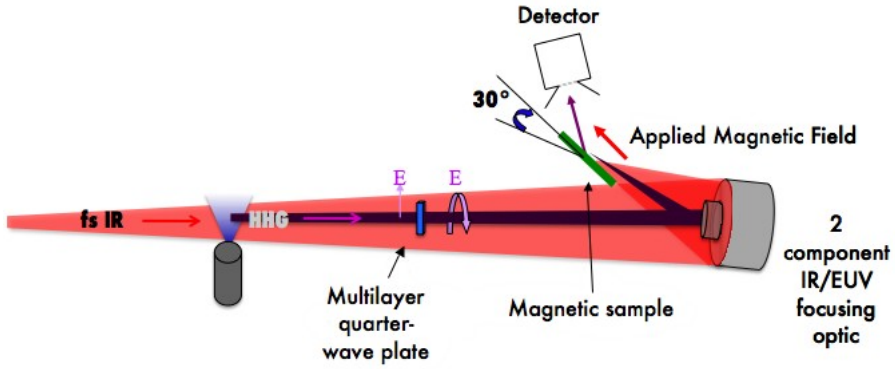

Figure 6.1: Sketch of the experimental set-up designed for TR-EUV/MCD using circularly polarized HH at the $M_{2,3}$ Fe/Ni-edges of ferromagnetic 3d metals. The train of generated HH encounters the ML-QWP, while the residual optical field passes beyond it. The PPM mirror (2 component) is able to focus the pump and the probe pulses onto the sample. The MCD signal is extracted detecting the EUV reflected beam. Courtesy of Andy Aquila.

6.3.1 Development and test of the multi-layer quarter wave-plate device designed for EUV radiation

The efficiency of the HHG processes (in terms of the number of generated photons) suffers of a dramatical fall down if the ellipticity of the incoming laser field increases [48]. This fact can be summarized in a phenomenological approach by considering that an elliptical (or circular) optical field is able to promote an atomic electron into the continuum. On the other hand, a transverse component in the momentum ($p_\perp$) is introduced with a consequence lowering of the probability of re-colliding with its parent ion. Several groups have investigated the dependence of the efficiency on the ellipticity of the incoming optical beam, emphasizing this problematic feature of the HHG processes.

In order to overcome such limitation and to perform MCD experiments by means of circularly polarized EUV pulses, a novel multi-layer optical device have been developed in collaboration with the Center for X-Ray Optics (CXRO) of the Lawrence Berkeley National Laboratory (LBNL). As previously underlined, such optical device has been designed to act both as a quarter wave-plate (ML-QWP) and a band-pass filter for transmitting only the spectral components with photon energies approaching the $M_{2,3}$ Fe/Ni-edges.

The ML-QWP designed to probe the MCD signal at the $M_{2,3}$ Fe-edge has been tested at the Advanced Light Source (ALS), located in Berkeley (USA), at the beam-line 6.3.2 (EUV and SXR Reflectometry and Scattering) [53]. Two kind of measurements have been performed.

The ML-QWP has been installed onto its holder set at the Brewster angle, while the permalloy sample has been set in the presence of a longitudinal (static) magnetic field, $\mathbf{B}_{ext}$, generated by permanent magnets. The EUV radiation from the beam-line has been transmitted and circularly polarized by the ML-QWP with a transmission efficiency of $\approx 1.7\%$ and, successfully, sent onto the sample detecting the intensity of the reflected radiation by means of a photodiode. The data have been acquired varying both the incidence angle on the sample between 20 degrees and 40 degrees, and the photon energy between 50 eV and 56 eV. This test has been performed per

each direction of the static magnetic field, in order to acquire two arrays of data (normalized to the ALS signal), i.e. $I_{\pm}$. The resulting MCD signal, I_{MCD}, comes from,

$$I_{MCD} = 2\frac{I_+ - I_-}{I_+ + I_-}. \tag{6.1}$$

These data have been used to reconstruct an iso-dichroic map at the $M_{2,3}$ Fe-edge. The results are reported in figure 6.2.

Once the possibility for polarizing EUV pulses, by means of the ML-QWP, has been proofed, the static magnets have been replaced with an electromagnet varying both the intensity and the direction of $\mathbf{B}_{ext}$. The resulting hysteresis loop is reported in the figure 6.3 (green dots and line). The figure 6.4 reports the zoom onto the coercitivity value probed to be ≈ 1.7 Oe, in perfect agreement with the existing literature.

These experimental results demonstrate the first applications of such optical devices for modifying the degree of polarization of the incoming radiation. More detailed informations about their working principles are reported in Dr. Andrew Lee Aquila's Ph.D. thesis [49].

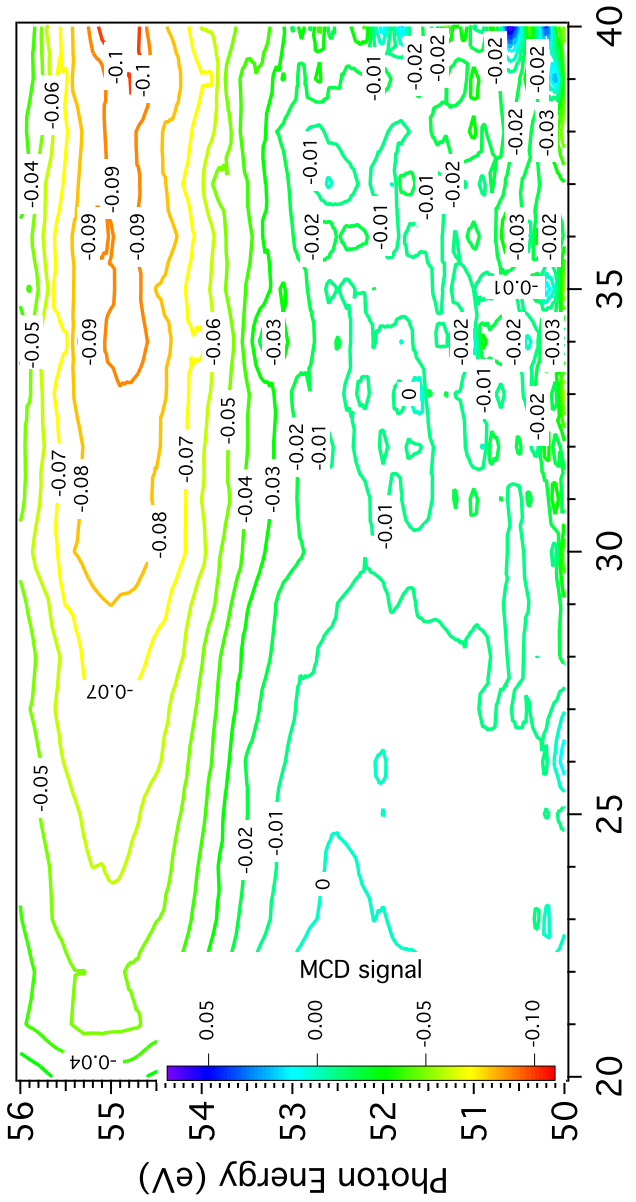

Figure 6.2: Iso-dichroic map of the MCD signal as a function of the photon energy of the incoming radiation and the angle of incidence on the sample. This test has been performed at the 6.3.2 beam-line at the ALS.

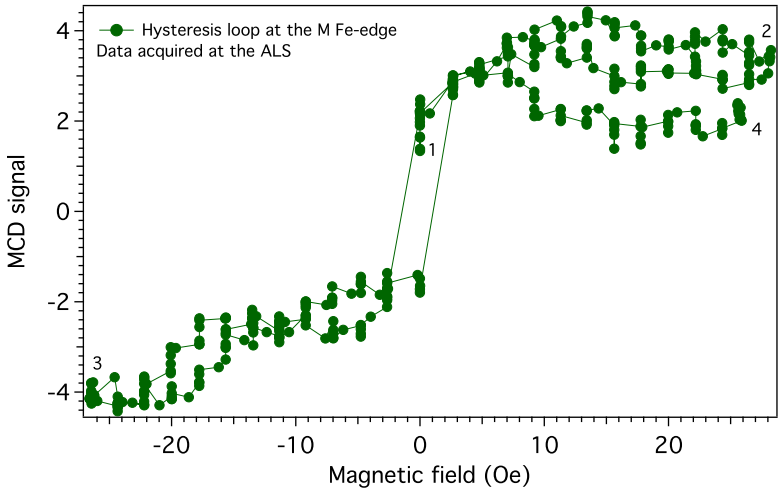

Figure 6.3: Hysteresis loop performed at the $M_{2,3}$ Fe-edge, zoomed onto the coercitivity value. The loop starts at 1, reach the positive and negative maxima at 2 and 3, respectively, and finally turn back to the positive maximum at 4. This test has been performed at the 6.3.2 beam-line at the ALS.

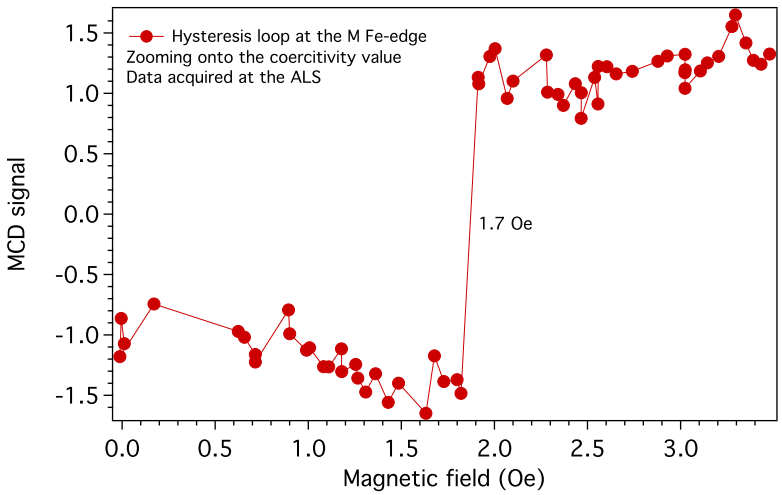

Figure 6.4: Hysteresis loop performed at the $M_{2,3}$ Fe-edge. This test has been performed at the 6.3.2 beam-line at the ALS.

6.3.2 The high-order harmonics generation vacuum chamber

Being the optical devices able to transmit only the spectral components of the HH train with photon energies corresponding to the $M_{2,3}$ Fe/Ni-edges, the monochromator (see chapter 3), consisting of the spherical grating and an the exit slit, becomes superfluous. As a consequence of this fact a new HHG source has been developed *ex-novo* at the T-ReX Laboratory and it consists only of a vacuum chamber for generating the coherent radiation (GC).

The $\approx$ 50 fs, $\approx$ 2.5 mJ, near-IR ($\lambda_0 \approx$ 800 nm) beam has been focused, by means of a plane-convex lens with a focal length equal to 300 mm, onto a gas cell centered in the GC and filled with argon. The gas pressure and the PM conditions have been optimized in order to maximize the number of the generated EUV/SXR photons. HH have been generated by such laser pulses, since the 35^{th} harmonic order has a photon energy centered at 54.38 eV, i.e. it represents an ideal tool to probe the absorption $M_{2,3}$ Fe-edge. On the other hand, the 43^{rd} harmonic order has a photon energy of 66.82 eV, i.e. it is able to probe the Ni-edge.

Figures 6.5 and 6.6 refer to two pictures taken during the data acquisition, showing the focused near-IR beam while entering in the GC and traveling through the gas cell (figure 6.7), i.e. generating the EUV/SXR radiation.

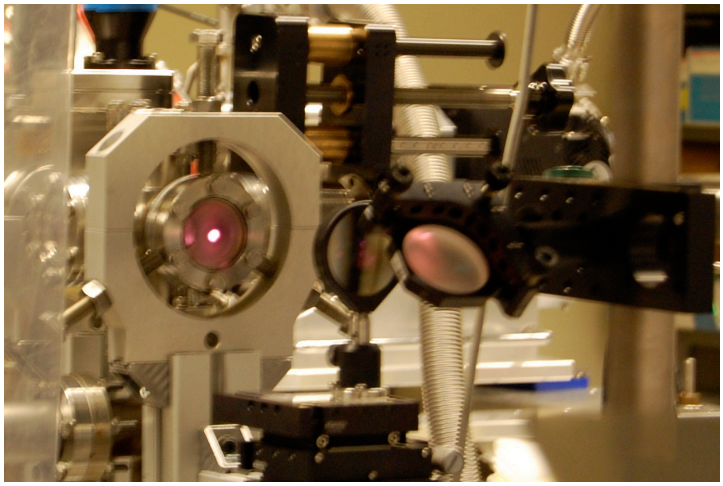

Figure 6.5: The near-IR ($\lambda_0 \approx 800$ nm) beam is focused by a plane-convex lens in the vacuum generation chamber.

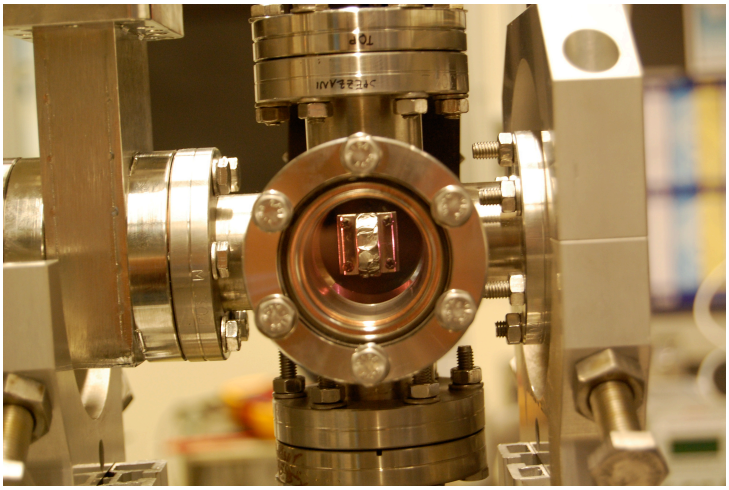

Figure 6.6: The focused near-IR beam passes through the gas cell filled with Ar generating the coherent EUV/SXR radiation.

6.3.3 The reflectometer experimental chamber

The generation chamber has been connected to an high-vacuum experimental chamber, called IRMA (Instrument pour la Réflectivité MAgnétique). Preserving the high-vacuum conditions, it is possible to control the incidence angle of the light onto the sample, which is mounted onto a holder equipped with a longitudinal or transversal electro-magnet for modifying the direction and the intensity of $\mathbf{B}_{ext}$.

The detectors are mounted onto a rotating harm in order to optimize the detection of the reflected radiation.

A more detailed technical overview on the experimental chamber IRMA is presented in the references [54, 55].

The GC and IRMA are separate by a differential pumping stage. Once generated, the HH spectral components encounters a (removable) 200 nm thickness Al-filter (on a mesh), which absorb the residual optical beam. The inner spherical mirror focuses the monochromatized EUV beam onto the permalloy sample. The incidence angle on the sample has been usually set between 30 degrees and 40 degrees, where both the existing literature and the data acquired at the ALS have probed the best MCD signal. The pressure in the GC is $\approx 1 \times 10^{-2}$ mbar, but inside IRMA remains lower than 5×10^{-6} mbar, to avoid any discharge process on the CEM. The table 6.1 reports all the experimental parameters for the TR-EUV/MCD experimental set-up:

GC operating pressure (Ar)	$\approx 1 \times 10^{-2}$ mbar
IRMA operating pressure (vacuum)	$\leq 5 \times 10^{-6}$ mbar
Al-filter (on a mesh) tickness	200 nm
Photons per pulse (source)	$\approx 10^7$
Photons per pulse (detector)	$\approx 10^2$
ML-QWP transmission at $M_{2,3}$ Fe-edge (54.6 eV)	0.017
ML-QWP transmission at $M_{2,3}$ Ni-edge (66.1 eV)	0.029
PPM reflectivity at $M_{2,3}$ Fe-edge (54.6 eV)	0.34
PPM reflectivity at $M_{2,3}$ Ni-edge (66.1 eV)	0.26
Sample reflectivity	$\leq 5\%$
PPM focal length	150 mm
PPM subtended angle	10 degrees
Incidence angle on the sample	30-40 degrees
Sample thickness ($Fe_{20}Ni_{80}$)	30 nm

Table 6.1: Main parameters of the TR-EUV/MCD experimental set-up

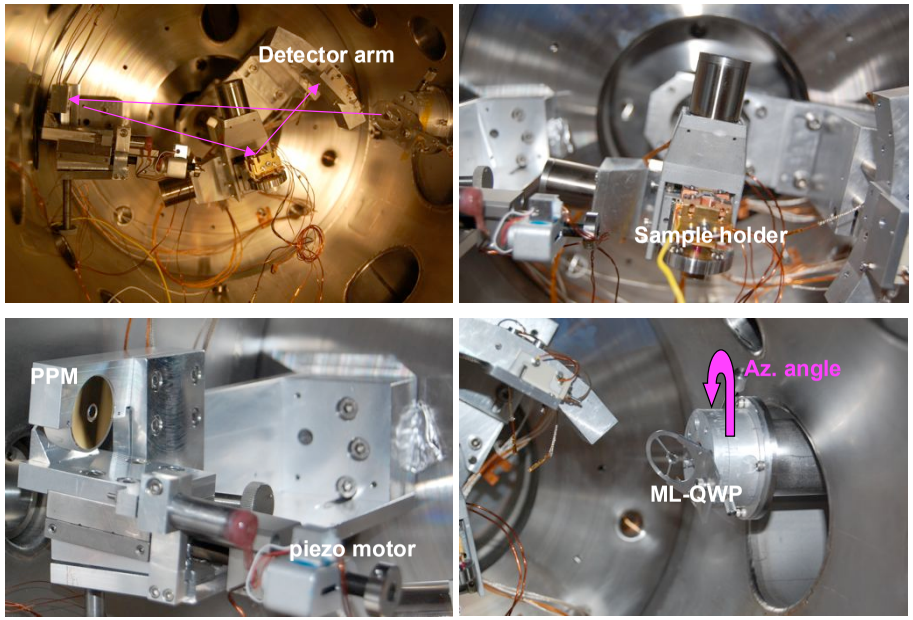

Figure 6.7: Images from the TR-EUV/MCD set-up. A refers the path (violet arrows) of the EUV radiation inside the experimental chamber, B refers to the sample holdes, C shows the PPM spherical mirror and D refers to the ML-QWP and its holder (azimuthal angle can be easily optimized).

6.4 Experimental results

Several test have been performed, in order to detect the MCD signal at the $M_{2,3}$ Fe/Ni-edges, respectively. In this chapter some preliminary results are presented. The following experimental results have been acquired in a static (not TR) configuration, i.e. without the presence of the residual near-IR optical beam. Both the ML-QWP designed for Fe/Ni-edges have been tested looking for the best experimental configuration. The detection of such MCD signal was very difficult, because of the low (≈ 100) number of photons per pulse reaching the detector. The signal has been normalized using the photo-induced current from the ML-QWP.

6.4.1 Static data on $M_{2,3}$ Fe-edge

This paragraph reports the static data (not TR) on the hysteresis loop acquired at the $M_{2,3}$ Fe-edge, varying the intensity of the longitudinal magnetic field, i.e. varying the current in the electro-magnet in the range between 0.5 A and -0.5 A. These data represent the state of the art about of the applications of coherent HH pulses in order to probe the magnetization dynamics of such ferromagnetic systems via EUV/MCD experiments.

The data have been acquired by means of a photo-diode and normalized to the photo-induced current in the ML-QWP. The incidence angle was set at 40 degrees. The red dots refer to the experimental data, while for sake of clarity also the smoothed data (blue dots) are reported. These refer to the corresponding smoothed hysteresis loop. These preliminary results exhibit a contrast at the two sides of the loop. The corresponding MCD signal is ≈ 0.013. It has been evaluated averaging the all data at the two extremities of the hysteresis loop.

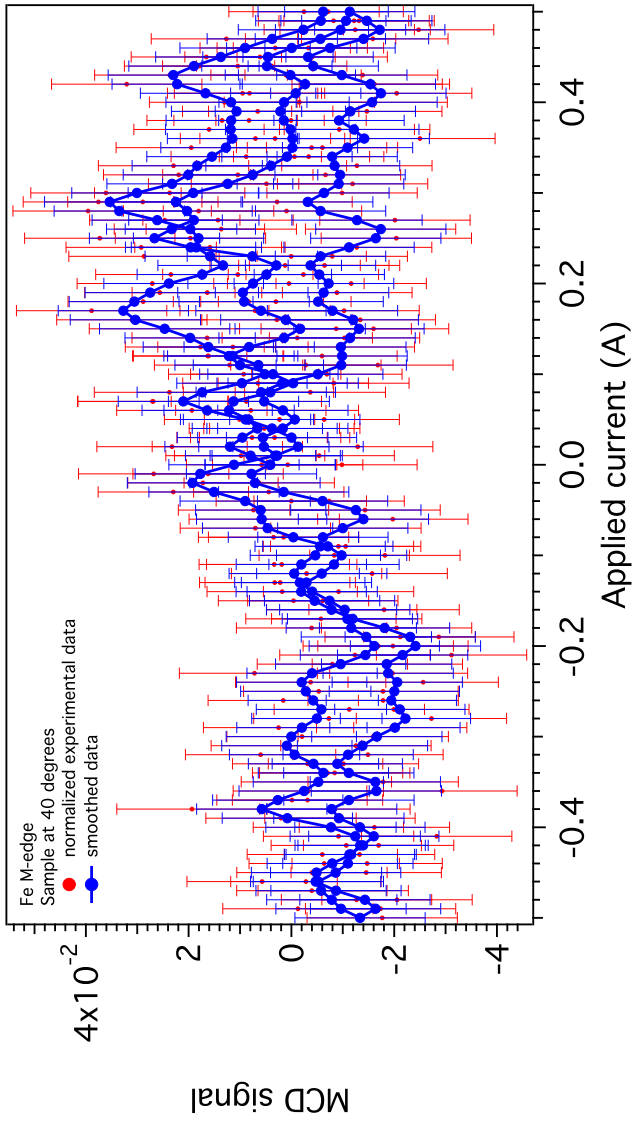

Figure 6.8: MCD hysteresis loop at the $M_{2,3}$ Fe-edge. The data have been acquired by means of a photo-diode and normalized to the photo-induced current in the ML-QWP. The sample has been set at an incidence angle of 40 degrees.

6.4.2 Static data on $M_{2,3}$ Ni-edge

This paragraph reports the static data on the hysteresis loops acquired at the $M_{2,3}$ Ni-edge. The literature accounts for a lower signal (few percent) than the Fe one. The data have been acquired by means of a photo-diode and normalized to the photo-induced current in the ML-QWP, with the sample set at 35 degrees or 40 degrees, as reported in the two following figures. These preliminary results exhibit a contrast at the two extremities of the loops, as expected. The red dots refer to the normalized experimental data, while, as above, the blue ones to the smoothed ones. When the sample is set at 35 degrees the contrast is more evident. The MCD signal is $\approx 8.9 \times 10^{-3}$ and $\approx 6.4 \times 10^{-3}$ when the incidence angle is 35 degrees and 40 degrees, respectively.

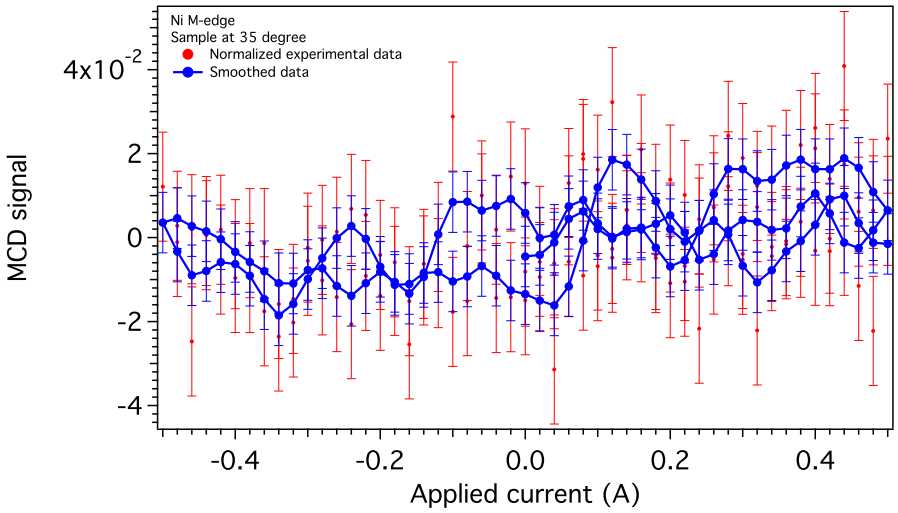

Figure 6.9: MCD hysteresis loop at the $M_{2,3}$ Ni-edge. The data have been acquired by means of a photo-diode and normalized to the photo-induced current in the ML-QWP. The sample has been set at an incidence angle of 35 degrees.

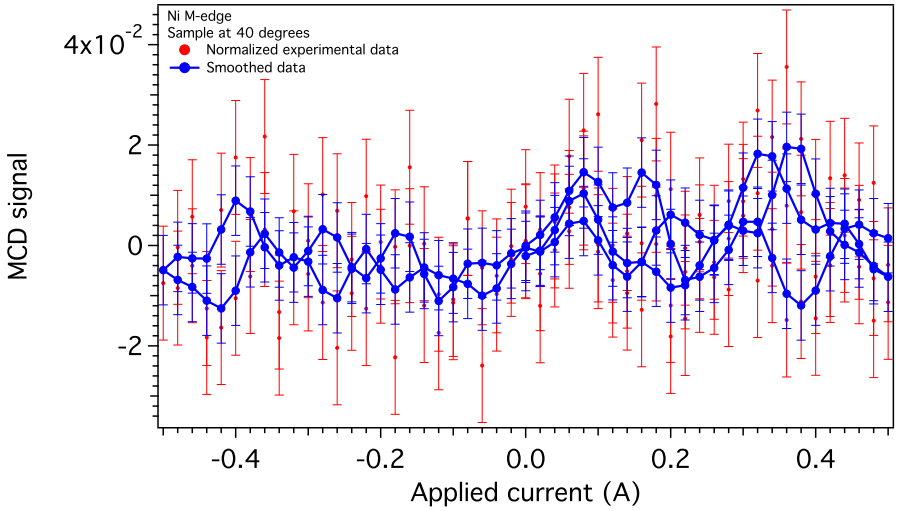

Figure 6.10: MCD hysteresis loop at the $M_{2,3}$ Ni-edge. The data have been acquired by means of a photo-diode and normalized to the photo-induced current in the ML-QWP. The sample has been set at an incidence angle of 40 degrees.

6.5 Conclusions

The experimental results reported in this chapter refer to the first applications of coherent EUV radiation, generated via HHG processes, for investigating the dynamics of ferromagnetic 3d metals at the $M_{2,3}$ Fe/Ni-edges, i.e. using HH pulses with photon energies of 54 eV and $\approx$ 66 eV, respectively. In order to overcome the intrinsic limitations for generating elliptically (or circularly) polarized HH pulses a novel multi-layer optical device has been designed in collaboration with the CXRO of the LBNL, in Berkeley (USA). The measurement performed at the ALS represent the first evidence for polarizing EUV/SXR pulses by means of such multi-layer optical devices. In addition, the unique experimental set-up developed at the T-ReX Laboratory has been used to perform preliminary measurements on the MCD behavior of a permalloy ($Fe_{20}Ni_{80}$) sample. These preliminary results report the first evidence of a MCD signal at the Fe/Ni-edges

Nonetheless, these preliminary results and the problems encountered during the acquisition have given prominence to a detailed study for im-

proving the performances of the TR-EUV/MCD set-up. This means that the number of the generated EUV photons must be increased, for example using $\approx$ 5 fs, $\approx$ 1 mJ, near-IR pulses, i.e. lowering the corresponding Keldysh's parameter from $\gamma_K \approx 0.25$ to $\gamma_K \approx 0.1$, with a consequence higher degree of the non-perturbative dynamics. On the other hand, the stability of the light source has to be improved, in order to avoid any fluctuations which can generate systematics

7

Conclusions

The scope of this Ph.D. thesis was to investigate the quantum nature of the atomic electrons involved into the generation of coherent light pulses via HHG processes. The last decade has been characterized by a large number of studies on HH by near-IR, or mid-IR, laser pulses in inert gases, molecular systems and more complex clusters. Nonetheless, the intrinsic quantum behavior of the wiggling electron in the optical field, i.e. the diffusion felt by its wavefunction, is usually overlooked into the current literature, while a detailed analysis is still lacking. This diffusion mechanism dramatically affects the efficiency of the HHG processes, i.e. the brilliance of the emitted EUV/SXR radiation, and the degree of polarization of such coherent pulses. The HHG processes represent one of the most promising optical technique for generating coherent radiation into the EUV and SXR spectral regions, with a temporal structure approaching, under certain experimental conditions, the attosecond time domain. A detailed study of the involved electron dynamics, i.e. the diffusion mechanism, can represent an innovative approach for improving the performances of the generated radiation. In addition, it represents a possible turning point for increasing the tunability (the number of the generated HH), the brilliance and the tuning of the state of polarization.

The possibility for generating HH in inert gases by means of visible optical pulses, i.e. the SH of an 1 kHz amplified laser field, has been taken into consideration and exhaustively investigated.

The interaction between the atomic electrons and the SH optical pulses

takes place in a not well defined dynamical region, which can not be formally described in the framework of the SFA, i.e. the hybrid regime. This means that the results reported in this thesis can help to improve both the tunability, of the spectral components of the generated radiation (technological improvement), and the knowledge of the physical process. The HH generated by the SH pulses exhibit an efficiency comparable, or higher, to the ones generated by the near-IR laser field. These results substantiate the conjecture that the transition amplitude of the HHG processes depends on the electron wavefunction diffusion mechanism, as predicted by M. Lewenstein and coauthors in 1994 [39]. The experimental set-up has been realized for characterizing the spectral behavior of the generated EUV photons using the near-IR or its SH optical fields.

Such results have been a starting point for investigating the spectral coherence properties of the train of the HH generated in different dynamical regimes. They represent a macroscopical signature of the different electron dynamics, corresponding to such regimes. In addition, the possibility for generating HH approaching the hybrid regime has been reported for the first time, proofing the disentanglement of the tunneling (non-perturbative) dynamical component by means of a detailed study of the damping of the number of generated photons lowering, continuously, the optical pulse energy [45]. HH have been generated using the visible pulses exhibiting a still appreciable number of photons per pulse ($\approx 10^5$) in a dynamical condition usually consider disadvantageous. In order to gain more informations concerning the hybrid regime, a novel phenomenological model has been developed.

In order to overcome the challenging generation of elliptically polarized HH for performing optical dichroic experiments such as XMCD on ferromagnetic 3d metals, a novel multi-layer optical device has been developed in collaboration with the CXRO of the LBNL, in Berkeley (USA). An *ad-hoc* experimental set-up has been developed at the T-ReX Laboratory at Elettra in Trieste (Italy) for performing TR-EUV/MCD measurements. Preliminary (static) results are reported in the last chapter of this thesis. These data prove the possibility of generating circularly polarized HH to probe the magnetic dynamics of a permalloy sample. On the other hand, a detailed

study for improving the performances of this set-up is in progress in order to perform a TR analysis of the ultra-fast de-magnetization processes.

List of Tables

3.1 Odd HH generated (photons refer to photons per pulse) in Ne by near-IR laser pulses ($\lambda_0 \approx 800$ nm) as a function of the gas pressure. 39

3.2 Odd HH (photons refer to photons per pulse) generated in Ar by near-IR laser pulses ($\lambda_0 \approx 800$ nm) as a function of the gas pressure. 41

3.3 Odd HH (photons refer to photons per pulse) generated in Xe by near-IR laser pulses ($\lambda_0 \approx 800$ nm) as a function of the gas pressure. 43

3.4 Even HH (photons refer to photons per pulse) generated by visible pulses ($\lambda_{SH} \approx 400$ nm) in Ne, Ar and Xe as a function of the gas pressure. 49

3.5 The five columns refer, respectively, to i) the inert gas, ii) the harmonic order , iii) the measured HH power, iv) the corresponding efficiency and v) the estimated Keldysh parameters. 54

3.6 The four columns refer, respectively, to i) the inert gas, ii) the harmonic order, iii) the Keldysh parameters used in the simulation (γ_K) in order to compute the theoretical efficiency (expressed in arbitrary units). 55

4.1 Spectral properties of some HH generated in Ne at a pressure of 2×10^{-3} mbar with the gas cell centered in the focus or placed at +3 mm, respectively. 63
4.2 Spectral properties of some HH generated in Ar at a pressure of 9×10^{-3} mbar with the gas cell centered in the focus or placed at ±3 mm, respectively. 64

5.1 Fit parameters of the exponential damping. 82

6.1 Main parameters of the TR-EUV/MCD experimental set-up 98

List of Figures

2.1 The temporal scale of matter. The red line focuses on the femto/attosecond timescale. Reported in [3]. 6

2.2 HHG spectrum generated in argon using ≈ 2.0 mJ, ≈ 50 fs, near-IR ($\lambda_0 \approx 800$ nm) laser pulses at a gas pressure of 5×10^{-3} mbar. The three colored boxes enclose the perturbative region (orange box), the plateau (red box) and the cut-off (violet box). 8

2.3 Ionization of an atomic electron via a) a multi-photon absorption ($\gamma_K \gg 1$) and b) a tunneling mechanism ($\gamma_K \ll 1$). Picture downloaded from [17] 12

2.4 Pictorial representation of the three steps process that lead to the emission of HH. The picture reports the processes competing with HHG (i, ii and iv). Reported in [3]. 13

2.5 Classical electronic trajectories (electron-ion distance) in atomic units (1 a.u. is ≈ 24 attoseconds), as a function of different values of θ_L. A path (violet line) leads to multiples re-collisions, others to a single one. The brown line refers to a possible classical trajectory that do not involve a re-collision process. The circles emphasize the re-collision time. An optical period for a near-IR field ($\lambda_0 \approx 800$ nm) is ≈ 111 a.u. 15

2.6 Gained kinetic energies (as a function of U_P) from the classical equation of motion. The ionized electron between 0 degree and ≈ 18 degrees will travel on a longer trajectory (long path). Otherwise, if ionized between ≈ 18 degrees and 90 degrees it will travel on the so called short path. 16

2.7 The behavior of $2|C(\tau)|$ as a function the time (fs). The values have been calculated for a near-IR optical field with wavelength $\lambda_0 \approx 800$ nm. The corresponding angular frequency is $\omega_0 \approx 0.057$ (expressed in atomic units). The optical period is ≈ 2.7 fs. 22

2.8 Coherent building-up of the generated HH fields into the non-linear medium. 23

3.1 Sketch of the laser source. It consists of two visible pump lasers (a,b), an oscillator (f), an amplifier with its stretcher (h), the amplification stage (i) and the final compressor (l). The green arrows (c,d) and the red ones (g,m) refers to the path followed by the light. 29

3.2 Optical set-up of the Mira Coherent® oscillator. 31

3.3 Layout of the optical set-up designed for generating HH pulses. The numbers refer to: 1a/b) telescope, 2a/b) CVA, 3) near-IR mirrors, 4) LBO non-linear crystal, 5) visible mirrors, 6a/b) lenses and 6c) removable mirror. The letters refer to A) cell, GC) generation chamber, MC) monochromator and CEM) detector. 34

3.4 Efficiencies of the Al-filter (red dots correspond to the transmission) and the monochromator (blue dots correspond to the reflection) as a function of the wavelength of the incoming EUV radiation. The green dots refer to the response of the CEM in terms of generated electrons per incoming photons at a fixed operating voltage (−1900 V). 36

3.5 Odd HH generated in Ne by near-IR laser pulses ($\lambda_0 \approx 800$ nm) as a function of the gas pressure. 38

3.6 Odd HH generated in Ar by near-IR laser pulses ($\lambda_0 \approx 800$ nm) as a function of the gas pressure. 40
3.7 Odd HH generated in Xe by near-IR laser pulses ($\lambda_0 \approx 800$ nm) as a function of the gas pressure. 42
3.8 Even HH generated in Ne by visible pulses ($\lambda_{SH} \approx 400$ nm) as a function of the gas pressure. 46
3.9 Even HH generated in Ar by visible pulses ($\lambda_{SH} \approx 400$ nm) as a function of the gas pressure. 47
3.10 Even HH generated in Xe by visible pulses ($\lambda_{SH} \approx 400$ nm) as a function of the gas pressure. 48
3.11 HH generated by near-IR field (red spectra) and SH (blue spectra) in Xe at pressure of 3×10^{-3} mbar. Data refer to coherent photons generated in the gas cell. 56
3.12 HH generated by near-IR field (red spectra) and SH (blue spectra) in Ar at pressure of 5×10^{-3} mbar. Data refer to coherent photons generated in the gas cell. 56
3.13 HH generated by near-IR field (red spectra) and SH (blue spectra) in Ne at an operating pressure of 1×10^{-3} mbar. Data refer to coherent photons generated in the gas cell. . . . 57

4.1 HH generated in Ne at a pressure of 2×10^{-3} mbar. The black spectrum refers to the HH generated in gas cell centered in z_0, while the blue one refers to a relative distance $\Delta z = 3$ mm. 62
4.2 HH generated in Ar at a pressure of 9×10^{-3} mbar. The black spectrum refers to the HH generated in gas cell centered in z_0, while the blue and red ones refers to $\Delta z = 3$ mm and $\Delta z = -3$ mm, respectively. 62
4.3 Spectral behavior of the 23^{rd} harmonic generated in Ne at a pressure of 1×10^{-3} mbar. The red line refer to the profile at $\Delta z = -1$ mm, while the dark blue one at $\Delta z = 3$ mm. The black profile has been acquired in the focus position. 65
4.4 Spectral behavior of the 18^{th} harmonic generated in Ne at a pressure of 1×10^{-3} mbar. 66

4.5 Spectral behavior of the 18^{th} harmonic generated in Ar at a pressure of 1×10^{-3} mbar. 66

4.6 Contribution of the geometrical dispersion from the near-IR laser field (red line) and its SH (blue line). The dark red line refers to the Gouy phase of the 23^{rd} harmonic and the violet one refers to the 18^{th} harmonic, i.e. the 9^{th} harmonic order generated by the SH field. 69

4.7 Dipole phase for HH generated by near-IR ($\lambda_0 \approx 800$ nm) laser pulses at $\gamma_K \approx 0.25$. The dark red line refers to the contribution of the long quantum path, while the red refers to the short one. 70

4.8 Dipole phase for HH generated by SH ($\lambda_{SH} \approx 400$ nm) laser pulses at $\gamma_K \approx 1$. The dark blue line refers to the contribution of the long quantum path, while the red refers to the short one. 71

4.9 Comparison between the dipole phases for odd (red line) and even (blue line) HH. Each of them have been evaluated for the long path. 71

4.10 Total axial phase (black line) for the 23^{rd} HH. The red line refers to the dipole phase, while the dark red refers to the Gouy one. 72

4.11 Total axial phase (black line) for the 18^{th} HH. The cyan line refers to the dipole phase, while the dark red refers to the Gouy one. It easy to note how the dipole phase represents only a small correction to $\Phi_{axl}(z)$. 73

4.12 Different total axial phases for the 18^{th} harmonic order evaluated for different re-coiling times, i.e. for different very long quantum paths. The thicker blue line (28 re-coilings) refers to the first non trivial dipole contribution. The red line (times 0.5) refers to the total axial phase for 23^{rd} harmonic order. . 74

5.1 Layout of the optical set-up used to study the hybrid dynamical regime. The sketch reports a (a) telescope, (b) CVA: (I) $\lambda/2$ and (II) Brewster mirrors, (d) Au mirror, (e) BBO noonlinear crystal, (f) visible mirrors, (g) generation chamber, (h) cell, (i) Al filter, (l) grating and (m) detector and (c) beam stopper used to block the s-polarized beam. 80

5.3 Calculated η_{eff} vs γ_K at $\lambda_0 = 800$ nm (blue), $\lambda_0 = 400$ nm (red) and $\lambda_0 = 266$ nm (purple). The black crosses represent the normalized experimental data. The red dashed line is a guide for the eye. Arrow 1 and 2 represent the experimental threshold for HHG processes at $\lambda_0 = 800$ nm and $\lambda_0 = 400$ nm. 86

6.1 Sketch of the experimental set-up designed for TR-EUV/MCD using circularly polarized HH at the $M_{2,3}$ Fe/Ni-edges of ferromagnetic 3d metals. The train of generated HH encounters the ML-QWP, while the residual optical field passes beyond it. The PPM mirror (2 component) is able to focus the pump and the probe pulses onto the sample. The MCD signal is extracted detecting the EUV reflected beam. Courtesy of Andy Aquila. 90

6.2 Iso-dichroic map of the MCD signal as a function of the photon energy of the incoming radiation and the angle of incidence on the sample. This test has been performed at the 6.3.2 beam-line at the ALS. 93

6.3 Hysteresis loop performed at the $M_{2,3}$ Fe-edge, zoomed onto the coercitivity value. The loop starts at 1, reach the positive and negative maxima at 2 and 3, respectively, and finally turn back to the positive maximum at 4. This test has been performed at the 6.3.2 beam-line at the ALS. 94

6.4 Hysteresis loop performed at the $M_{2,3}$ Fe-edge. This test has been performed at the 6.3.2 beam-line at the ALS. 94

6.5 The near-IR ($\lambda_0 \approx 800$ nm) beam is focused by a plane-convex lens in the vacuum generation chamber. 96

6.6 The focused near-IR beam passes through the gas cell filled with Ar generating the coherent EUV/SXR radiation. 96
6.7 angle=90 99
6.8 MCD hysteresis loop at the $M_{2,3}$ Fe-edge. The data have been acquired by means of a photo-diode and normalized to the photo-induced current in the ML-QWP. The sample has been set at an incidence angle of 40 degrees. 101
6.9 MCD hysteresis loop at the $M_{2,3}$ Ni-edge. The data have been acquired by means of a photo-diode and normalized to the photo-induced current in the ML-QWP. The sample has been set at an incidence angle of 35 degrees. 102
6.10 MCD hysteresis loop at the $M_{2,3}$ Ni-edge. The data have been acquired by means of a photo-diode and normalized to the photo-induced current in the ML-QWP. The sample has been set at an incidence angle of 40 degrees. 103

List of acronyms

ADK	Ammosov, Delone and Krainov model
as	attosecond
ATI	Above Threshold Ionization
CEM	channeltron electron multiplier
CXRO	Center for X-Rays Optics
EUV	Extreme Ultra-Violet
fs	femtosecond
GC	generation chamber
HHG	High-order Harmonic Generation
HH	High-order Harmonics
IRMA	Instrument pour la Reflectivité MAgnetique
LBNL	Lawrence Berkeley National Laboratory
MC	monochromator chamber
MPI	Multi-Photons Ionization
near-IR	near InfraRed
PM	phase-matching condition
r.r.	repetition rate
SEA	Single-Active Electron
SFA	Strong-Field Approximation
SH	Second Harmonic
SXR	Soft X-Rays

TDSE	Time-Dependent Schoedinger Equation
THG	Third Harmonic Generation process
T-ReX	Time Resolved
TR	Time-Resolved
UV	Ultra-Violet
XMCD	X Rays Magnetic Circular Dichroism
Y-I	Yudin Ivanov model

List of symbols

λ_0	wavelength of the laser field
λ_{SH}	wavelength of the SH field
ω_0	angular frequency of the laser field
T	optical period of the laser field
$\mathbf{E}_L(t)$	electric (vector) laser field
$E_L(t)$	electric (module) laser field
I_0	peak intensity of the laser field
τ_L	temporal length of the laser pulse
$S(\mathbf{p}, I_P)$	semi-classical action for a free electron set into a laser field
Γ	ionization rate
$\Gamma_{ADK}(t)$	ADK ionization rate
$N_{ADK}(t)$	ADK pre-exponential factor
I_P	first ionization potential of the inert gas
U_P	quiver (or ponderomotive) potential
n^*	effective principal quantum number
l^*	effective angular quantum number
n	principal quantum number
l	angular quantum number
$w_{ion}(t)$	ionization probability
γ_K	Keldysh parameter
τ_T	tunneling time

V_b	atomic binding potential
$\hat{H}_{kin}$	kinetic hamiltonian
$\hat{H}_{int}(t)$	interaction hamiltonian
$\hat{V}_b$	binding (or potential) hamiltonian term
$c_{bf}(\mathbf{v}, t, t_0)$	bound-free states transition amplitude
$S_{sp}(t, \tau)$	semi-classical action evaluated on the stationary points
Δk	wavevector mismatch
λ_{pump}	wavelength of the visible pump laser field
$\Phi_{Gouy}(z)$	Gouy (or geometrical) phase
$S_{st}(t, \tau)$	geometrical phase dependent on the semi-classical action
z_0	focus position
z_R	Rayleigh distance
w_{IR}	waist of the near-IR beam
w_{SH}	waist of the SH beam
Δz	relative distance between the gas cell and the focus
$\mathbf{B}_{ext}$	static magnetic field

Bibliography

[1] T. Pfeifer, C. Spielmann and G. Gerber, *Femtosecond x-ray science*, Rep. Prog. Phys. **69** 443-505 (2006)

[2] M. F. Kling and Vrakking, *Attosecond Electron Dynamics*, Annu. Rev. Phys. Chem. **59** 463-492 (2008)

[3] F. Krausz and M. Ivanov, *Attosecond physics*, Rev. Mod. Phys. **81**, 163-234 (2009)

[4] Ahmed H. Zewail, *Femtochemistry: Atomic scale dynamics of the chemical bonds using ultrafast lasers*, Nobel Lectures, December 8, 1999

[5] M. E. Fermann, A. Galvanauskas, G. Sucha, *Ultrafast lasers. Technology and Applications.*, Marcel Dekker, Inc. (2003)

[6] J-C. Diels, W. Rudolph, *Ultrashort Laser Pulse Phenomena. Fundamentals, Techniques, and Applications on a Femtosecond Time Scale*, Elsevier (2006)

[7] T. Brabec and F. Krausz, *Intense few-cycle fields: Frontiers of nonlinear optics*, Rev. Mod. Phys. **72**, 545-591 (2000)

[8] P. B. Corkum, *Plasma perspective on strong field multiphoton ionization*, Phys. Rev. Lett. **71**, 1994-1997 (1993)

[9] J. L. Krause, K. J. Schafer and K. C. Kulander, *High-order harmonic generation from atoms and ions in the high intensity regime*, Phys. Rev. Lett. **68**, 3535 (1992)

[10] R. A. Bartels, A. Paul, H. Green, H. C. Kapteyn, M. M. Murname, S. Backus, I. P. Christov, Y. Liu, D. Attwood, C. Jacobsen, *Generation of Spatially Coherent Light at Extreme Ultraviolet Wavelengths*, Science **297**, 376-378 (2002)

[11] P. Salieres, A. L'Hullier, P. Antoine, M. Lewenstein, *Study of the spatial and temporal coherence of high order harmonics*, arXiv:quant-ph/9710060v1(1997)

[12] L. V. Keldysh, Soviet Physics JETP, **47**, 1495 (1964)

[13] L. D. Landau, L. M. Lifshitz, *Quantum Mechanics Non-Relativistic Theory*, Butterworth-Heinemann; 3 edition (1981)

[14] M. Yu. Ivanov, M. Spanner, O. Smirnova, *Anatomy of strong field ionization*, Journal of Mod. Phys. **52** 165-184 (2005)

[15] M. S. Ammosov, N. B. Delone and V. P. Krainov, *Tunnel ionization of complex atoms and of atomic ions in an alternating electromagnetic eld*, Soviet Physics JETP, **64**, 1191 (1986)

[16] B. Bransden, C. Joachain, *Physics of atoms and molecules*, Benjamin-cummings Publishing Company

[17] *http://hasylab.desy.de/facilities/flash/research/multiphoton$_i$onization-/index$_e$ng.html*

[18] *http://www.mpi-hd.mpg.de/mpi/en/pfeifer/home/*

[19] M.Lewenstein, Ph. Balcou, M. Yu. Ivanov, Anne L'Huillier and P. B. Corkum, *Theory of high-harmonic generation by low-frequency fields*, Phys. Rev. A **49**, 2117-2132 (1994)

[20] M. Srednicki, *Quantum Field Theory*, Cambridge University Press (2007)

[21] D. M. Volkov, Z. Phys. **94**, 250 (1935)

[22] P. Salieres, A. L'Huillier and M. Lewenstein, *Coherence Control of High-Order Harmonic*, Phys. Rev. Lett. **74**, 3776-3779 (1995)

[23] E. Gibson, *Quasi-Phase Matching of Soft X-ray Light from High-Order Harmonic Generation using Waveguide Structures*, Ph.D. Thesis, University of Colorado (2004)

[24] D. Attwood, *Soft X-rays and extreme Ultraviolet Radiation*, Cambridge University Press (1999)

[25] M. Uiberacker, Th. Uphues, M. Schultze, A. J. Verhoef, V. Yakovlev, M. F. Kling, J. Rauschenberger, N. M. Kabachnik, H. Schroeder, M. Lezius, K. L. Kompa, H.-G. Muller, M. J. J. Vrakking, S. Hendel, U. Kleineberg, U. Heinzmann, M. Drescher, F. Krausz, *Attosecond real-time observation of electron tunnelling in atoms* , Nature **446**, 627 (2007)

[26] A. L. Cavalieri, N. Muller, Th. Uphues, V. S. Yakovlev, A. Baltuska, B. Horvath, B. Schmidt, L. Blumel, R. Holtzwarth, S. Hendel, M. Drescher, U. Kleineberg, F. Krausz and U. Heinzmann, *Attosecond spectroscopy in condensed matter*, Nature **449**, 1029 (2007)

[27] C. M. Kim, I J. Kim and C. H. Nam, *Generation of a strong attosecond pulse train with an orthogonally polarized two-color laser field*, Phys. Rev. A **72**, 033817 (2005)

[28] L. Misoguti, I. P. Christov, S. Backus, M. M. Murname and H. C. Kapteyn, *Nonlinear wave-mixing processes in the extreme ultraviolet*, Phys. Rev. A, **72**, 063803 (2005)

[29] *http://www.elettra.trieste.it/experiments/laboratories/trex*

[30] *http://www.coherent.com/Lasers/*

[31] *http://www.coherent.com/Lasers/*

[32] *http://www.padova.infm.it/luxor/*

[33] *http://www.altechna.com/*

[34] *http://www.sjuts.com/CEMModels$_S$tandard.html*

[35] *http://web.mit.edu/course/3/3.091/www3/pt/pert9.html*

[36] G. L. Yudin and M. Yu. Ivanov, *Nonadiabatic tunnel ionization: Looking inside a laser cycle*, **64**, 013409 (2001)

[37] D. Bondar, *TInstantaneous Multiphoton Ionization Rate and Initial Distribution of Electron Momenta*, **78**, 015405 (2008)

[38] A. Gordon and F. X. Kaertner, *Scaling of keV HHG photon yield with drive wavelength*, Opt. Expr. **13**, 2941-2947 (2005)

[39] A. Simoncig, B. Ressel and F. Parmigiani, *Proofing the Lewenstein's conjecture on the efficiency of the high-order harmonic generation processes*, submitted to Appl. Phys. Lett. (2009)

[40] R. P. Feynman, *Space-time approach to non-relativistic quantum mechanics*, Rev. of Mod. Phys. **20**, 367-387 (1948)

[41] P. Salieres, B. Carre', L. Le Deroff, F. Grasbon, G. G. Paulus, H. Walther, R. Kopold, W. Becker, D. B. milosevic, A. Sanpera, M. Lewenstein, *Feynman's path-Integral Approach for Intense-Laser-Atom Interaction*, Science **292**, 902-905 (2001)

[42] A. Zair, M. Holler, A. Guandalini, F. Schapper, J. Biegert, L. Gallmann and U. Keller, *Quantum Path Interferences in High-Order Harmonic Generation*, Phys. rev. Lett. **100**, 143902 (2008)

[43] M. B. Gaarde, F. Salin, E. Constant, Ph. Balcou, K. J. Schafer, K. C. Kulander and A. L'Huillier, *Spatiotemporal separation of high harmonic radiation into two quantum path components*, Phys. Rev. A **59**, 1367-1373 (1999)

[44] M. Lewenstein, P. Salieres and A. L'Hullier, *Phase of the atomic polarization in high-order harmonic generation*, Phys. Rev. A **52**, 4747-4754 (1995)

[45] A. Simoncig, A. Caretta, B. Ressel, L. Poletto and F. Parmigiani, *Damping of the tunneling mechanism in high-order harmonic generation processes induced by femtosecond visible laser pulses*, Appl. Phys. Lett. **95**, 041107 (2009)

[46] P. Carra, B. T. Thole, M. Altarelli and X. Wang, *X-Ray Circular Dichroism and Local Magnetic Fields*, Phys. Rev. Lett. **70**, 694-695 (1993)

[47] G. van der Laan, B. T. Thole, *Strong magnetic x-ray dichroism in 2p absorption spectra of 3d transition-metal ions*, Phys. Rev. B **43**, 13401-13411 (1991)

[48] D. Schulze, M. Doerr, G. Sommerer, J. Ludwig, P. V. Nickles, T. Schlegel, W. Sandner, M. Drescher, U. Kleineberg, U. Heinzmann, *Polarization of the 61st harmonic from 1053-nm laser radiation in neon*, Phys, Rev. A **57**, 3003-3007 (1998)

[49] Andrew Lee Aquila, *Development of extreme ultraviolet and soft x-ray multilayer optics for scientific studies with femtosecond/attosecond sources*, Ph.D. Thesis, UC Berkeley (2009)

[50] E. Beaurepaire, J.-C. Merie, A. Daunois and J.-Y. Bigot, *Ultrafast Spin Dynamics in Ferromagnetic Nickel*, 76, 4250 (1996)

[51] H. S. Rhie, H. A. Durr, W. Eberhardt, *Femtosecond electron and spin dynamics in Ni/W(110) films*, Phys. Rev. Lett. **90**, 247201 (2003)

[52] C. Stamm, T. Kachel, N. Pontius, R. Mitzner, T. Quast, K. Holldack, S. Khan, C. Lupulescu, E. F. Aziz, M. Wietstruk, H. A. Durr and W. Eberhardt, *Femtosecond modification of electron localization and transfer of angular momentum in nickel*, **6**, 740-743 (2007)

[53] *http://www.cxro.msd.lbl.gov/als6.3.2/*

[54] M. Sacchi, C. Spezzani, P. Torelli, A. Avila, R. Delaunay, C. F. Hague, *Ultrahigh-vacuum soft x-ray reflectometer*, Rev. Sci. Instrum. **74**, 2791 (2003)

[55] Dr. Carlo Spezzani, Ph.D. Thesis, (200)

Acknowledgment

...what we do in life, echoes in eternity.
(...ciò che facciamo in vita, riecheggia nell'eternità.)

This Ph.D. thesis is the final result of a both human and scientific experience started in February 2007. First of all I want to thank my Ph.D. supervisor Professor Fulvio Parmigiani, who offered to me at the beginning of 2007 the possibility for working in the T-ReX group, and Barbara Ressel, that helped and trained me since my first day at Elettra. She stood me and my queer ideas in order to improve the performances of the HHG source, too. I also appreciate the non conventional and exuberant personality of the technician Mr. Michele Pasqualetto. I would like to thank all the members of the T-ReX group as Cesare, Goran, Cephice, Luigi, Marco Malvestuto, Marco Zangrando, Michele Zacchigna and the Ph.D. students Jack and Federico. In addition I want to thank Carlo Spezzani, who offered to me the possibility for developing the EUV/MCD experiment using his scientific instrumentation. I would like to thank many people from Berkeley Labs as Andy Aquila, Erik Gullikson and Professor Attwood, who offered to me the unique possibility for working for almost two months in Berkeley and for visiting California wilderness.

At the end, I would like to express my full gratitude to my parents, who supported my inclination for science and helped me to study physics in Trieste.

Queste pagine stanno per diventare di pubblico dominio quindi preferisco passare all'italiano per rendere omaggio a tutti i miei amici conosciuti in questi otto anni passati a Trieste, tra i quali non posso non menzionare

quella marmaglia rappresentata dai membri dell'Ordine, al quale noi stessi abbiamo dato vita. A loro porgo il mio vigoroso saluto ed allo stesso tempo li invito (caldamente) a preservare mai domo il proprio spirito, ricordando loro che il sarà sempre e solo il loro valore a rappresentare l'unico mezzo per elevarli al di sopra delle fittizie miserie umane.

Allo stesso modo non posso scordare di menzionare i compagni di cordata e discese nella vera neve (quella non calpestata dagli esseri umani), grazie ai quali continuo a vagare per le Alpi.

Il corno ha squillato. Giunge l'ora di andare.